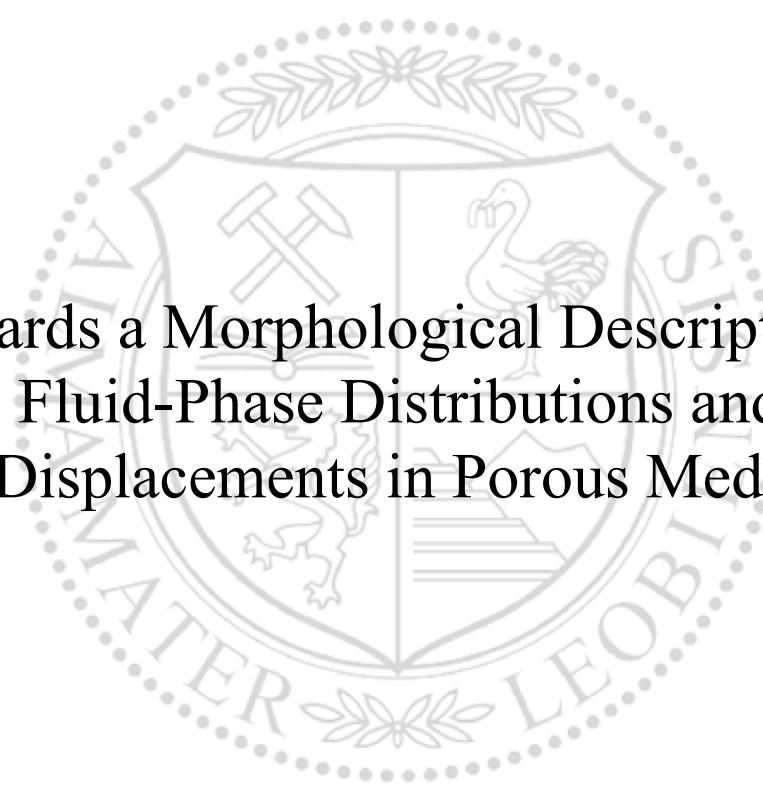Chair of Reservoir Engineering

Doctoral Thesis

Towards a Morphological Description of Fluid-Phase Distributions and Displacements in Porous Media

Dipl.-Ing. Pit Arnold, BSc

July 2023

MONTANUNIVERSITÄT LEOBEN

www.unileoben.ac.at

EIDESSTATTLICHE ERKLÄRUNG

Ich erkläre an Eides statt, dass ich diese Arbeit selbständig verfasst, andere als die angegebenen Quellen und Hilfsmittel nicht benutzt, und mich auch sonst keiner unerlaubten Hilfsmittel bedient habe.

Ich erkläre, dass ich die Richtlinien des Senats der Montanuniversität Leoben zu "Gute wissenschaftliche Praxis" gelesen, verstanden und befolgt habe.

Weiters erkläre ich, dass die elektronische und gedruckte Version der eingereichten wissenschaftlichen Abschlussarbeit formal und inhaltlich identisch sind.

Datum 13.07.2023

_____

Unterschrift Verfasser/in
Pit Arnold

To my beloved wife and daughter,

your unconditional support made this possible.

Acknowledgments

The past few years have been quite a journey culminating in this thesis. First and foremost, I want to thank my supervisor, Holger Ott, for mentoring and pushing me since the end of my Bachelor's degree. You were the reason I decided to embark on this PhD journey by awakening my excitement for science. One of the things I cherished most were our lengthy after-work discussions in your office, which often began with topics at subatomic levels and expanded into questions about the universe. Your continuous support has transformed me and helped me transition into a scientist.

I would also like to extend special thanks to my mentor, Steffen Berg, who, in addition to his rapid response times, consistently provided valuable input to my research. After each meeting, my head was buzzing, and my "to-read" paper list seemed to grow exponentially. Your profound knowledge always guided me back to the right path whenever I felt lost in the labyrinth of research. I especially admire your ability to accurately summarize papers and others' research within a few sentences. Our discussions helped me to gain a clearer picture.

Additionally, I am grateful to my former team at the Chair of Reservoir Engineering, where ideas were conceived and discussed, and where laughter and frustrations were shared, and friendships blossomed. Special thanks to Ahmad Kharrat, Patrick Jasek, and Gerald Stiedl, who always lent an open ear to my problems. I want to specifically thank Boris Jammernegg, who assisted me in developing the scripts I used for this thesis and who was always open to discussions despite having a busy schedule himself. I am thrilled to call all of you my friends!

I must also express my gratitude to many people outside my team who have been instrumental in my journey. I want to thank Mario Dragovits for being there at all times, boosting my confidence when I was struggling. His work during his Master's thesis paved the way for important parts within this thesis.

I would also like to thank the team at Math2Market, namely Arne Jacob, Christian Hinz, and Sven Linden, who developed the method used for the simulations and were always open to discussions and receptive to changes that needed to be applied. Working with such a fantastic team has been a pleasure.

Last but certainly not least, I want to extend my heartfelt thanks to all my family, friends, and acquaintances I met along this journey for their unwavering support and encouragement.

Thank you all for being part of this incredible adventure.

Abstract

Access to energy resources is indispensable for the growth and development of modern society. As the majority of these resources are obtained through the extraction of fossil fuels, there is a consequential increase in CO_2 emissions which contribute to the greenhouse effect. This necessitates the urgent implementation of efficient fossil fuel production methods during the transition to cleaner energy sources, and the development of strategies for capturing and sequestering CO2 in geological formations. Understanding flow and displacement phenomena in porous media is central to these endeavors. However, given the scarcity and often incompleteness of reservoir data, there is a need for reliable simulation methods.

This research aims to model and analyze multiphase displacement processes in porous media to deepen the understanding of these phenomena and develop methods that will ultimately bridge the gap between microscopic and macroscopic scales. The primary objective is to compute capillary pressure and relative permeabilities and conduct an in-depth analysis of imbibition displacement modeling under different wettability conditions. The Morphological Method (MM) is particularly appropriate for this research due to its computational efficiency, allowing for simulations on large domains while accommodating uncertainty analysis. This method, which uses mathematical morphology to populate a porous medium with different phases, will be not only utilized but also further refined within this study.

Traditionally, MM models quasi-static, capillary-driven processes and does not incorporate a time scale, rendering it less effective for imbibition modeling. This study introduces an enhanced version of MM by integrating forced imbibition, effectively adding a quasi-time scale to the displacement process, which improves the alignment between model predictions and experimental data. Additionally, the extended MM includes structural constraints and introduces two strategies for distributing the non-wetting material within porous structures: a stochastic approach, which involves random distribution, and a deterministic approach that orientates the distribution on the pore size distribution.

Using the extended MM, capillary pressure and relative permeability saturation functions for various rock structures are modeled, and the sensitivities of these functions to different wetting states and contact angles are investigated. Minkowski functionals are employed to provide a comprehensive description and evaluation of the results, highlighting distinct topologies for

wetting and non-wetting phases and illustrating the significant influence of spontaneous imbibition on topology.

This research represents a major step forward in the understanding of pore-scale physics in porous media and the enhancement of multiphase flow modeling techniques. It underscores the importance of taking into account the pore structure and wettability distribution in simulations. The extended MM emerges as a robust and efficient pore-scale simulation tool with significant potential for practical applications in accurately modeling fluid displacements in porous media. This is crucial for uncertainty analysis, the proficient extraction and storage of resources, and the underground storage of CO2.

Zusammenfassung

Der Zugang zu Energiequellen ist für das Wachstum und die Entwicklung der modernen Gesellschaft unerlässlich. Da der Großteil dieser Ressourcen durch die Förderung von fossilen Brennstoffen gewonnen wird, kommt es zu einem Anstieg der CO_2-Emissionen, die wesentlich zum Treibhauseffekt beitragen. Dies erfordert die dringende Einführung effizienter Methoden zur Produktion von fossilen Brennstoffen während des Übergangs zu saubereren Energiequellen sowie die Entwicklung von Strategien zur Abscheidung und Speicherung von CO2 in geologischen Formationen. Das Verständnis von Strömungs- und Verdrängungsphänomenen in porösen Medien sind für diese Ziele von zentraler Bedeutung. Aufgrund der Knappheit und oft unvollständigen Natur von Lagerstättendaten besteht jedoch Bedarf an zuverlässigen Simulationsmethoden.

Diese Forschung zielt darauf ab, Mehrphasenverdrängungsprozesse in porösen Medien zu modellieren und zu analysieren, um das Verständnis dieser Phänomene zu vertiefen und Methoden zu entwickeln, die letztendlich die Lücke zwischen mikroskopischen und makroskopischen Skalen überbrücken. Eines der Hauptanliegen ist es, den Kapillardruck und die relativen Permeabilitäten zu berechnen und eine eingehende numerische Analyse von Verdrängungsprozessen bei verschiedenen Benetzungseigenschaften durchzuführen. Die Morphologische Methode (MM) ist besonders geeignet für diese Forschung aufgrund ihrer rechnerischen Effizienz, die Simulationen auf großen Domänen ermöglicht und gleichzeitig Unsicherheitsanalysen berücksichtigt. Diese Methode, welche die mathematische Morphologie verwendet, um ein poröses Medium mit verschiedenen Phasen zu bevölkern, wird in dieser Studie nicht nur genutzt, sondern auch weiter verfeinert.

Traditionell modelliert die MM quasi-statische, kapillargetriebene Prozesse und berücksichtigt keine Zeitskala, was sie für die Modellierung von Imbibitionsprozessen weniger effektiv macht. Diese Studie führt eine erweiterte Version der MM ein, indem sie die forcierte Imbibition integriert, wodurch effektiv eine quasi-Zeitskala in den Verdrängungsprozess eingeführt wird, was die Übereinstimmung zwischen Modellvorhersagen und experimentellen Daten verbessert. Darüber hinaus enthält die erweiterte MM strukturelle Einschränkungen und führt zwei Strategien zur Verteilung der nicht benetzenden Oberflächen innerhalb poröser Strukturen ein: einen stochastischen Ansatz, der eine zufällige Verteilung beinhaltet, und einen deterministischen Ansatz, der die Verteilung an der Porengrößenverteilung orientiert.

Unter Verwendung der erweiterten MM werden Kapillardruck und relative Permeabilitätssättigungsfunktionen für verschiedene Gesteinsstrukturen modelliert und die Sensitivitäten dieser Funktionen gegenüber verschiedenen Benetzungszuständen und Kontaktwinkeln untersucht. Minkowski-Funktionale werden eingesetzt, um eine umfassende Beschreibung und Bewertung der Ergebnisse zu liefern, dabei werden die Topologien für benetzende und nicht benetzende Phasen untersucht und der Einfluss der spontanen Imbibition auf die Topologie veranschaulicht.

Diese Forschung stellt einen großen Fortschritt im Verständnis der Fluidphysik in porösen Medien und der Verbesserung von Mehrphasenfluss-Modellierungstechniken dar. Sie unterstreicht die Bedeutung der Berücksichtigung der Porenstruktur und der Benetzungsverteilung in Simulationen. Die erweiterte MM erweist sich als robustes und effizientes Werkzeug für Simulationen auf dem Porenmaßstab mit erheblichem Potenzial für praktische Anwendungen bei der präzisen Modellierung von Fluidverdrängungen in porösen Medien. Dies ist entscheidend für die Analyse der Unsicherheiten, die effiziente Gewinnung und Speicherung von Ressourcen sowie die Untertagespeicherung von CO_2.

Table of Contents

Chapter 1

Introduction

The growth and development of our modern society are strongly connected to the access and availability of energy. Vast amounts of our energy consumption are stilled by the production of fossil resources from the subsurface, consequently causing massive emissions of CO_2 into the atmosphere. While further production from the underground is necessary to maintain our current status, capturing and sequestration of CO2 underground is substantial for limiting global warming. The production and storage of liquids or gases from geological reservoirs are linked to flow and fluid displacement events in porous media. Even though subsurface production has been ongoing for decades, there is often limited information available from the reservoirs. Direct information obtained from well logging reflects only a portion of the actual reservoir; therefore, additional measurements and interpretations are necessary.
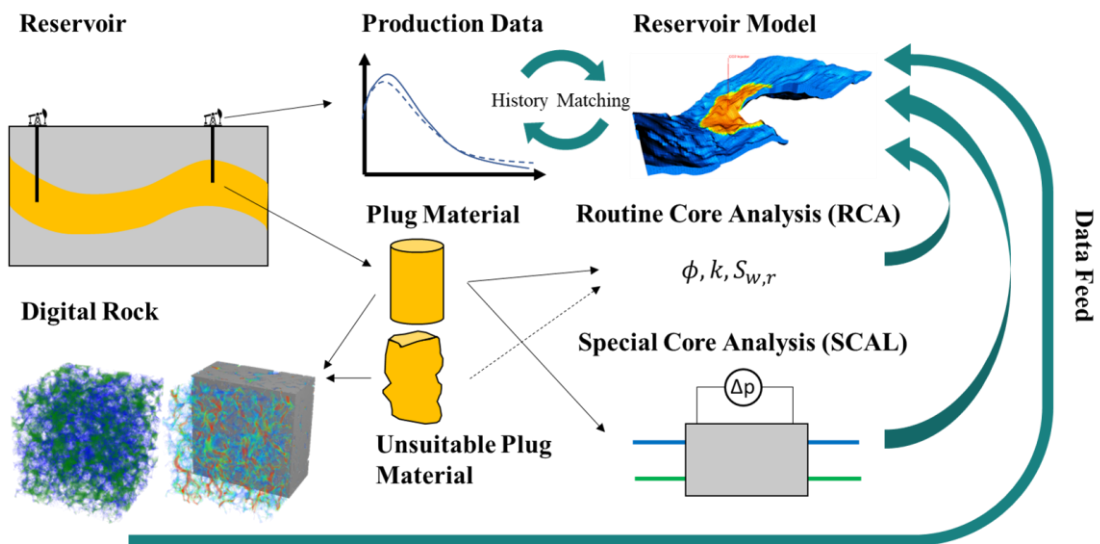

Figure 1 Illustration of how data required for reservoir modeling can be obtained from field production data and laboratory experiments, i.e., core analysis and digital rock analysis. Core analysis can be limited if the samples are not intact or too small in size. The illustration shows how digital rock can add information to existing workflows, especially if special core analysis is not feasible.

Most of the data is derived from pressure responses (from multiple wells) or is measured in a laboratory, as sketched in Figure 1. When (intact) core plugs are available routine and special

core analysis experiments can be performed, giving out a range of information about the porous media system and fluid displacement properties. Combined with production data from the field reservoir models can be updated to predict the flow behavior within a reservoir. However, they are time-consuming, limiting the variability of experiments that can be performed. Furthermore, the production data available might be limited as it is the beginning of a field life or not available at all, e.g., as it can be for potential CO_2 storage projects.

Advances in imaging technologies and computational power allow for solving fluid transport and displacement problems on multiple scales. While the bridging between those scales is extremely complex and not yet solved, significant advances have been made in modeling fluid flow on the pore scale. Micro computed tomography (mCT) allows the non-destructive imaging of the rock, pore space, and fluids. In combination with state-of-the-art modeling approaches workflows have been established for solving flow and transport properties of different systems, which are all included in digital rocks. This does not only reduce uncertainties for existing reservoirs but also allows first estimations of reservoir properties and flow behavior for newly explored fields.

1.1   Scope and Objectives

Multiphase flow modeling in porous media is of key interest for predicting flow, displacement and trapping potentials in various subsurface applications, such as fluid and gas storage and production. One of the most active areas of research is attempting to bridge the gap between the pore scale and the Darcy scale. While the Darcy scale provides and effective description applicable to the reservoir scale, pore-scale fluid dynamics provides physical explanations. Effects, such as capillary effects, are strongly related to the microscopic pore structure as well as the wettability of the system, whereas the later extends over several scales. The capillary pressure and relative permeability saturation functions, which are coupled, are used to characterize the flow behavior in a porous media. The understanding of pore scale physics plays a key role in further developing multiphase flow modeling. In the past, fundamental mechanisms were both incorporated into various modeling methods and derived from them through learning. It is also noteworthy that results are strongly influenced by the segmentation of the tomographic images and can vary between individual users (Andrä et al. 2013a, 2013b). Therefore, if possible, the segmentations are calibrated using experimental data to minimize user bias.
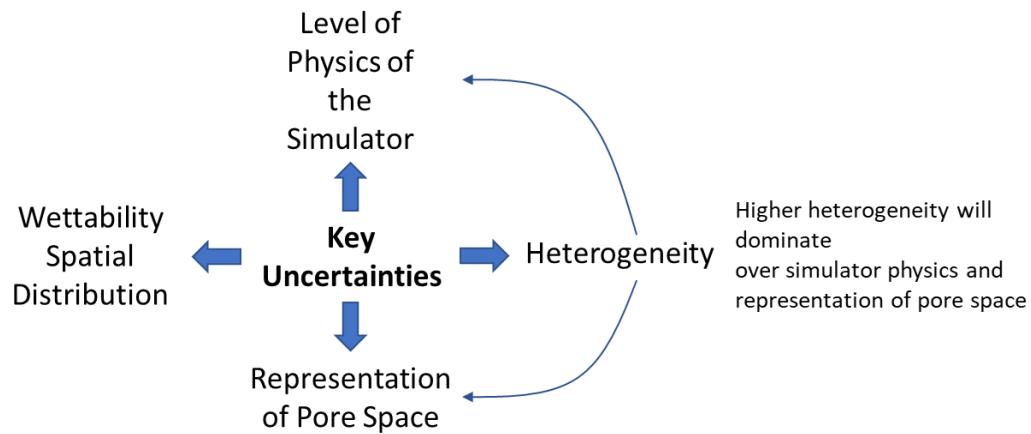
Higher heterogeneity will dominate over simulator physics and representation of pore space

Figure 2 Key inherent uncertainties of pore scale modeling.

The three most commonly employed methods for solving porous media flow are the Lattice Boltzmann Method (LBM), Pore Network Modeling (PNM), and the Morphological Method (MM). However, while basic morphological operations are frequently integrated with other numerical simulations, they are seldom utilized to model entire displacement processes. Other methods, such as volume of field (VoF) or smooth particle hydrodynamics (SPH) are available, however have not reached the popularity of LBM, MM, and PNM within the last decade (Liu et al. 2007). Each of these methods has its own distinct advantages and disadvantages, but they all commonly exhibit the same key uncertainties, as illustrated in Figure 2. These uncertainties arise from insufficient information and technical limitations, such as image resolution and computational capabilities. All of these uncertainties are interconnected, although some may have a greater influence than others. A high level of heterogeneity within our sample, e.g., as in carbonates, will dominate over the effects caused by the level of physics or the representation of the pore space. The wettability and the spatial distribution on the other hand might be connected to the level of heterogeneity and adds to complexity. Each of the beforenamed methods has therefore different approaches to tackle these key risks, which will be more thoroughly discussed in Chapter 2.
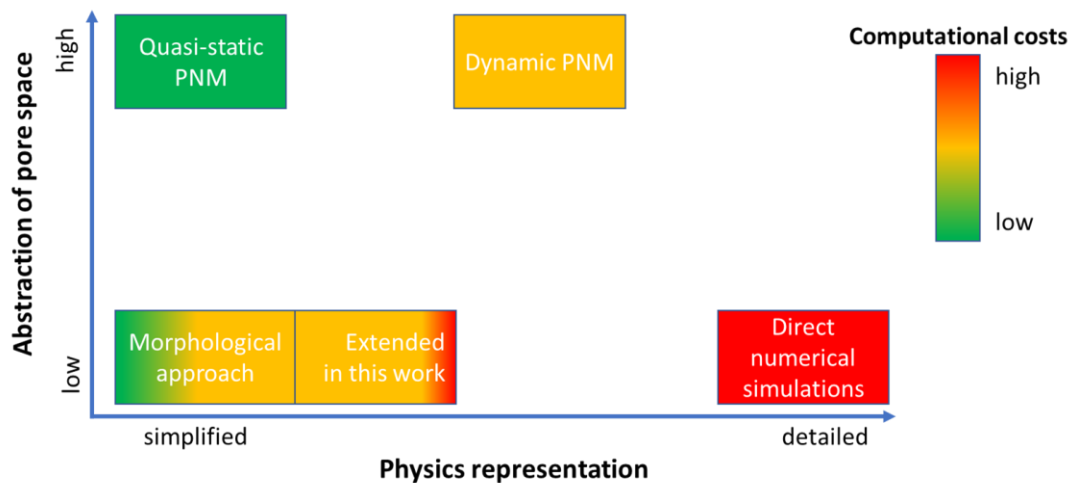
Figure 3 Categorization of the main multiphase modeling approaches by the level of implemented physics versus the abstraction of the pore space. The color code indicates the computational costs needed to simulate comparable systems.

Figure 3 displays a categorization of the different modeling approaches on the basis of the physics used and the abstraction of the pore space. The color code indicates a rough distinction with regard to the computational costs on the basis of the experiences made within this work and a comparative study about the CPU usage of the methods by Vogel et al. from 2005 (Vogel et al. 2005). Note that the computational costs increase exponentially increasing structure sizes and that with the usage of GPU clusters the efficiency of e.g., LBM simulations has greatly increased, which makes a direct comparison difficult. A low abstraction of the pore space means that the simulation method works on the actual measured rock structure derived from e.g., micro computed tomographic images. The MM and LBM, both work directly on the segmented images, resulting in a detailed representation of the pore space, but increased computational costs, as indicated by the color code. For the PNM different extraction algorithms are used, resulting in a simplified representation of the pore space (Al-Kharusi und Blunt 2007; Lindquist et al. 1996; Dong und Blunt 2009). The most simplified representation of a pore network is using spheres for the pores bodies and sticks for the pore throats connecting them. It is worth mentioning that with the implementation of different geometries complexity has been added to the abstracted pore models. As one of the major goals is the proper prediction of the flow behavior, the level of physics implemented in each method is a key attribute. Here a first distinction between quasi-static and dynamic models needs to be made. The quasi-static PNM and MM both have no time scale associated to the displacement process, which reduces the computational costs, but results in limited prediction capabilities. Both models rely on the direct or indirect implementation of rules to model displacement events. The main difference is that in the MM the implemented algorithm ultimately follows the structural properties, therefore

following the rules imposed by the structure, e.g., pore throat size distribution. This approach proves effective for processes dominated by forced capillary action, like primary drainage displacement, where the morphological operations successfully identify and characterize the pore throats accurately. An imbibition on the other hand consists of a spontaneous and forced process, which is rather driven by interfacial properties like the contact angle distribution and wetting state. To properly model more complex displacement events an increased level of implemented physics and a time scale, such as in dynamic PNM and LBM, is necessary (Lenormand et al. 1988). Both models are much closer to modeling actual multiphase flow while demanding more computational power. One could argue that with excessive computational power direct numerical simulations (DNS) should be carried out. However, also here limitations apply as the outcome is fixed to the input and boundary conditions, therefore DNS can be considered as "computer experiments". That means if not every detail is resolved during imaging the resulting gaps need to be bridged. As example, recent work has shown that the influence of the wettability distribution and multiscale properties cannot be neglected (Ruspini et al. 2021; Garfi et al. 2022). Meaning that workflows need to be adjusted, combined, and/or calibrated against experimental data. Therefore, it is beneficial to investigate whether PNM and morphological approaches can be further improved to a level where the results are acceptable. This work extends the MM by introducing a quasi-time scale through the incorporation of structural constraints. These constraints serve as a stopping criterion for the displacement process, ensuring that the sequence of contact line propagation is honored. By doing so, the method introduces a sense of temporal progression in the simulation without explicitly solving the underlying time-dependent equations. By adding these structural constraints, the extended MM can avoid far-reaching domain-filling events that may result in premature disconnections of a phase. This is beneficial because such events can lead to unrealistic representations of the displacement process. Instead, it allows for intermediary fluid distributions, enabling further analysis of fluid phase changes during the displacement process. Overall, the extension of the MM with structural constraints not only introduces a quasi-time scale, capturing the temporal aspects of the displacement process but also prevents unrealistic domain-filling events. This enhances the accuracy and reliability of the simulation, facilitating the analysis of fluid phase changes throughout the process.

The focus of this work lies in the computation of capillary pressure and relative permeabilities with detailed investigations of the imbibition displacement modeling. Different wetting states and systems are investigated, to gain further insight on the morphological description of fluid phases and displacement events in porous media.

1.2   Overview of Dissertation

In Chapter 2 the different modeling approaches for displacement processes in porous media are introduced and compared. A focus is put on the modeling of different wetting states, as they majorly influence multiphase flow simulations. Topological analysis of fluid phases and pore structures is introduced, which will later be used to uniquely identify and compare the modeling results.

The morphological method (MM) and its developments, as used throughout this thesis, are thoroughly described in Chapter 3. Furthermore, all additional computational methods used in the frame of this thesis are introduced.

Chapter 4 encompasses the introduction, along with a comparison of the structural and computed petrophysical properties of various porous media structures. These structures serve as a basis for evaluating and contrasting the trends observed in the computations and developments of the MM.

In Chapter 5 the MM is applied to model capillary pressure and relative permeability saturation functions from the rock structures introduced in Chapter 4. The functions are investigated with their sensitivities to the different modeling approaches of wetting states (deterministic and stochastic) and the assigned contact angles within the domain. The implementations are validated against an experimental dataset.

In Chapter 6 the former sensitivities are further analyzed and compared by computing the Minkowski functionals, giving a more comprehensive description of the results allowing for better comparability and evaluation of the data.

Chapter 7 concludes the thesis by presenting the key findings of the study. The results indicate that the wettability distribution within a system plays a crucial role in influencing the modeling of an imbibition process, even for different types of rocks. Additionally, the study revealed that the MM can be extended beyond modeling capillary-dominated displacements.

Chapter 2

Theoretical Background

2.1 Displacement Processes and Saturation Functions in Porous Media Flow

Displacement events in porous media are characterized on multiple scales, (a) due to the underlying physical description and (b) due to the porous media domain sizes. While single displacement events occur on the pore scale, continuum-scale displacements average over a series of pore-scale events. In porous media flow, a distinction is therefore made between the pore scale and Darcy scale. Displacement processes in the former are typically driven by the two main mechanisms of piston-like and snap-off events. The competition of capillary and viscous forces results in different invasion patterns for drainage and imbibition processes, i.e., wetting and non-wetting phase displacements. Consequently, dominant processes such as Haines Jumps and snap-off events need to be properly modeled to accurately predict and ultimately upscale two-phase flow properties (Berg et al. 2013; Singh et al. 2017a; Zacharoudiou et al. 2018). On the Darcy scale, gravitational forces need to be included as well, especially for high-density ratios, e.g., between gaseous and liquid phases.

2.1.1 Wettability and Wettability Modeling

In general, the wettability is defined as the preference of a phase to adhere to a surface in presence of another phase. The contact angle θ at the three-phase contact line is taken as a measure for the wetting state to decide whether a fluid is wetting, non-wetting, or whether there is no wetting preference of a fluid to the mineral phase. It significantly affects fluid displacement and trapping events in porous media, which is reflected in the resulting capillary pressure and relative permeability curves (Anderson 1986; Donaldson und Alam 2008a, 2008b). The complexity of wettability comes from the many different factors it depends on

such as mineral and fluid-phase compositions, thermodynamic conditions, surface chemistry and the exact pore geometry. The wettability can be defined on multiple scales, as shown by Armstrong et. al resulting in an increased degree of freedom for the implementation (Armstrong et al. 2021).

In macroscopic experiments, the wettability of a system is typically defined by different indices, with the Amott wettability index and the USBM method index being the most well-known ones (Amott 1959; Donaldson et al. 1969). Both methods give an indication of the wetting state of a system, whereas the USBM method compares the ratio of mechanical work by the spontaneous and forced process, while the Amott method compares the saturation ranges for each process. While they might fail for a qualitative distinction, especially towards neutral wetting systems, they are useful for a quantitative description of a wettability change.

On a microscopic scale, the spatial wettability distribution has a profound influence on the displacement process as it dictates the propagation of an invading and displaced fluid(AlRatrout et al. 2018; Valvatne und Blunt 2004; Murison et al. 2014; Foroughi et al. 2020). Therefore, the wettability distribution is a part of the overall system heterogeneity (Garfi et al. 2022). However, the overall influence might mitigate on larger scales. Advances in imaging techniques and computational power enabled further insights by in-situ measurements of contact angles and interface curvatures for wettability characterizations (Alhammadi et al. 2017; AlRatrout et al. 2017; Andrew et al. 2014; Higgs et al. 2022; Scanziani et al. 2017; Blunt et al. 2019). However, the in-situ measurement of the contact angle at the three-phase contact line poses rather challenging, as uncertainties in image quality and segmentation are amplified. An alternative approach is given by using a thermodynamic method. Locally the wettability is controlled by the energy balance of the fluid phases in contact with the solid and by fluid-fluid contacts, by which at local capillary equilibrium a thermodynamically-consistent contact angle can be defined (Blunt et al. 2019). By this, the average contact angle of a displacement event can be correctly defined, whereas a geometrically measured contact angle only delivers a local property. The fluid geometry plays a major role for the transport properties, which ultimately is a consequence of the geometry of the pore structure in combination with the local wetting properties (Singh et al. 2017b; Singh et al. 2019). Therefore, the thermodynamically-consistent contact angle as suggested by Blunt et al. could lead to major improvements with regard to the prediction of displacement events (Blunt et al. 2019).

Depending on the modeling approach chosen the wettability is implemented differently. A possible implementation is the discrete assignment of contact angles to voxels or entire regions in a model (Armstrong et al. 2016; Arnold et al. 2023). When working with the actual pore structure different wettability regions might be defined based on the initial grey scale image

where individual minerals can be identified. Other approaches distribute CAs on the basis of experimental data or statistically by general distribution functions. A change in the contact angle during displacement processes can be incorporated by the hysteresis of the advancing and receding contact angle (Joekar-Niasar et al. 2013; Valvatne und Blunt 2004).

A common approach in PNM is the distribution of contact angles within a defined range on the basis of a distribution function or random assignment (Bultreys et al. 2018; Gharbi und Blunt 2012; Høiland et al. 2007; Raeesi und Piri 2009). Depending on the model the contact angles are assigned to the pores and throats. The relative frequency of all contact angles defines the wettability of the system.

In morphological modeling, a contact angle is directly assigned to each solid voxel. The number of contact angles is then limited by the number of solid materials. Resulting typically in only a limited number of implemented contact angles. However, the discrete assignment allows for a simple implementation of different wetting conditions even within a single bore body.

Lattice-Boltzmann models have the highest degree of freedom and complexity, when implementing wettability since all kinds of physical mechanisms over several scales can be accounted for. Therefore, effective modeling approaches, such as assigning a wetting map are often chosen (Ramstad et al. 2020; McClure et al. 2021; Boek und Venturoli 2010). Similar to the assignment of a contact angle for a voxel, a scalar affinity value can be assigned, reflecting the wetting condition. This enables effective modeling of moving and equilibria contact lines. Note, this is just an exemplary implementation, based on the software package of James McClure et al., and that there are many other possible implementations (McClure et al. 2021).

2.1.2 Capillarity in Two-phase Flow

The capillary pressure for an interface at rest is defined by the Young-Laplace equation,

$$p_c = \frac{2\sigma \cos\theta}{r} \qquad [\,1\,]$$

with σ being the interfacial tension, θ the contact angle at the three-phase contact line and r the local radius of curvature of the interface. It is defined by microscopic structural properties, interfacial and surface forces, which in case of a rock depend on the mineral and fluid phases present. In two-phase systems the macroscopic capillary pressure of a saturation state ($P_c(S_\alpha)$) is defined by the difference between the pressures of the fluids (P_α and P_β).

$$P_c(S_\alpha) = P_\beta - P_\alpha \qquad [\,2\,]$$

Equation [1] is limited to quasi-static situations when dynamic effects are neglected. It is therefore often used to describe the capillary pressure at the pore scale. The capillarity of a

porous medium determines both displacement processes and trapping alike, as it acts as an opposing force to viscous displacements. In porous media research, capillary pressure-related processes are defined as drainage and imbibition, relating the process to the displacement of a wetting phase and vice versa. Both are essential for history matching and predictive purposes. Experimentally, drainage and imbibition capillary pressure curves can be measured by mercury injection, porous plate and centrifuge methods. Being time-consuming the modeling of both processes is a key interest in pore-scale modeling.

2.2   Multiphase Flow Simulation Techniques

On a continuum scale, multiphase flow in porous media is described on a phenomenological basis by the two-phase extension of Darcy's law. Two-phase Darcy requires capillary pressure and relative permeability saturation functions as input parameters. The phase-specific flow, v_α, is then described by

$$v_\alpha = -\frac{k_{r\alpha}(S_\alpha)k}{\mu_\alpha}\nabla p_\alpha \ , \qquad\qquad [\,3\,]$$

where $k_{r\alpha}$, S_α, μ_α and ∇p_α are the relative permeability, saturation, viscosity and pressure gradient of fluid α. However, the equation is physically incomplete as it does not incorporate hysteresis during displacements (Hilfer 1998; Niessner et al. 2011). A more complete description is given, when derived from a thermodynamic consistent approach, as suggested by Hassanizadeh and Gray (Hassanizadeh und Gray 1990). Niessner et al. showed in their work that the classical extended two-phase Darcy's law can be combined with the thermodynamic approach (Niessner et al. 2011). However, it requires that a more microscopically detailed description of the system is known. While a conceptual problem is being posed for the scaling from the pore to Darcy scale, the missing information could be given by the topology of the system (Khanamiri et al. 2018). Furthermore, computing the integral geometry of the system during displacement processes allows to give an estimation of the hysteresis of the system by quantifying the dissipated energy (Khanamiri et al. 2018; McClure et al. 2018; McClure et al. 2020; Schlüter et al. 2016). Further information on the topological description of a system will be given in chapter 2.3 of this thesis.

While these thermodynamic-geometrical descriptions can reduce the uncertainties in displacement modeling, a major challenge is still posed by the upscaling. Presently, the application of these complex flow equations to reservoir simulations may not be feasible.

Experimental multiphase flow parameters are typically derived from continuum-scale special core analysis experiments, which are costly and time-consuming. Therefore, a possibility could be deriving saturation dependent parametrization from simulation results in combination with

uncertainty analysis. Actual multiphase flow modeling has proven to be challenging as viscous and capillary effects need to be considered, extensively increasing the computational demand and complexity. In the past fundamentals have been learned from pore-scale modeling, where simplifications and assumptions are applied to effectively model displacement processes. A common approach is quasi-static modeling where only capillary forces are accounted for. In those models, multiphase flow is only indirectly solved by computing single-phase flow on the connected phases while considering the rest as rigid. This works quite well for capillary-dominated processes such as a primary drainage but lacks for more complex processes such as imbibition. Alternatively, in dynamic pore network modeling and in direct numerical simulations a time scale is introduced to consider the evolution of the flow field enabling the modeling of actual multiphase flow.

2.2.1 Quasi-static Pore-scale Modeling

Under dynamic flow conditions, viscous and capillary forces compete with each other, which is quantified by the capillary number, Ca. A commonly used approximation to define the ratio between the viscous and capillary forces has the following dimensionless form:

$$Ca = \frac{\mu_w u_w}{\sigma_{nwp}},$$ [4]

with, μ_w, being the viscosity and u_w, being the velocity of the wetting phase and σ_{nwp} defining the interfacial tension between the wetting and non-wetting phase. However, this approximation assumes that both forces act on the same length scale (Armstrong et al. 2014). Quasi-static modeling approaches, such as the MM and quasi-static PNM, rely on the rule-based population of digital models, assuming that the capillary number is very low, i.e., capillary forces are dominating. However, this assumption does not hold for dynamic processes where viscous forces cannot be neglected. Furthermore, this choice of the capillary number is limited to the microscale and needs to be adjusted when used for the macro scale (Armstrong et al. 2014).

In PNM the invasion is controlled by the capillary entry pressure of the individual pore, obtained by calculating the force balance on the duct interface. This leads to a sequence of calculated equilibrium states that mimic a displacement process. Whereas for drainage modeling only piston-like displacements and optionally snap-off events are considered, an imbibition process is rather characterized by the dimensions of the pore body than the pore throats. At each equilibrium state, the effective permeability of a phase can be determined by calculating the total flow rate of the phase through the occupied portion of the network and dividing it by the total single-phase flow rate of the network. The phase flowrate is found by solving the pressure between all pores, with regard to the fluid conductance and distance

between the pore centers. In the most basic case the conductance is given by Poiseuille's law which can be adapted for different geometries representing the pore throats (Valvatne und Blunt 2004).

The MM delivers similarly to the quasi-static PNM different equilibrium states. However, those are directly obtained from the geometrical structure of the measured pore space by applying morphological operations (Hilpert und Miller 2001). By applying different algorithms, including connectivity checks, displacement events are mimicked. The effective permeability is then found by solving the (Navier-)Stokes equation directly on the connected fluid phase. In contrast to PNM, no geometry factors are necessary as the flow is directly calculated on the pore structure, however resulting in an increased computational effort. Figure 4 shows the workflow of calculating multiphase flow properties when using the MM for populating a simplified 2D model. The blue phase represents a WP which is replaced by a NWP in a drainage process. The upper part of the figure depicts a single displacement event for a specific capillary pressure, p_c, resulting in two connected phases where an effective flow can be calculated. The MM will be introduced in more detail in Chapter 3 as it is the main modeling approach applied in this thesis.
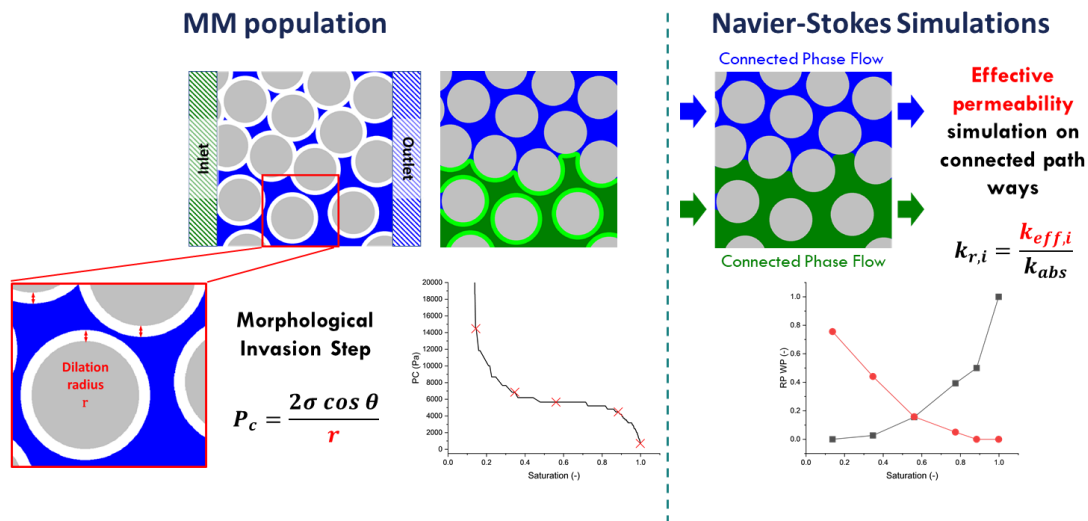
Figure 4 Workflow for calculating multiphase flow parameters for the morphological method. Quasi-static equilibrium states are obtained from morphological operations (left). The effective permeability is then calculated on the connected phases by solving the (Navier-)Stokes equation (right). In that way, the interplay of capillary-viscous flow in which both forces act simultaneously is decomposed into a sequence of steps, i.e., a capillary step (left) and a viscous step (right).

Quasi-static modeling is computationally cheap allowing the simulation of large domains and uncertainty modeling. They work quite well for strongly wetting conditions and capillary-dominated processes, however, are limited as visco-capillary effects are not accounted for (Berg

et al. 2016b; Bultreys et al. 2020; Joekar Niasar et al. 2009; Valvatne und Blunt 2004). Therefore, the modeling of an imbibition process is mainly restricted to the spontaneous part. In PNM this problem is tackled by a dynamic modeling approach, which includes interface movement, filling events and a time scale (Regaieg und Moncorgé 2017; Joekar-Niasar et al. 2010; Joekar-Niasar und Hassanizadeh 2012). The MM faces similar challenges, which due to the purely geometry-based nature has no time scale included and therefore does not account a proper contact line propagation. This deficiency can cause intermediary states to be overlooked during extensive pore-filling events, which are solely determined by structural constraints. Direct comparisons between experimental and simulated data have shown that the initial approach for imbibition modeling is leading to strong discrepancies (Berg et al. 2016b). Within Chapter 3 of this thesis, an extension of the traditional MM will be proposed to account for the actual sequence of contact line propagation by modeling a forced imbibition process.

2.2.2 Dynamic Pore-scale Modeling

When directly computing multiphase flow the interaction between capillary and viscous forces are explicitly taken into account. Therefore, some sort of time scale needs to be introduced to account for the evolution of the flow field. From the methods discussed so far, only dynamic PNM and the LBM provide a numerical solution for the direct computation of multiphase flow.

In dynamic PNM either single-pressure or two-pressure algorithms are used for computing multiphase flow. The first only accounts for a single pressure within a pore body, even though it might be occupied by two fluids. The volumetric flux between two pore bodies is calculated by applying an analog of the Washburn equation. While this is computationally very attractive, the method is limited to non-angular cross-sections for the pore throats (Al-Gharbi und Blunt 2005). Furthermore, depending on how the pore occupation with fluids is handled, one might run into problems how to formulate the force balance with neighboring pore bodies.

Aware of the limitations and with increasing computational capabilities more recent studies are using the two-pressure algorithm, where each fluid gets an individual pressure assigned. In contrast to the single-pressure approach, the volumetric flux between two pore bodies is then solved for each individual fluid phase, e.g., allowing to account for film flow within the corners of a pore throat. By distinguishing between the individual phases local displacement potentials can be calculated incorporating the associated pressure drop from capillary, viscous and gravitational forces (Aghaei und Piri 2015).

A comprehensive study on the individual assumptions and limitations of the approaches can be found in the review of Joekar-Niasar and Hassanizadeh (Joekar-Niasar und Hassanizadeh 2012). Even newer publications refer to this study as the main principle has not changed, which relies on the calculation of the (individual) phase conductivity and pressure drop for solving the

volumetric flux. Including a time scale, this leads to an increased simulation effort scaling with $mn \ln n$, with m being the number of re-computations and n being the number of elements (pore throats and bodies) (Blunt 2017).

A variety of LBM models for solving multiphase flow has been proposed by researcher groups, which are covered in the review of Liu et al. (Liu et al. 2016). Since each method relies on a different simulation principle, the focus will be constrained to the color gradient model as used in McClure et al. to deliver a complete picture for an exemplary simulation package (McClure et al. 2021). The model is defined by three lattice Boltzmann equations based on a D3Q19 discretized velocity set, which models the mass and momentum transport. At each time step the propagation, population, collision, external forces and two-phase step is calculated. Therefore, the density, velocity and pressure/stress of the fluids are known at any given point. Based on the color gradient the fluids are moving and redistributed at each time step, coupling the interface interactions and solving the flow of the fluids. The number of velocity sets and simulation steps indicate the computational effort needed and the amount of data created for a single time step.

Table 1 Comparison of three common pore-scale simulation methods on the basis of multiphase displacement and flow modeling aspects

	Morphological Method	PNM		Lattice Boltzmann
		Quasi-static	Dynamic	
Structure	Actual Structure	Idealized Structure		Actual Structure
Simulation effort*	low to medium	low	medium	high
Time component	quasi-static	quasi-static	dynamic	quasi-static and/or dynamic
Displacement Modeling	Mathematical morphological operations	Rule Based; force balancing		simplified interface tracing (e.g., color models) or free-energy model
Wettability modeling	discrete contact angles directly assignment to voxels	CA distributions e.g., pore-based wetting index		High degree of modeling approaches, typically wetting map
Flow simulation	Solving (Navier-)Stokes on the structure	Solving hydraulic conductivities (e.g., Hagen-Poiseuille, Washburn)		approximating Navier-Stokes flow via solving collision dynamics of fluid packets
Degrees of Freedom	low	intermediate	high	high
Input needed	low	intermediate	intermediate to high	high
Limitations	Does not capture dynamic effects, cannot handle neutral wetting conditions	Relies on a proper network extraction		Physics need to be understood Limited structure sizes
Comments	Incorporated in other simulation models	a lot of learnings about pore scale displacements in the past		

*Simulation time cannot be directly compared since the individual methods rely on different hardware (e.g., CPU and GPU)

2.3   Topology in Porous Media

Characterizing transport mechanisms and the exact arrangements of fluids within a porous medium are of key interest. With the recent progress of imaging technologies and the evolution of computational power, the investigation of in-situ displacements and trapping events has become feasible and has been captured and evaluated in various studies (Berg et al. 2013; Berg et al. 2016b; Garing et al. 2017; Rücker et al. 2015; Scanziani et al. 2020). However, such experiments require a lot of experience, time and are often limited to a restricted field of view, a direct correlation of fluid-phase properties in different porous media is difficult. From a conceptual point of view property correlation between different porous media and the fluids therein is an elementary question.

In the past, different researchers have found relationships, e.g. between porosity and permeability for similar rock types or measures to characterize porous media (Leverett 1941; Tiab und Donaldson 2015; Sahimi 2011). However, with regard to more complex topics, such as carbonate rock structures those simple relationships break down (Dullien 2015). The interest is therefore to find a complete characterization, which can uniquely describe a system. Geometric state functions could potentially offer a more refined definition and deeper insights (Armstrong et al. 2019; Hilfer 2001). State functions are the sole means of comparing microscopic states. The robustness of this comparison is pivotal because, even in experiments and simulations that appear comparable, different microstates are observed - the exact saturation distribution is never identical. This discrepancy underscores the need for a reliable mechanism to compare and analyze these microstates.

Emerging from the field of statistical physics the Minkowski functionals (MF) have been introduced with the potential to characterize both, the fluid phases and pore geometry (Mecke und Stoyan 2000). Hadwiger's theorem states that a set of four invariant measures can be used to completely quantify a three-dimensional (3D) geometry (Hadwiger 1975). For multiphase porous systems, these measures have proven to be the volume of the pore space V, surface area between the phases S, integral mean curvature of the phases κ and Euler characteristic of an individual phase χ. The relationship between these measures is then stated in the MF. Below, the four MF are given describing a 3D space, e.g., porous media structure

$$M_0 = \phi V \qquad\qquad [\,5\,]$$

$$M_1 = \int dS \qquad\qquad [\,6\,]$$

$$M_2 = \frac{1}{2} \int \left(\frac{1}{r_1} + \frac{1}{r_2} \right) dS = \frac{1}{2} \int \kappa dS \qquad\qquad [\,7\,]$$

$$M_3 = \int \frac{1}{r_1 r_2} dS = 4\pi\chi \qquad [\,8\,]$$

where ϕ is the porosity, r_1 and r_2 are the principal radii of curvature. The Euler characteristic can essentially be reduced to a counting exercise and can be calculated from the Betti numbers, which are defined as the number of objects (N), number of loops or holes (L) and number of voids (O).

$$\chi = N - L + O \qquad [\,9\,]$$

As stated earlier, the geometric state functions of a system are investigated with respect to closing the missing link between microscopic and macroscopic multiphase displacement events. It was already shown that there is an existing link between multiphase displacements and the MFs of a system (Liu et al. 2017; Schlüter et al. 2016; Armstrong et al. 2016; Vogel 2000; Herring et al. 2013; Ruecker et al. 2015). More specifically the Euler characteristic provides an opportunity to describe the connectivity of a phase, hence indicating the relative permeability of a system. However, it still remains open how complete this description for predictive purposes is. Therefore, another approach is to reduce uncertainties by using topological computations as validation for more complex simulations (McClure et al. 2020). Investigating interim results for trends and uncertainties can strongly reduce the overall simulation effort. Furthermore, it was shown that complex displacement processes, such as oil recovery by alkaline flooding, can be characterized by computing the fluid topology (Ott et al. 2020). Subsequently, allowing for the potential to screen such systems for their optimum displacement conditions.

In modeling, there is a susceptibility to the risk of overfitting models, as the degree of freedom is much higher than that of experimentally derived data. Topological measures can elevate validation to a different level, as they produce unique fingerprints that can be used to check the correctness of data. Exemplarily Arnold et al. has shown simulated and experimental data can be compared on basis of relative permeabilities and the Euler characteristic of the fluid phases (Berg et al. 2016b; Arnold et al. 2023); in detail it was shown that different simulation approaches lead to similar relative permeabilities while consisting of different fluid configurations.

Chapter 3

Method and Method Developments

The morphological method (MM) allows the population of a porous domain with different phases, enabling the modeling of displacement processes, such as drainage and imbibition at relatively low computational cost. Simulating a displacement process results in a sequence of quasi-static saturation states. The method is rule based and is linked to capillarity with viscous effects being neglected. During the displacement process the invasion of a phase is governed by the structure and wettability, i.e., contact angle. Throughout this chapter, the terms wetting phase (WP) and non-wetting phase (NWP) are used, which imply contact angles below 90° and above 90° respectively.

The MM employs morphological operations on pore-scale rock images based on mathematical morphology. It was first developed by Matheron and Serra in 1964 during Serra's PhD thesis, and subsequently published in Serra et al.'s 1982 paper (Serra 1982). By utilizing basic dilation and erosion operations on the rock's pore structure, the MM enables a quantitative analysis of pore geometries with respect to drainage displacement thresholds – the pore throats. The identification of thresholds through morphological means connects the pore structure to capillarity and fluid displacement physics through the YL equation. The original mathematical concepts underlying the MM are thoroughly discussed in the paper by Hilpert and Miller from 2001 (Hilpert und Miller 2001). Originally, the approach was restricted to binary images but can now be applied to greyscale images as well (Heijmans 1995). A variation of the MM called the pore MM or maximum inscribed spheres (Silin und Patzek 2006), can predict the distribution of wetting and non-wetting phases inside a porous medium.

The MM primarily relies on geometrical rock properties to predict saturation changes and therefore assumes that capillary forces are more dominant than viscous forces, which means it describes displacements at low capillary numbers (Hazlett 1995). To distribute the two fluid phases, the method employs morphological operations rather than partial differential equations. A reservoir connection of the pores is essential for an invasion to occur (Becker et al. 2008; Hilpert und Miller 2001). In addition, a criterion for a displacement event is the separation from the respective wetting and non-wetting reservoirs (as described further below) that are

connected to the system boundaries, allowing for the formation of residual saturations (Ahrenholz et al. 2008). The terms imbibition and drainage describe the invasion of the WP and the NWP, respectively. Simple image operations on the segmented pore and fluid structures modify the topology of the fluid phases, which corresponds to a capillary pressure change, where the extent of the dilation operation corresponds to the pore throat radius in the Young-Laplace equation. The dilation of voxels in an image corresponds the radius r, indicative of the pore throat dimensions during a drainage process. Subsequent to Schulz's work, distinct contact angles are factored in by adjusting the dilation radius using the $\cos\theta$, where θ represents the contact angle (Schulz et al. 2015). However, this approach has a tendency to slightly exaggerate the true contact angle, proving it ineffective for contact angles nearing 90°.

Throughout this thesis, the simulation and modeling software GeoDict by Math2Market was used. The drainage and imbibition modeling has been performed using the SatuDict module. In the next chapters, the general definition and basic displacement algorithms are described. Within the software, more advanced options and constraints can be applied for more realistic modeling.

3.1   Drainage

A drainage is defined as the displacement of the wetting phase by the non-wetting phase in an immiscible manner. During a drainage, the capillary pressure is monotonically increasing. Figure 5 shows a simulated primary drainage curve for a Berea sandstone sample. Each of the data points represents a capillary equilibrium state. The capillary pressure increases until the maximum pressure is reached, defining our residual saturation (left of the red line).
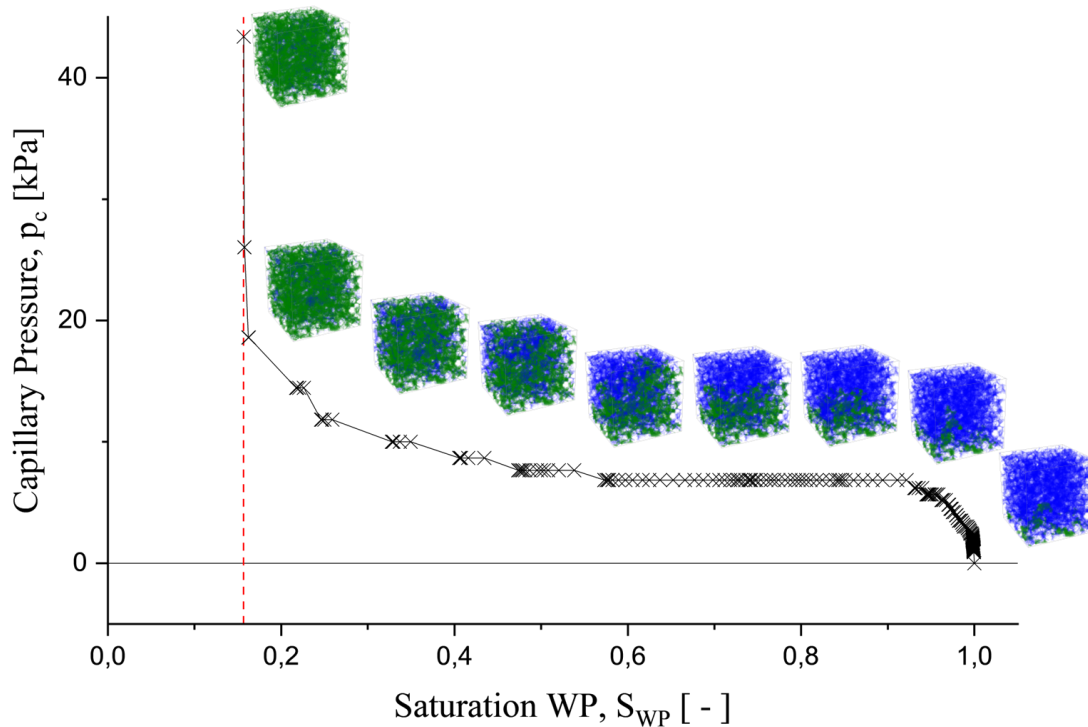
Figure 5 Primary drainage capillary pressure curve simulated from a segmented pore scale image of Berea sandstone rock. The dashed red line indicates the residual saturation. The cubes show the fluid configuration, with blue being the displaced wetting phase by the green non-wetting phase.

3.1.1 Primary Drainage

A primary drainage process initiates with the system being initially fully saturated by the non-wetting phase NWP. When an external pressure is applied a displacement event can take place. The displacement threshold is set by the capillary pressure of the system, which is governed by the microscopic pore structure, more specifically the pore throat size distribution, and wettability of the system. The interfacial tension is only accounted for in a post-processing step. The quasi-static nature of the MM results in a stepwise population of the model, which is constraint by the boundary conditions set.

When modeling mercury injection capillary pressure (MICP) all boundaries are defined as non-wetting reservoirs. This allows an invasion from all sides, while the displacement is entirely governed by the pore structure. The simulation concludes when the entire domain is saturated with the NWP, leaving no residual phases. In this context, the displacement is not limited to the phase connected to the domain boundary. It assumes that the displaced phase, specifically air in this case, is compressible and therefore does not need to exit the porous domain at the boundary. This enables the identification of the pore throat size distribution based solely on geometric characteristics.

When modeling a primary drainage with an inlet and outlet the displacement is constraint by the wetting and non-wetting reservoir. A displacement can only take place as long as the WP is still connected to the wetting reservoir(s). As soon as a phase is disconnected it is considered residual and can no longer be displaced. The tangential boundaries are typically either considered as a wetting reservoir or symmetric to ensure the invasion is only limited to the inlet. The drainage modeling is finished, when either no WP is left, or the WP is entirely disconnected from the WP reservoir.

The maximum capillary pressure obtainable is defined by the resolution of the system, as a voxel defines the minimum pore throat diameter. Applying the Young-Laplace equation [1], with r being half of the resolution of a voxel, the maximum modellable capillary pressure can be calculated.

3.1.2 Drainage Modeling Implementation

The drainage process is described by a sequence of equilibrium steps resulting from dilation operations and connectivity checks. Figure 6 shows a simplified illustration of the drainage algorithm for a single CA, resulting in a capillary pressure curve as shown in Figure 5. The models are initially 100% saturated with the WP and the NWP is invading from the left side of the images. Top and bottom of each image are considered as no-flow boundaries. The basic algorithm for modeling a morphological drainage process can be described by four steps (Arnold et al. 2022; Arnold et al. 2023):

1. **Dilation 1:** Dilation of grains into the WP-saturated pore space by a voxel radius r, which can be scaled by $\cos(\theta)$.

2. **Connectivity 1:** Recolor* the pore space that is connected to the NWP reservoir and label it as NWP.

3. **Dilation 2:** Dilate the NWP by the initial (non-scaled) voxel radius from step one.

4. **Connectivity 2:** Identify all WP disconnected from the WP reservoir as residual – it will no longer be considered for further displacement calculations.

*The term "recolour" in this context refers to the process of reassigning the phase in the illustrated images.
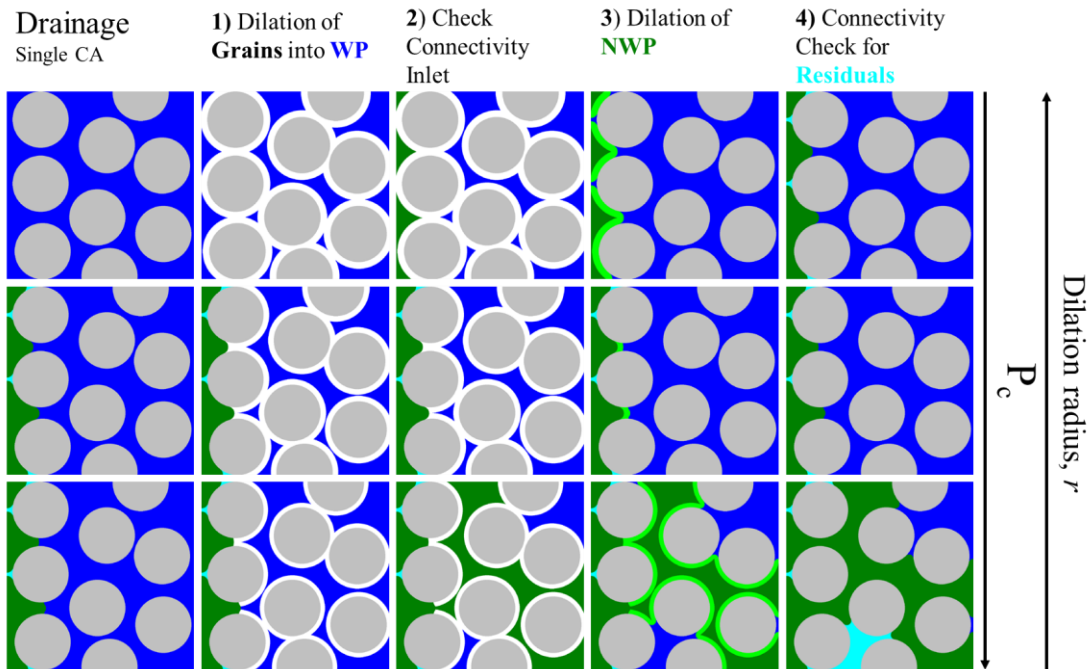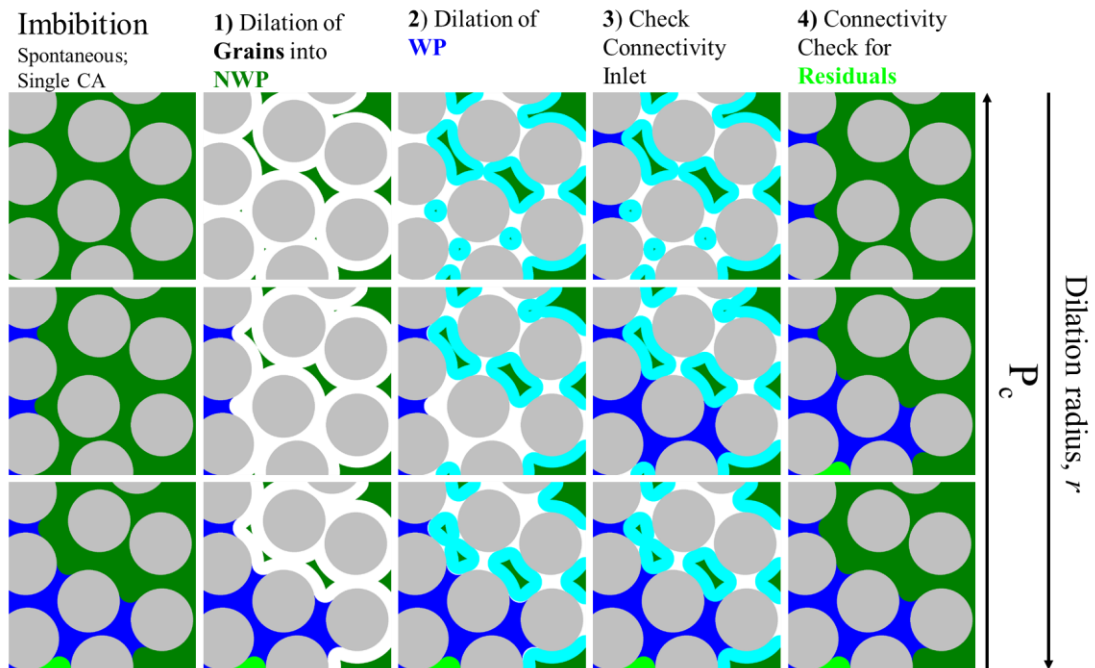
Figure 6 Simplified 2D illustration of the basic drainage algorithm for a single contact angle (CA) showing an invasion from the left side of the images. Blue is the displaced wetting phase, white represents the dilation of the grains, green the invading non-wetting phase, light green the dilation of the non-wetting phase and cyan representing a residual wetting phase, assuming that an outflow can only happen on the right side of the image. The capillary pressure, p_c, increases during the drainage, top to bottom.

The capillary pressure, p_c, increases in conjunction with the decreasing dilation radius top to bottom. Figure 7 shows the same algorithm for multiple materials, hence, contact angles. The contact angle of the brown material in the illustrated case is 40° which is used for the scaling of the dilation radius. In both figures, the same dilation radii for each equilibrium step were chosen. It shows that for the same capillary pressure different saturations and ultimately different invasion pathways are chosen. A higher contact angle will result in a reduced capillary pressure needed for overcoming the same pore-throat size.
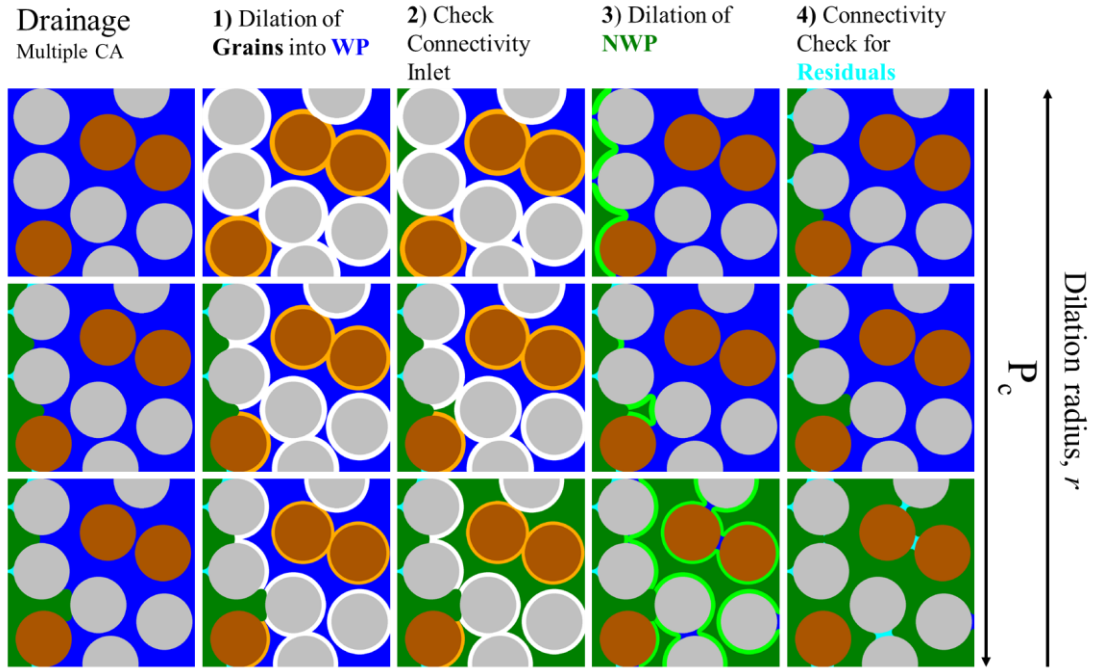
Figure 7 Simplified 2D illustration of the basic drainage algorithm for multiple contact angles showing an invasion from the left side of the images. Where blue is the displaced wetting phase, white and light brown are the dilation of the grains, green the invading non-wetting phase, light green the dilation of the non-wetting phase and cyan representing a residual wetting phase, assuming that an outflow can only happen on the right side of the image. The contact angle of the brown grain is higher than that of the grey grain, therefore the dilation voxel of the white and light brown are different. The capillary pressure, p_c, increases during the drainage, top to bottom.

3.2   Imbibition

Within this thesis, the imbibition displacement process is defined as the displacement of the non-wetting phase by the wetting phase. The imbibition is distinguished in a spontaneous and a forced part, whereas for the later the algorithm was modified in the frame of this thesis. In general, an imbibition process is more complex than a primary drainage, as it is not only dominated by local capillary effects but also includes viscous effects. In chapter 2.2.1 the quasi-static pore modeling approaches and their constraints to capillary-dominated processes were discussed. So far the MM was limited to spontaneous modeling only, which lead to early cut-offs of the NWP, reduced saturation ranges and mismatches with experimental data (Berg et al. 2016b). Therefore, a new modeling approach has been proposed and tested for overcoming previous limitations. Figure 8 shows the entire imbibition process modeled, starting from the endpoint of a primary drainage, ergo residual saturation. The blue line represents the spontaneous and the red line the forced part of the imbibition curve. For illustration purposes, the Berea sandstone was modeled assuming mixed wetting conditions, so both processes make up a distinct part of the imbibition curve. Each data point stands for an equilibrium state.
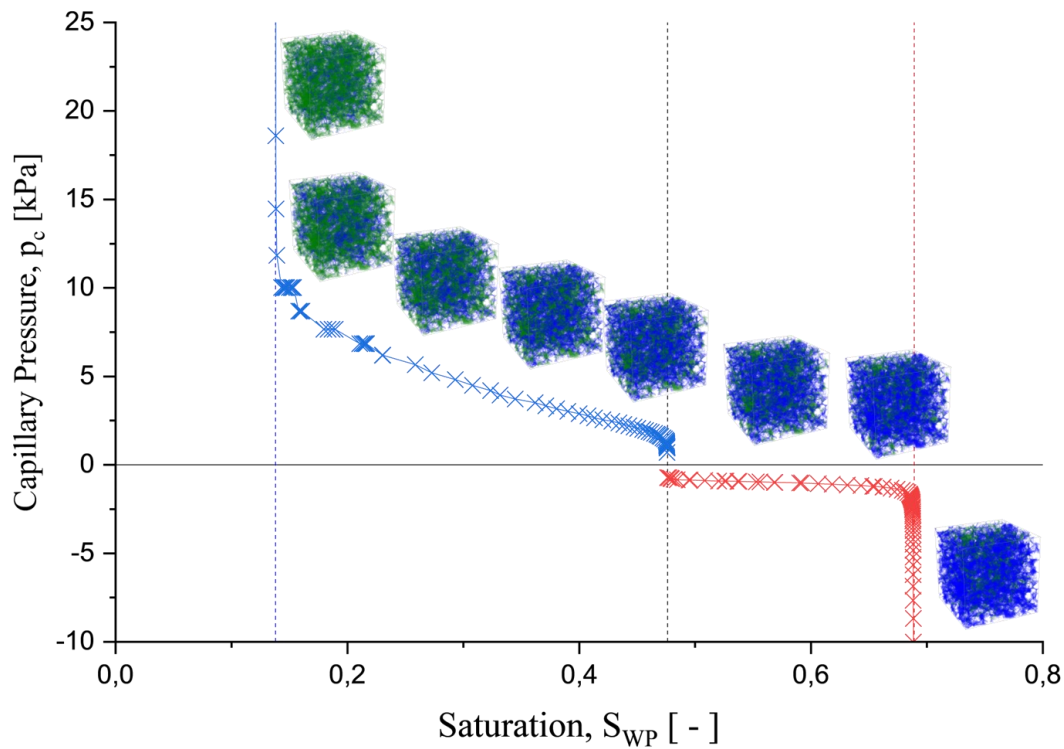
Figure 8 Exemplary imbibition capillary pressure curve of a Berea sandstone, starting at a residual wetting saturation, assigning mixed wetting conditions. The capillary pressure is monotonically decreasing, with increasing wetting saturation. The residual saturations are indicated by the dashed blue and red line respectively. For the saturation range between the blue and black dashed lines a spontaneous imbibition was modeled, whereas for the saturation range between the black and red dashed lines a forced imbibition was modeled. The cubes show the fluid configuration, with blue being the wetting phase that displaces the green non-wetting phase.

3.2.1 Spontaneous Imbibition

A spontaneous imbibition is defined as a process where fluid displacement takes place, without external forces being applied. It is indicated by the positive part of a capillary pressure curve, which monotonically decreases with increasing wetting phase saturation. An illustrative example would be the soaking up of water by a sponge. The sponge, a porous medium, is initially filled with air (NWP) which is displaced by water (WP). In porous media flow, the model is typically not 100% saturated with a NWP but has already a WP residual. Typically, the end of the primary drainage is used as starting point for the imbibition modeling. Contrary to the primary drainage, the imbibition is rather controlled by the retracting NWP, which predominantly sits in the larger structures, i.e., pore bodies. The process is therefore rather controlled by the pore bodies than the pore throats, which is modeled by the dilation curvature around the retracing NWP.

3.2.2 Spontaneous Imbibition Modeling

Similarly, to the drainage process, a spontaneous imbibition is described by a sequence of equilibrium steps resulting from morphological operations. The drainage algorithm is hereby slightly modified by interchanging the dilation step 2 with the connectivity check 1 (Arnold et al. 2022; Arnold et al. 2023).

1. **Dilation 1:** Dilation of grains into the WP-saturated pore space by a voxel radius r, which can be scaled by $\cos(\theta)$.

2. **Dilation 2:** Dilate the NWP by the initial (non-scaled) voxel radius from step one.

3. **Connectivity 1:** Recolor* the pore space that is connected to the WP reservoir and label it as WP.

4. **Connectivity 2:** Identify all NWP disconnected from the NWP reservoir as residual – it will no longer be considered for further displacement calculations.

*The term "recolour" in this context refers to the process of reassigning the phase in the illustrated images.

Figure 9 Simplified 2D illustration of the spontaneous imbibition algorithm for a single contact angle (CA) showing an invasion from the left side of the images. Blue is the invading wetting phase, white the dilation of the grains, cyan the dilation of the wetting phase, green the displaced non-wetting phase and light green representing a residual non-wetting phase, assuming that an outflow can only happen on the right side of the image. The capillary pressure, pc, decreases during the imbibition, top to bottom.

Figure 9 shows a 2D illustration of the altered drainage algorithm to model a spontaneous imbibition. The model is initially 100% saturated with a NWP, with the WP invading from the left side of the images. Top and bottom of the image are considered as no-flow boundaries. In contrast to the drainage algorithm, the imbibition modeling starts with a small dilation radius, which increases with each step. The capillary pressure is therefore decreasing top to bottom. In the illustration, a rather large dilation radius was chosen for the sake of illustration purposes.

A spontaneous imbibition (SI) simulation stops when either the entire NWP is disconnected from the NWP reservoir(s) or when the dilation radius exceeds the largest pore size. While the physics of a SI seems to be correctly captured, the end state of the process comes with the downside of having an entirely disconnected NWP, resulting in an effective permeability for the NWP of zero. However, based on experimental observations (Berg et al. 2016b), it is known that the connectivity of the NWP can be present for almost the entire saturation range, especially in smaller domains. Therefore, in addition to the forced imbibition (FI) modeling an additional stopping criterion needs to be introduced, ensuring a connectivity of the NWP at the end of a SI process. Non-wetting material prevents the SI front from advancing, as it restricts the dilation process at those areas, avoiding a displacement. Therefore, the possibility was implemented to imply another stopping criterion by introducing non-wetting material before the start of SI modeling. This gives the control to deny access to parts of the domain, hence displacement of NWP.

3.2.3 Forced Imbibition

The forced imbibition connects directly after the SI is finished. Here, similar to the primary drainage, an external pressure is needed for a displacement of the NWP. The end of a forced imbibition is marked when the residual non-wetting saturation is reached. The abrupt p_c change, visible as discontinuity in Figure 8, is a result of the finite morphological modeling operations which can never start or stop at zero as it would imply an infinitely large morphological operation radius. Furthermore, for some cases, a rather large saturation jump can be observed between the transition saturation point and start of the forced imbibition modeling. These effects are more dominant for smaller domains, e.g., a single capillary as illustrated in Figure 10. It is believed that this discontinuity is locally and physically correct and that it diminishes with increasing domain size. The underlying argument is that for an increasing scale, the saturation state is less and less dominated by single pore-scale events. As a result, the transition smoothens out as a function of domain size.
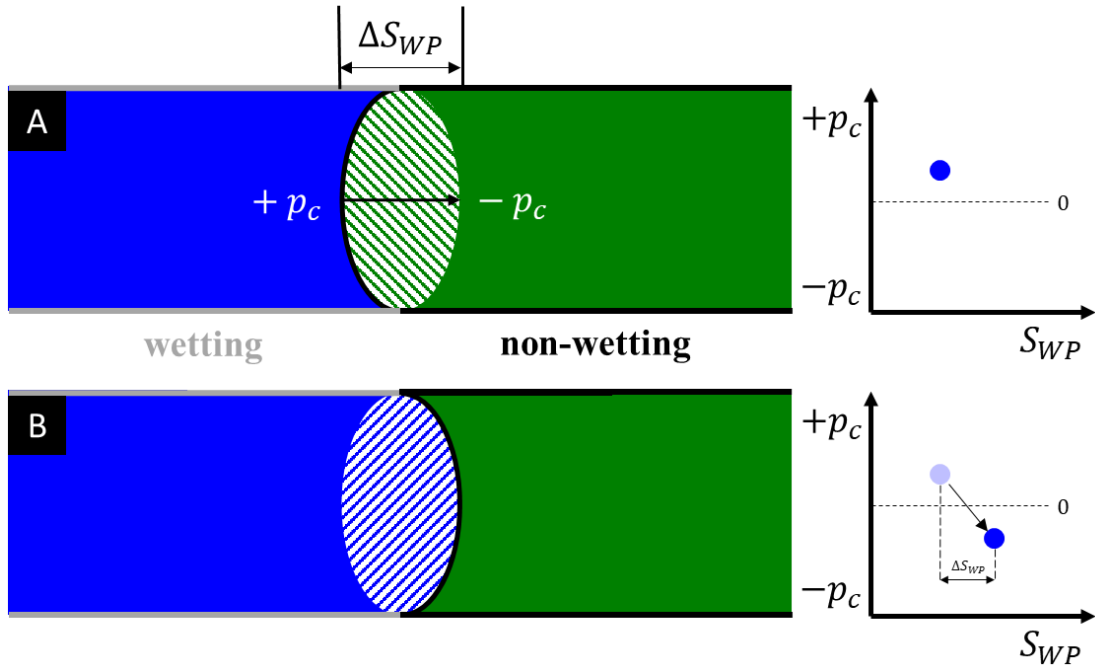
Figure 10 2D illustration of a single capillary with wetting (grey) and non-wetting (black) conditions, where the meniscus between two immiscible phases is folding over (A to B). The blue color represents a wetting phase and the green color a non-wetting phase. The folding over would correspond to a capillary pressure and saturation jump between two quasi-static states (right graph).

3.2.4 Forced Imbibition Modeling

The displacement during a forced imbibition is assumed to be similar to that of a drainage. The principal idea is, therefore, to model the forced displacement with the drainage algorithm, by switching the wetting and non-wetting roles at the end of the SI. This switch allows a forced modeling of the NWP displacement by the WP. As the displacement conditions are the same as for the primary drainage modeling, a connectivity of the NWP with the outlet is necessary for further displacements. Therefore, an additional stopping criterion, in form of non-wetting material is introduced. As the introduction of non-wetting material is connected to a wettability alteration, it is thoroughly discussed in chapter 3.3.

In the forced imbibition (FI) process, the drainage algorithm is utilized, with the contact angles and the roles of the phases inverted. Specifically, a non-wetting contact angle is treated as wetting (i.e., $180° − α$) for the FI drainage process, while the roles of the WP and NWP are swapped. This signifies a menisci transition between the WP and NWP as the displacement process shifts from spontaneous to forced.

3.3   Modeling Wettability Heterogeneity

In the MM the wettability is defined by assigning discrete contact angles within the porous structure. Contact angles can be distributed within the system, either on the basis of the segmented image or by a stochastic or deterministic approach. As mentioned earlier, the applicability of the MM is constrained by the number of different CA that can be represented, which in turn is limited by the number of materials. The number of materials is typically determined during the initial segmentation process, but it can be expanded further, limited only by the image type used for modeling. In Figure 11 the invasion of pore space with two different solid materials (grey and brown) characterized by two different contact angles, with $\theta_{grey} < \theta_{brown}$, is shown.
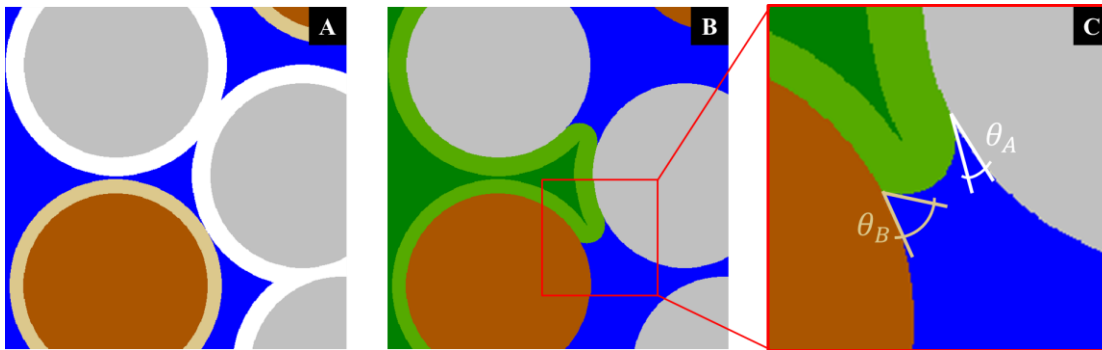
Figure 11 2D illustration of the MM for two different materials (grey and brown) for which two different contact angles ($\theta_A < \theta_B$) are applied. Image C shows the resulting contact angles for an invading non-wetting front.

Image A shows the different dilation radii, which are followed by an invasion from the left side of the image into the first pore. The subsequent dilation of the NWP (image B), results in two different advancing contact angles, which are shown in more detail in image C. The scaling of the dilation radius by the cosine of the contact angle leads to a slight overestimation of the modeled contact angle.

In order to implement different wetting conditions, different materials and subsequently wetting states need to be introduced. For drainage simulations, the invasion paths are only slightly altered when multiple contact angles are introduced, as the process is mainly governed by the structural properties, i.e., pore throat size distribution. The focus throughout the next chapters is therefore put on the imbibition displacement process and the effect of wettability alteration.

As discussed in chapter 3.2.2 non-wetting material as an additional stopping criterion needs to be introduced to be able to model a full-scale imbibition process. Throughout this thesis two approaches are chosen, one on a deterministic basis, the other on a stochastic one. In chapter 2.1.1 it was already discussed, that even for a single material a range of contact angles can be

assigned. Therefore, a stochastic distribution of contact angles and non-wetting material was investigated to observe its influence on the imbibition process, as well as on the overall wetting conditions of the system. The material is introduced with a defined region size and is generated based on an isotropic Gaussian random field. The field threshold is defined by the solid volume percentage (SVP), which is introduced.
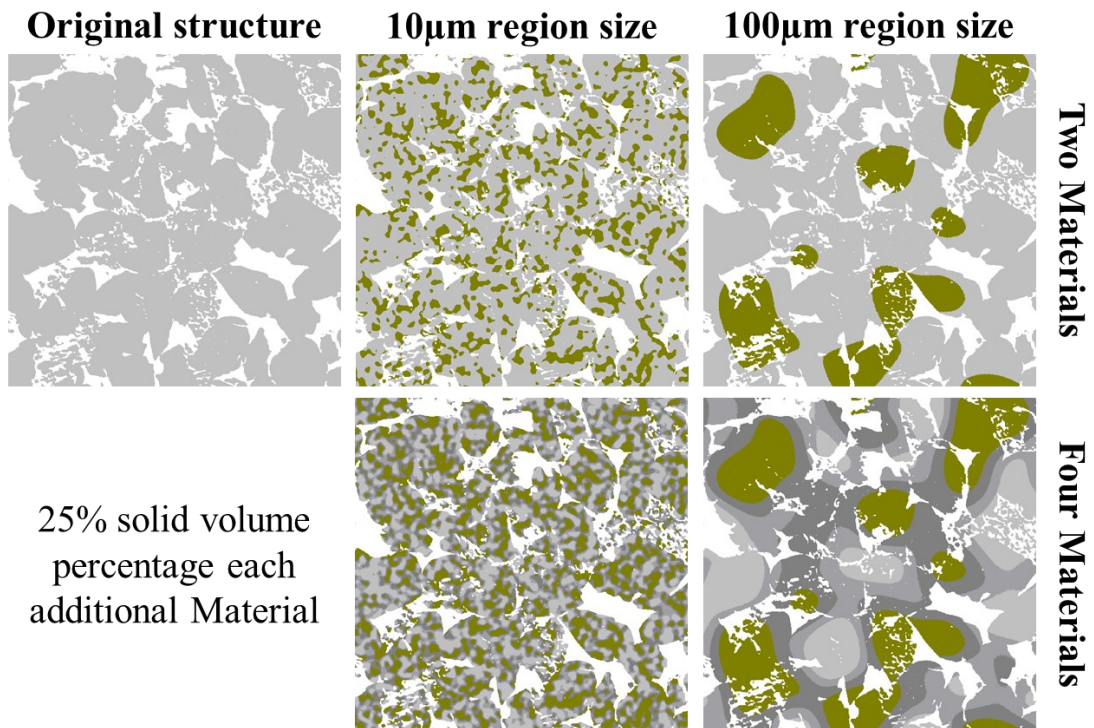
Figure 12 Illustration of introduced material based on the stochastic approach on a digital twin (top left) of the size 1100x1100 µm. The golden material and grey shades materials correspond in all images to 25% solid volume percentage (SVP), with different region sizes of 10µm (middle) and 100µm (right).

By employing the same random seed, but varying the SVP, it is possible to introduce multiple contact angles, with a smooth transition between them. For the introduction of non-wetting material, the stochastic distribution is already applied before the drainage process, influencing both the drainage and imbibition displacement process. The stochastic approach might not represent the actual attributes of a single material, however making the implementation less user biased as it entirely depends on the topology and volume. The material incorporated can form connections across the entire structure, the extent of which is dictated by the region size and volume. The proportion of the material altered in volume is equivalent to the surface area percentage between the solid and pore material, with only minor discrepancies. Figure 12 illustrates the stochastic approach with one (top) and three (bottom) materials introduced on a digital twin. Exemplary two different region sizes are shown, which represent a size below (10µm) and above (100µm) the average grain size visible.

The deterministic approach stems from the natural alteration of wettability that occurs as a result of an aging process. An aging process assumes that mineral surfaces in contact with the NWP can alter their initial wetting state (Hirasaki et al. 1990; Wael Abdallah et al. 2007; Rücker et al. 2020). In contrast to the stochastic approach, non-wetting material is introduced at the end of the drainage process. Based on an algorithm that analyses the pore size distribution, non-wetting material is introduced only in areas where it comes in contact with the NWP from the drainage, while prioritizing the biggest pores first. The pore space considered (PSC) is used as an input parameter to define the volume of pores considered for the implementation of non-wetting material.
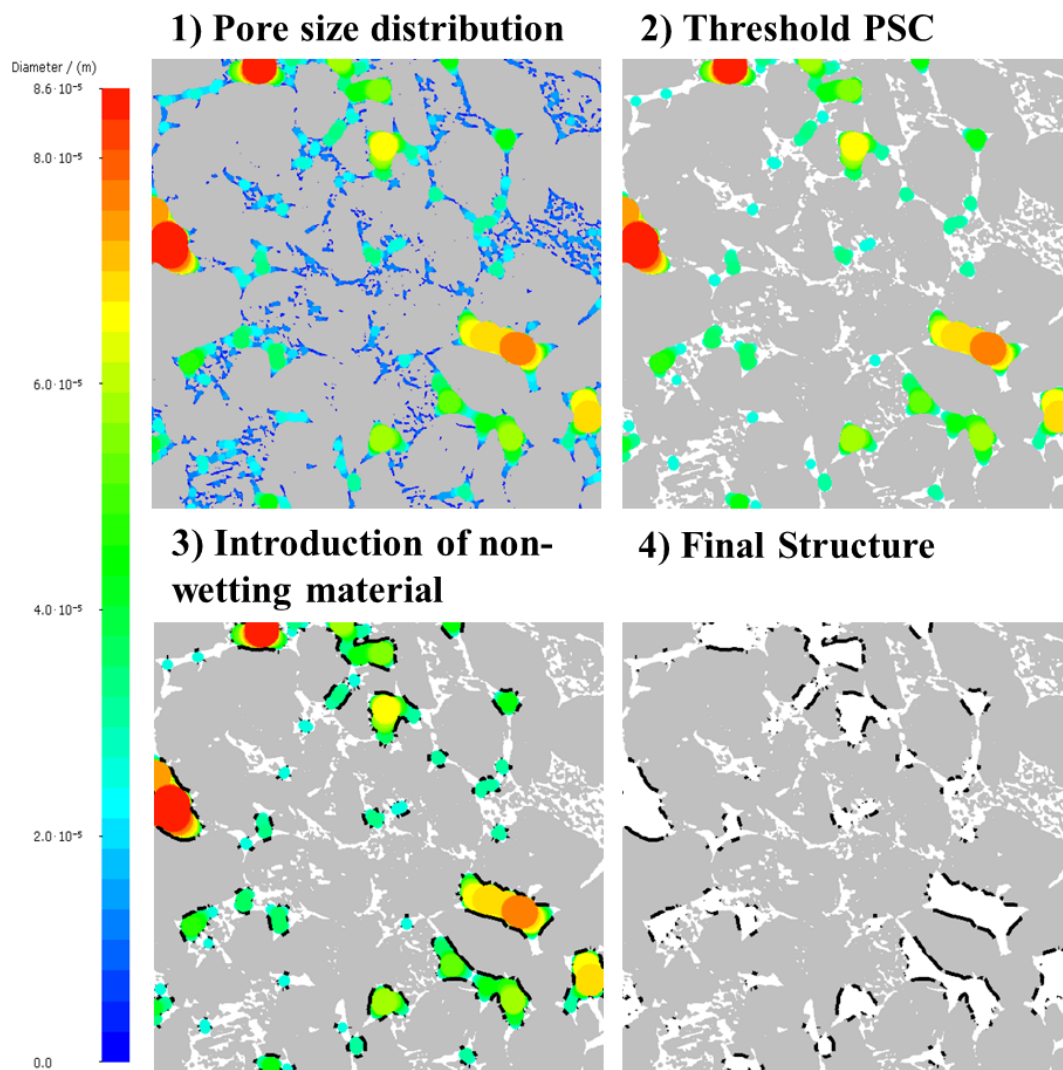
Figure 13 2D illustration of the deterministic algorithm for the introduction of non-wetting material. After the pore size distribution (1), a threshold of pore space considered (PSC) is set (2), which defines the pores which are considered for implementation. Image (4) shows the final structure with the non-wetting material, in image (3) it can be seen that the larger pores are prioritized. The structure has a size of 1100x1100 μm.

The volume percentage does not equal the surface area percentage, as only parts of each pore change wetting-state. Figure 13 shows the deterministic algorithm on a 2D structure. The calculated pore sizes are represented by a volume field, which is color-coded using a hue-saturation-lightness legend. In this representation, blue signifies the smallest pores, while red indicates the largest ones. The last two images show the implementation, based on a PSC threshold of 50%. It is assumed that the entire structure was filled with the NWP.
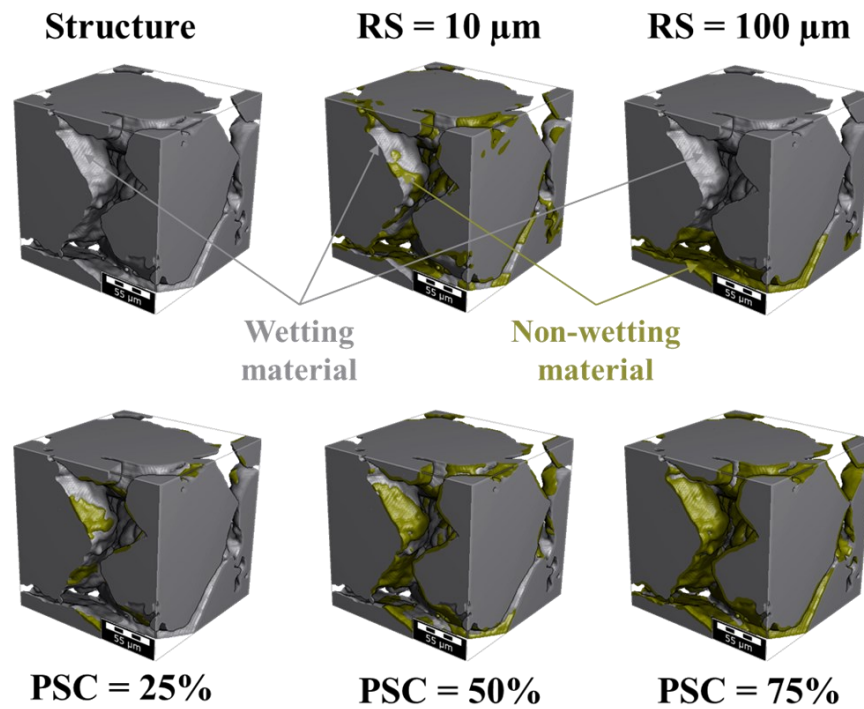
Figure 14 3D visualization of both approaches on a smaller scale.

Figure 14 shows the implementation of both approaches on the same structure in 3D. The top of the image refers to the stochastic approach with two different region sizes, which shows that the introduction within the pore body is random. The bottom images show a pore body, which is considered for all thresholds, however the larger the threshold (high PSC value) the more non-wetting material is introduced in the structure.

3.4 Computing Relative Permeability via Stokes Flow Simulation

All flow simulations were performed with the FlowDict module from GeoDict, using the Left Identity Right (LIR) solver (Linden et al. 2015). Each simulation is performed, by assigning a constant pressure drop along the flow direction. The solver calculates the flow velocity field, by solving the (Navier-)Stokes equation. For each simulation a very small pressure drop of 0.02 Pa is assigned, therefore resulting in a linear relation between the pressure drop and mean

velocity. This allows the neglect of the inertia term and therefore solving Stokes flow only, performing much faster while delivering similar results compared to solving Navier-Stokes. The average absolute difference for a single-phase permeability is around 0.02 ± 0.01, with the Stokes solver slightly overestimating while reducing the average simulation time by a factor of 2 (valid for a 600^3 voxels domain).

The boundary conditions in flow and tangential direction are defined as periodic with adding an implicit region of 10 voxels at the in- and outflow. The effective flow is simulated separately for each fluid phase, taking into account only the connected pathways specific to that phase. In these simulations, the other phase is treated as immobile, considering all internal boundaries as rigid and fixed. As a result, viscous momentum transfer between the fluid phases is disregarded, meaning that the movement of one phase does not impact the movement of the other fluid phase (Blunt 2017).

3.5   Topology Computation

The topology of the structure and phases are computed by using the MatDict module from GeoDict and the MorphoLibJ plugin from ImageJ (Legland et al. 2016). The MatDict module delivers all four Minkowski functionals based on the estimation of the real surface area. It is computed by using a staggered grid and statistical image analysis (Math2Market 2022). However, for the evaluation of the results, only the surface area and curvatures are considered, as the Euler number is computed separately. Furthermore, all results are normalized by dividing the results by the total volume, which will be referred to as specific. The Euler number and cluster size analysis are separately computed with MorphoLibJ. Each phase (wetting and non-wetting) is separately segmented, labeled and then analyzed. Connected components, hence individual clusters, are identified by a labeling algorithm using a 26-connectivity. After the identification of each cluster, the volume and Euler number are computed.

Chapter 4

3D Structure and Properties of Rock Samples

In this chapter, the porous structures investigated in the context of this study will be introduced. All samples are sandstones with different pore and grain size distributions. The four structures are acquired from micro computed tomography imaging and are reconstructed and segmented. For the segmentation the machine learning algorithm software Ilastik was used (Berg et al. 2019). Example images of the digital rock structures are shown in Figure 15. In a first step, the properties of the samples are analyzed. Even though all samples are sandstones, each of the rock structures exhibits different petrophysical and topological properties.

| Berea 1 | Berea 2 | Bentheimer | Fontainebleau |
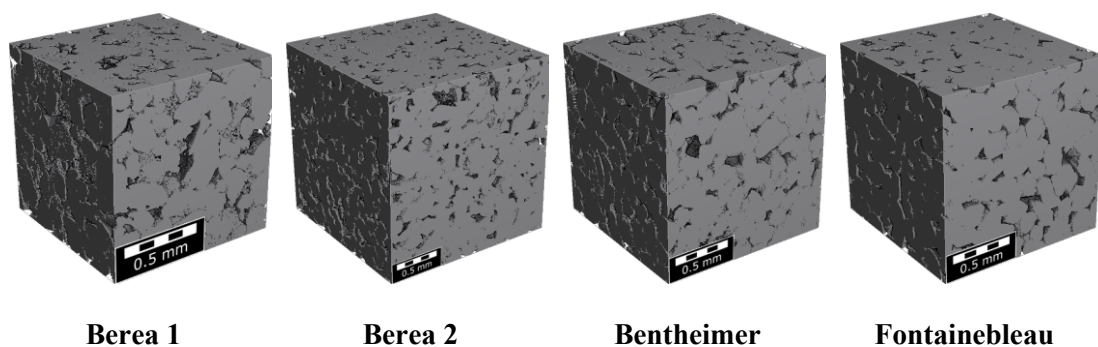
Figure 15 3D porous media images of the real rock digital twin structures. Each structure has a size of 600³ voxels, with different voxel sizes.

The Berea sandstone has a relatively homogenous mineral composition and grain size, in combination with being a host to oil and gas, it has already been intensively studied with respect to porous media flow and is therefore often used in core flooding experiments and for digital rock computations (Pepper et al. 1954; Churcher et al. 1991; Ma und Morrow 1994). Berea, as an outcrop material, offers an abundant supply, making it highly suitable for conducting a wide range of studies. The well-established understanding of Berea further enhances its value as an excellent choice for testing new methodologies. In this study, two different Berea samples are being used, which were imaged with two different resolutions. The Bentheimer sandstone is also frequently used for laboratory studies, due to its homogeneous nature and well-sorted grain framework (Peksa et al. 2015). It serves as well as a reservoir for oil, which peaked the initial interest in the characterization of the rock. The sample used in this work comes from an outcrop.

The absence of clay makes the Fontainebleau a unique sandstone that almost entirely consists of Quartz (~ 99%). It is a model porous media example and is widely used to find the correlation between petrophysical and multiphase flow properties (Saadi et al. 2017).

In order to characterize the given samples, the porosity, permeability, coordination number, number of pores, pore throat and pore size distributions of each digital twin are computed. The results are shown in Table 2 and Figure 16. The Berea samples, although sharing the same rock type, display distinct properties. Berea 1 is notably tighter compared to Berea 2, as evidenced by its smaller pore throat and pore diameters, as well as its lower permeability. It is important to note that the resolution of the individual samples differs. In contrast, Bentheimer and Fontainebleau exhibit similar properties and were imaged under comparable settings. However, their primary distinction lies in the number of pores present in each sample.

Table 2 Structural and computed petrophysical properties of real digital rock structures

Sample Name	Berea 1	Berea 2	Bentheimer	Fontainebleau
Resolution, [μm]	1.84	3.4	2.56	2.37
Porosity, ϕ, [-]	0.186	0.194	0.149	0.113
Permeability, k, [mD]	777	1904	412	382
Mean coordination number, [-]	3.18	2.94	3.97	3.39
Number of pores, [-]	35917	11935	62239	7225
Mean pore throat diameter	19.8	30.1	22.3	23.8
Mean pore diameter	28.5	46.0	38.2	36.5
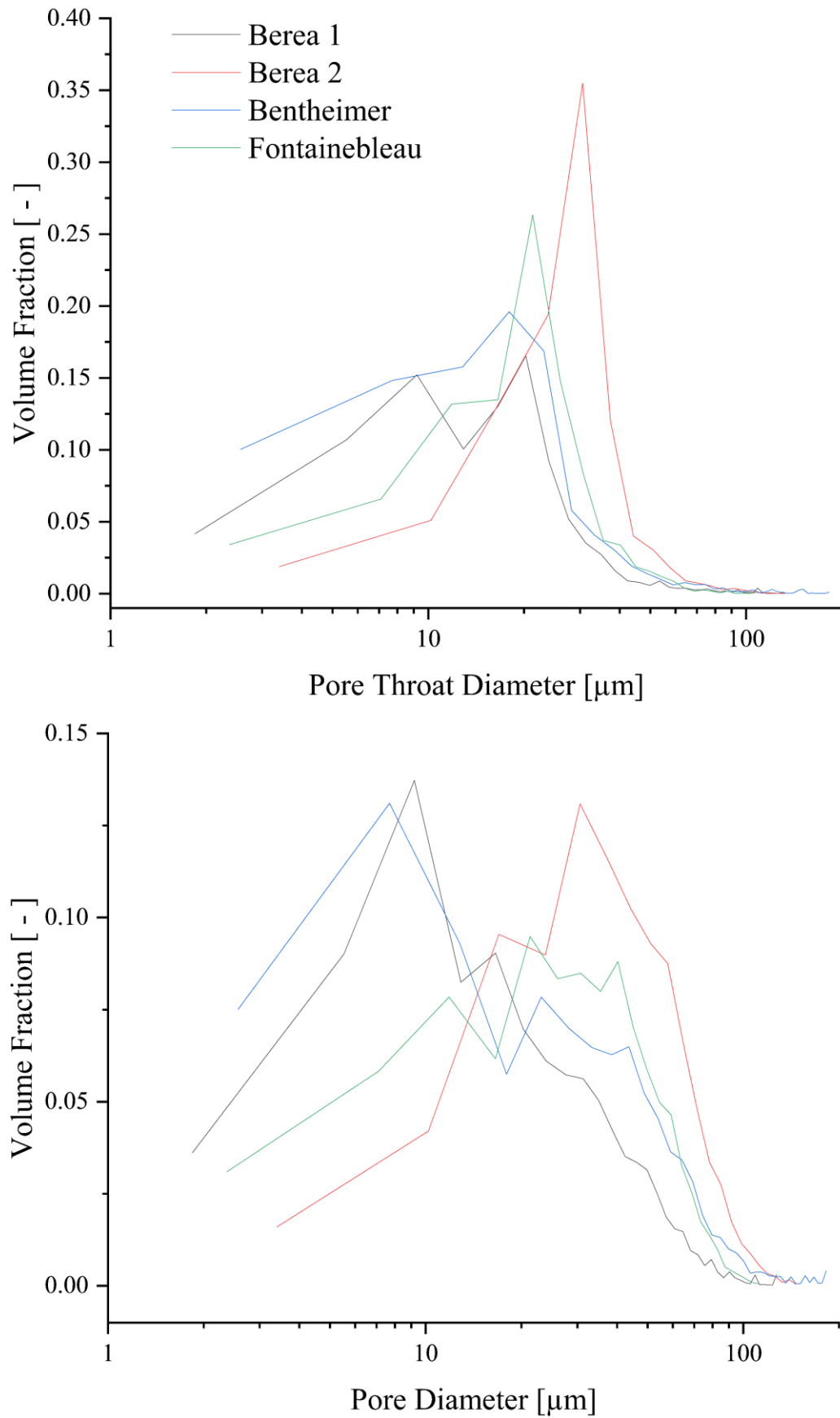
Figure 16 Computed pore throat diameter (top) and pore diameter (bottom) for all four sandstone samples.

In Chapter 5.3 an experimental dataset is used to validate the extension of the MM. Berg et al. carried out a synchrotron experiment on Gildehauser sandstone, which had an average observed porosity of 20% and a permeability of 1.5±0.3 D. Pre-segmented datasets of the domain and the experimental fluid distributions were taken from the digital rocks portal (Berg et al. 2018). As displayed in Figure 17, the digital rock structure has a resolution of (4.4 µm)3/voxel. It comprises a cylindrical domain with dimensions of 830x830x566 voxels, a porosity of 20.3% and a computed permeability of 1.55 D (Arnold et al. 2022; Arnold et al. 2023).
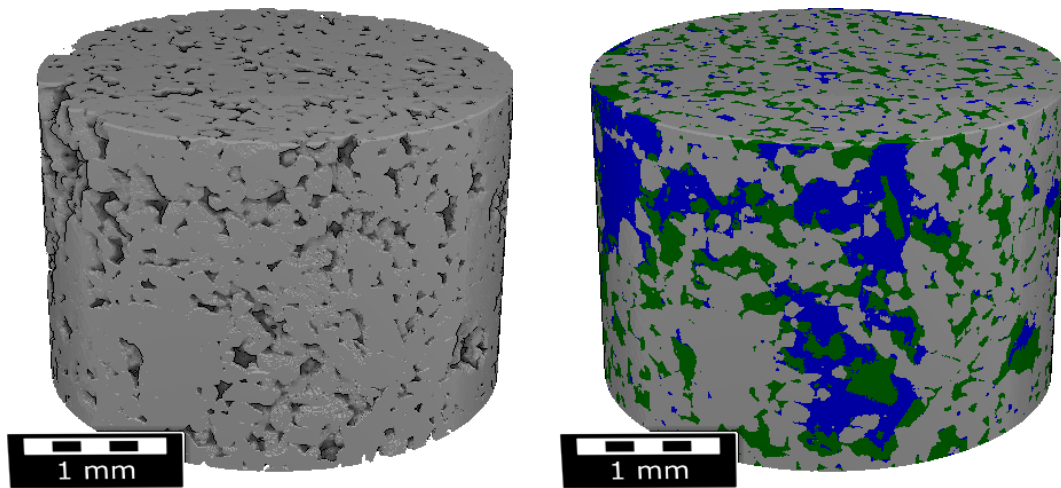
Figure 17 3D digital twin of the Gildehauser structure empty (left) and at residual wetting saturation (right). The right side shows the structure with the fluid distribution as obtained from the synchrotron experiment, with the wetting phase (blue) and non-wetting phase (green).

Chapter 5

Multiphase Modeling and Simulations

In Chapter 3 the drainage and imbibition algorithms used for displacement modeling are introduced. Within this chapter, the wetting variations, parameter sensitivities, and the resulting influence on the relative permeabilities are discussed. Capillary end-effects may influence the connectivity of a phase. In a multiphase core flooding experiment, capillary end-effects arise due to the significant capillary pressure disparity between the end of the core material and the surrounding external region. To minimize these effects changes to the setups are necessary. In order to avoid them during simulations the domain is mirrored by 1/3 of the domain size in flow direction during the drainage and imbibition modeling and is then cropped before the effective permeability simulations.

At the end of the chapter, the method is applied and compared to the experimental data set of Berg et al. (Berg et al. 2018).

5.1   Saturation Functions

Saturation functions are significant input parameters for simulations on a continuum scale and are, therefore, of utmost interest. The two most critical functions for multiphase flow modeling are the capillary pressure and relative permeability, which are closely related. To conduct a sensitivity analysis of these functions, the capillary pressure curves, which form the basis for the computation of relative permeability, are examined first. When computing the capillary pressure curves for imbibition, a distinct jump can be observed at the transition from the spontaneous to the forced part of the capillary pressure curves across the $p_c = 0$ condition. This abrupt p_c change is discussed in Chapter 3.2.3.

5.1.1 Wettability Trends

In chapter 3.3 the different methodologies for implementing wettability in the MM are introduced and thoroughly discussed. Within this chapter, the resulting capillary pressure curves and wettability changes of the systems are presented and discussed. The stochastic algorithm is already applied before the drainage process, therefore influencing the drainage and

imbibition process. Later for the analysis of the different structures, mainly the deterministic approach is chosen, which ensures better comparability for varying contact angles, as the starting point for the imbibition is the same. To analyze the trends each approach is thoroughly analyzed for a single contact angle system for the Berea 1 sample. Additionally, the influence of multiple contact angles on the same sample are investigated.

5.1.1.1 Stochastic and Deterministic Parameter Sensitivity

The stochastic and deterministic approach have different working principles for the implementation of non-wetting material. Therefore, it is expected that both methods will deliver different results. On the other hand, our simulation approach should be robust, which means that the results by varying wettability should rather reflect the uncertainty in wettability determination than another system. However, direct comparison is rather difficult as only the volume of non-wetting material introduced can be compared. Nonetheless, this comparison enables us to explore the spatial influence of wettability, as the deterministic distribution follows the structural topology of the system, including factors such as the pore size distribution. In contrast, the stochastic approach is purely randomized, introducing additional variability. Within this section, the sensitivity of the capillary pressure results to the individual parameters is investigated.

First, the wettability of the system with regard to the introduced volume of non-wetting material is investigated. All simulations are executed by choosing intermediate wetting conditions for both the wetting and non-wetting material, with 40° and 140° respectively. In the stochastic approach, the process is controlled by (a) the solid volume percentage (SVP) and (b) the region size (RS). The higher the SVP the earlier the SI process is stopped since the invasion front accessibility to pores is restricted on a larger scale. A decreasing RS has a similar effect, as the volume of non-wetting material is more thoroughly distributed within the system, influencing a much higher number of pores. For the deterministic approach, the pore space considered (PSC) is the defining threshold, as it defines the volume and spatial distribution of non-wetting material within the system. The higher the PSC the earlier the spontaneous imbibition is stopped, as more material is added, while affecting a wider range of pores.
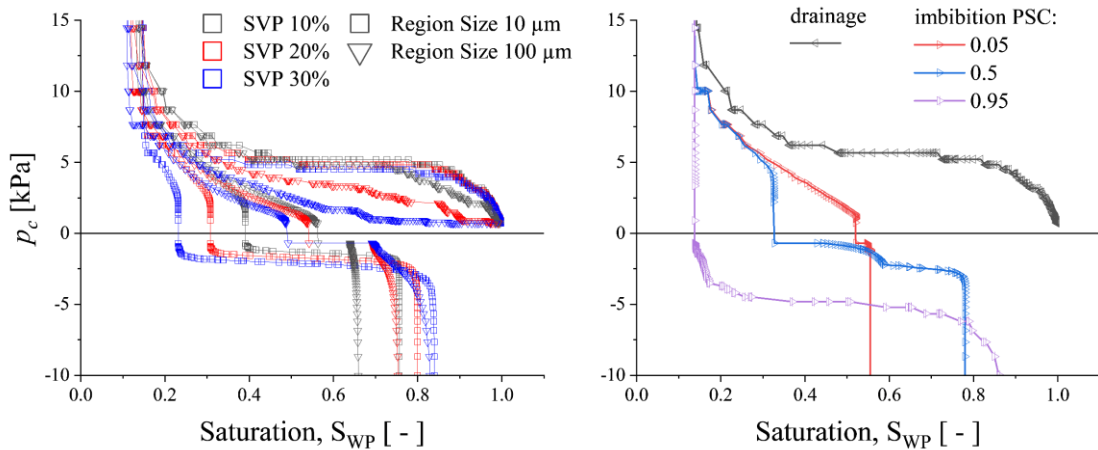
Figure 18 Influence of the non-wetting material input parameters on the capillary pressure curves for the stochastic (left) and deterministic approach (right).

Figure 18 shows the resulting capillary pressure curves of both algorithms. The left side shows six different scenarios, for three different SVP (10%, 20% and 30%) and two different RS (10µm and 100µm). While the WP residual saturation at the end of the drainage is rather unaffected the residual NWP saturations show much larger differences, depending on both the SVP and RS. On the right side of the image, three different PSC (0.05, 0.5 and 0.95) scenarios are shown, which display a large impact on the residual NWP saturation. Ultimately both approaches show the earlier discussed trends.

To further investigate the influence, a more detailed investigation and analysis of the capillary pressure curves is necessary. So far, the wetting state changes have been described by qualitatively discussing the changes in residual saturations and $p_c = 0$ crossing points. In the next step, wettability indices are introduced, which help to quantify the changes. A direct link between wetting and non-wetting state is given by comparing the areas underneath the curve. It indicates the work performed by the system on the environment (which is spontaneous and positive) and the work done by the environment on the system (which is forced and negative). The ratio of these two forms a wettability index (WI). By calculating the logarithm of this ratio, akin to the U.S. Bureau of Mines (USBM) wettability index, a wetting state is indicated by a positive value and vice versa (Donaldson et al. 1969). The Amott (water) wetting index delivers another indication, ranging from 0 to 1, which compares the saturation range of the spontaneously to the total imbibed wetting phase. A value of 0 indicates no spontaneous imbibition, whereas a value of 1 indicates an entirely spontaneous process.
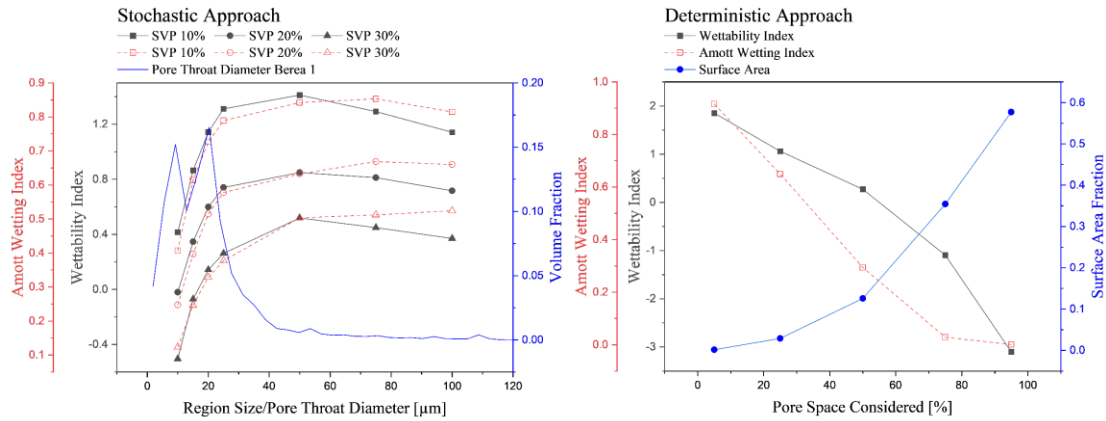
Figure 19 Left: The Amott wetting index and the wettability index from the stochastic approach, with the data plotted as a function of the region size for different solid volume percentages.

For a better comparison, in Figure 19, both indices are plotted as a function of the region size for different SVP (left) and pore space considered (right). In addition to the PSC the surface area fraction of non-wetting material has been computed (right), to show that there is no linear relationship between both. For the stochastic approach (left) both indices deliver similar trends and show that for a fixed SVP the RS majorly influences the wettability of the system. The influence decreases when the RS is larger than the average pore throat diameter, here the effect caused by the SVP dominates. With minor deviations for large region sizes, it can be stated that a smaller RS and higher SVP tend towards a non-wetting state of the system. Large region sizes and SVP might lead to entirely interconnected areas of non-wetting material throughout the system and should therefore be chosen according to the domain size. For the deterministic approach (right) both wetting indices show slightly different trends, with the Amott wetting index indicating more of a non-wetting trend as a function of the pore space considered.

The implementation of non-wetting material in the deterministic approach is based on the pore size distribution of the system. It can therefore be assumed that the wetting condition of the system is governed by the pore structure, i.e., pore size and pore throat size distribution, and by the volume of non-wetting material introduced. While the wetting trends in Figure 19 already indicate that statement, it is more visual in Figure 20. Here, the indices results are plotted against the residual non-wetting phase (NWP) saturation for both approaches.
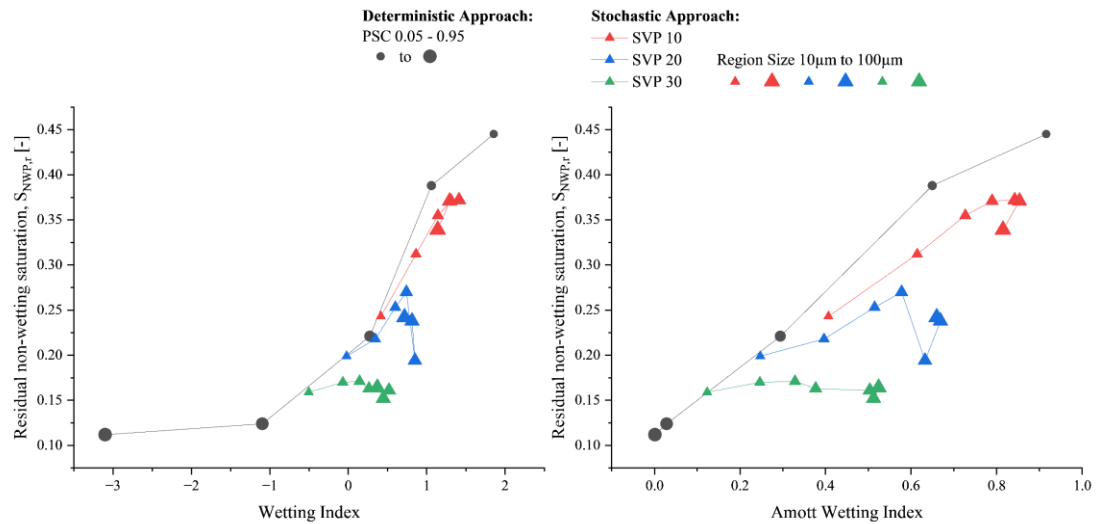
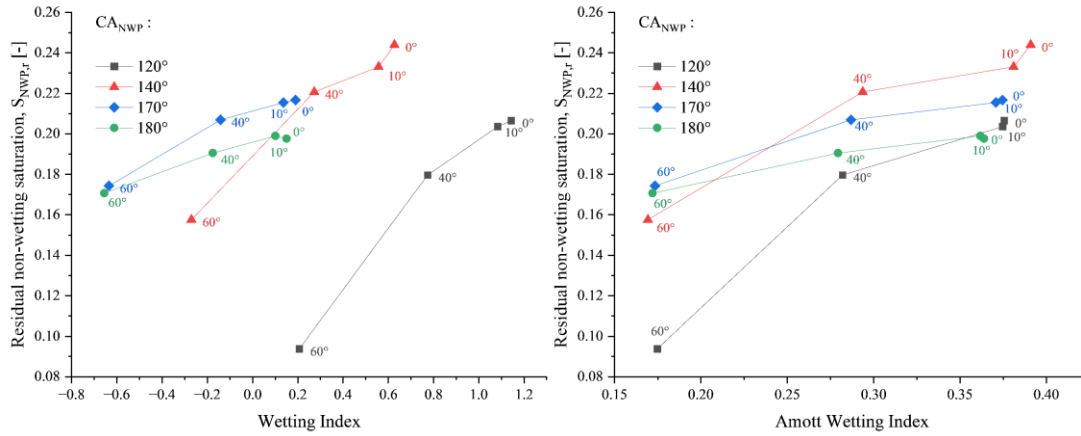*Figure 20 Residual non-wetting phase saturation plotted against the Wetting Index (left) and Amott Wetting Index (right) for the deterministic and stochastic approach. The data is separated by the different input parameters for the non-wetting material. For the deterministic approach, the size of the symbols increases with an increasing PSC value, whereas for the stochastic approach, the sizes scale with the region size.*

The deterministic approach exhibits clear trends for both wetting indices, that with increasing PSC value the wetting conditions change quite drastically with respect to the residual NWP saturation. It implies that the more of the bigger pores are considered and the more of non-wetting material is introduced the more of the non-wetting phase can be displaced during the imbibition process. The stochastic approach on the other hand does not exhibit clear trends for all input parameters. It can be observed that for small region sizes, e.g., 10 μm, the wetting indices have a similar relationship to the residual NWP saturation, as for the deterministic approach. For small volumes, e.g., SVP 10% and 20%, trends can be observed in combination with small region sizes up to 25 μm. This suggests that if the volume and the region size of the implemented non-wetting material are below the structural feature sizes, the structure itself is still dominant with respect to the wetting trends of our system. Once this threshold is overcome the stochastic component of the introduction dominates of the structure itself, which can be seen by the green triangles in Figure 20. Here the relationship of the wetting index to the residual saturation scales with the region size of the introduced non-wetting material.

5.1.1.2 Wetting and Non-wetting Contact Angle Sensitivity

The wettability of a system is not only defined by the size and volume of non-wetting material implemented but also by the individual contact angle of each material. In this chapter, the influence of the contact angle(s) on the wetting state of our system is investigated.
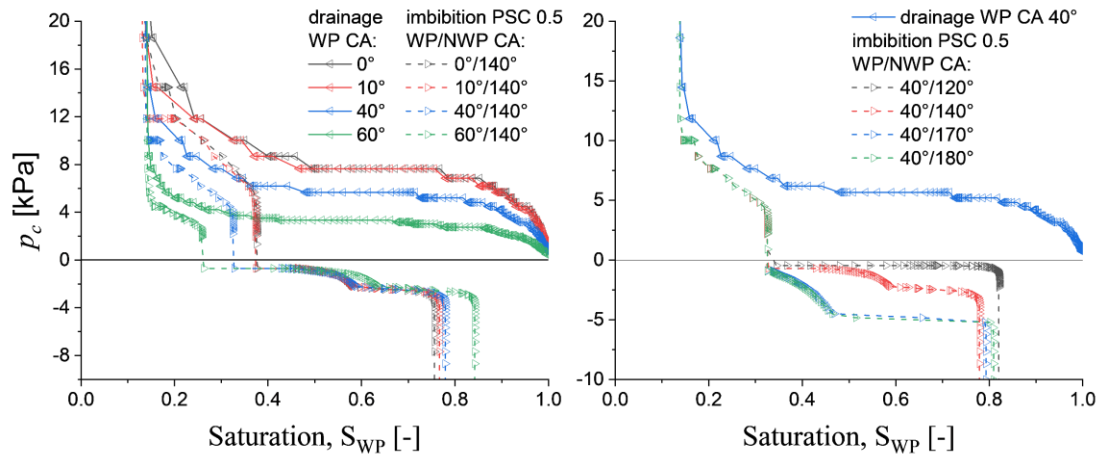
Figure 21 Capillary pressure curve sensitivity to the wetting (left) and non-wetting (right) contact angle, for the deterministic modeling approach, with a pore space considered of 0.5.

For comparability reasons, the deterministic approach was chosen, to ensure the drainage process is solely influenced by the selected contact angle and not by the implementation of non-wetting material. The PSC value is set to 0.5, so both spontaneous and forced imbibition are modeled. The wetting contact is then varied while keeping the non-wetting contact angle constant and vice versa. Figure 21 shows the trends with respect to the different contact angles. A change of the wetting contact angle also influences the drainage process, as seen on the left side, however, it only minorly influences the residual WP saturation as this is mainly defined by the microscopic structure, i.e., pore throat size distribution. An increasing wetting CA indicates a reduced wetting condition, which can be observed by a reduction of the spontaneous imbibition saturation range, which minorly influences the residual NWP saturation. The non-wetting CA on the other side only minorly influences the forced imbibition saturation range showing an increased range with increasing non-wetting CA. In both cases, 60° and 120° seem to differ from the qualitative trend for the forced part of the imbibition curve. The multi-contact angle method after Schulz fails for contact angles close to 90°, which could explain the atypical behavior of both curves. In Appendix A the capillary pressure curves for combinations of all wetting and non-wetting contact angles are shown.

While qualitative changes can be observed in the capillary pressure graphs, the wetting indices offer a quantitative measure of the changes resulting from the variations in contact angles.
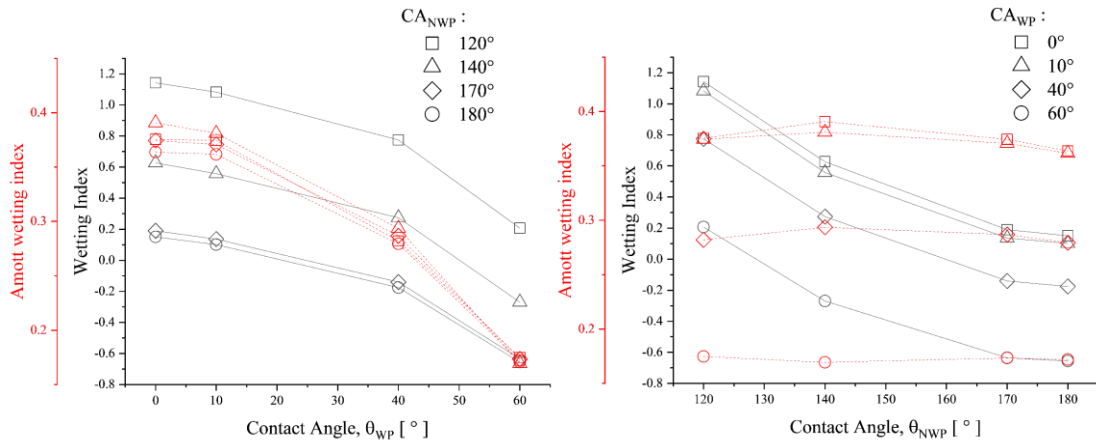
Figure 22 Amott wetting index and wetting index plotted against the wetting (left) and non-wetting contact angle (right)

Figure 22 shows the wetting indices plotted against the wetting (left) and non-wetting contact angle (right), while the respective other CA is varied. The WI (black) exhibits for all cases the same trend when a single wetting or non-wetting contact angle is fixed. The wetting state exhibits a strong correlation with the contact angle, indicating that higher contact angles correspond to a diminished wetting trend. This relationship arises from the scaling of the dilation radius by the cosine of the contact angle, affirming that the modeling approach aligns with the underlying physics. Since the area underneath the capillary pressure curve is directly linked to the scaling of the dilation radius, a higher CA results in a smaller area underneath the SI while the area underneath the FI is increased for higher non-wetting contact angles. While the WI reflects the expected changes from varying the contact angles, the Amott wetting index only shows a trend with respect to the wetting contact angle. On the left-hand side, where the wetting index is plotted against the wetting CA, it can be seen that there are only minor changes between the symbols, but that the index is decreasing with increasing wetting CA. The Amott wetting index correlates to the saturation ranges of the spontaneous and forced process and reflects the modeling approach of each, as it is majorly affected by the wetting CA and nearly unaffected by the non-wetting CA. The invasion during the SI process is entirely governed by the wetting CA, ignoring the non-wetting CA, as only the spatial distribution of non-wetting material affects the process. This results in a strong correlation of the saturation range with the wetting CA, while being unaffected by the non-wetting CA. The later influences the forced imbibition process which equally to the drainage process is only minorly affected by a change of CA. The resulting trends are therefore a direct reflection of the modeling approaches of each process.

Saturation endpoints are essential parameters that define the extreme points in storage or production processes. Changes in these endpoints, for the same rock type, provide an indication of wettability variations. Based on SCAL knowledge, it is anticipated that shifts towards a non-

wetting state, characterized by larger wetting and non-wetting contact angles, will result in reduced trapping of the non-wetting phase and, consequently, smaller residual non-wetting saturations.

Figure 23 Residual non-wetting phase saturation plotted against the Wetting Index (left) and Amott Wetting Index (right) for different wetting and non-wetting contact angle when using the deterministic approach (PSC 0.5).
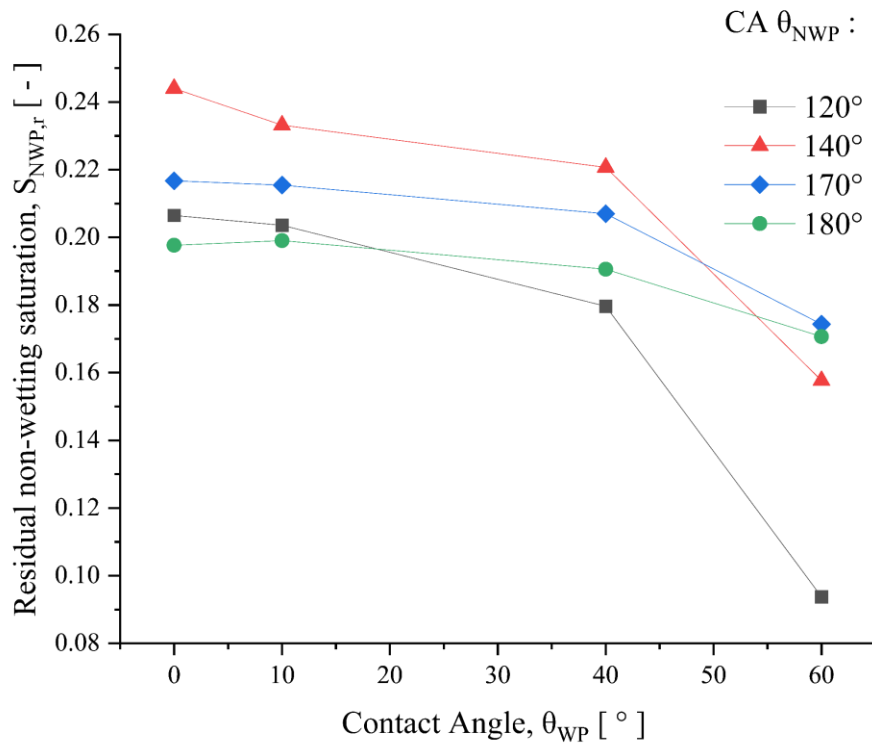
Figure 24 Residual non-wetting saturation as a function of the wetting contact angle for different non-wetting contact angles.

Figure 23 shows the residual non-wetting saturation plotted against the wetting indices, for different wetting and non-wetting contact angle combinations. It can be observed, that the

residual saturation is mainly influenced by the wetting CA, while the wetting conditions change with both CAs. The overall changes in residual non-wetting saturation align with the observations from experiments regarding the variations in wettability.

When strong wetting conditions, e.g., 0° or 180° are applied the changes in the wetting index are most apparent. However, while the work, as reflected by the wetting index, changes with both contact angles, the Amott wetting index is nearly unaffected by the non-wetting CA. This means that the change of the residual saturation caused by the wetting CA is nearly equivalent to the general saturation changes. In Figure 24 the consistency of the residual saturations with respect to the CA is clearly visible. However, it is important to note that CAs of 60° and 120° deviate from the general trend and exhibit more extreme behavior. These irregularities appear to be attributed to the scaling of the dilation radius as discussed in Chapter 3.3.

In systems with strong wetting characteristics, such as gas-water systems, the absence of non-wetting material might make the implementation of non-wetting material appear counterintuitive. However, it's essential to recognize that in those cases the non-wetting contact angle should be interpreted as the receding contact angle of the non-wetting phase when the displacement transitions from a spontaneous to a forced process. This interpretation permits the modeling of a viscous-dominated process through a capillary-dominated modeling approach, where the contact angle reflects the viscous force.

5.1.1.3 Introducing Multiple Contact Angles

Introducing multiple contact angles for the wetting and/or non-wetting materials combines both approaches, as the contact angles are upfront stochastically distributed for the drainage process while choosing the deterministic approach for the imbibition modeling. The distribution of the contact angles on the Berea 1 structure for two different region sizes (10 μm and 100 μm) is shown on the bottom of Figure 12. Instead of a single wetting contact angle, there are now four different contact angles being considered. The material is equally distributed accounting for one-quarter of the solid volume percentage, which also corresponds to the surface area percentage of each material with the pore space. An average contact angle of the system can be calculated by taking the arccosine of the sum of the cosine of each CA multiplied by the surface area fraction of the material wit that CA,

$$\theta_{Avg} = \arccos\left(\sum_{i=1} \cos x_i * \omega_i\right) \qquad [\,10\,]$$

where θ_{Avg} is the average contact angle, x_i the contact angle and ω_i is the surface area fraction of a material. The applied wetting contact angles are $\alpha =$ 10°, 30°, 40° and 60°, with the non-wetting contact angles being the respective opposite (i.e., 180°$-\alpha$). Taking these four CA

results in, an average wetting contact angle of roughly 38.8° and 141.5° for the non-wetting material. Figure 25 shows the capillary pressure curves (left) with respect to the four wetting contact angles and two different region sizes. Since both modeling approaches are combined, the drainage curve is influenced as well, however showing just minor changes. For the one non-wetting CA, 140° was chosen, to compare it with the average contact angle of the four contact angles. The base case, shown by the wine-colored crosses, represents the 40°/140° combination. It fits right into the other data, which backs up the average contact angle calculations. In Appendix B, the wetting indices are plotted against the region size. The total wetting differences between one and four contact angles are only minor, while generally, the smaller region size shows less wetting behavior.
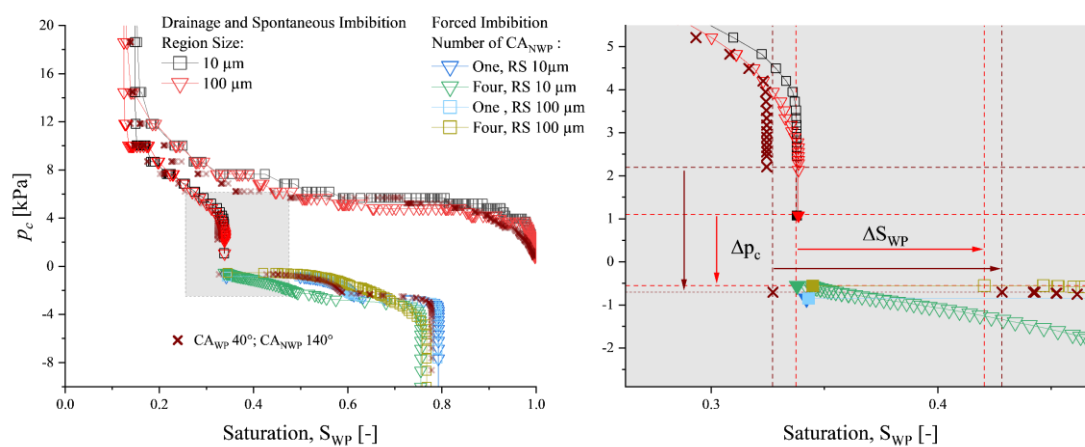
Figure 25 Capillary pressure curves (left) of drainage and imbibition displacement processes for up to four wetting and non-wetting contact angles and two different region sizes (10µm and 100µm). The wine-colored crosses represent the base case with a single wetting and non-wetting contact angle.

The right side of Figure 25 shows the transition zone between the spontaneous and forced imbibition in more detail. The red dashed lines show the capillary pressure jump when switching from the SI to FI modeling, as well as the saturation jump occurring from the first morphological operation. This saturation jump corresponds to pore space which can immediately be filled due to the switch of the wetting conditions. The introduction of multiple CA (a) mitigates the capillary pressure jump occurring at the switch of the processes and (b) the saturation jump coming from the instant filling of pores. In the case of a small region size and multiple contact angles (green downward triangle), an even smoother displacement is observable. An introduction of multiple materials indicates a smoother transition between the processes, even though the overall wettability is similar to the single contact angle cases. Therefore, a strong influence on the connectivity of the phases is expected.

The wetting state of the systems mainly depends on the introduction of non-wetting material, with the volume and region size having the biggest overall influence. In combination with the

wetting CA, it defines the spontaneous imbibition modeling, which sets a major part of the wetting state. More precisely they define the residual saturations, therefore influencing both wetting indices. The qualitative non-wetting CA influences on the hand are rather small, as they mainly concern the area underneath the curve rather than the residuals. Further investigations into the phase distributions and connectivity are therefore necessary, also with regard to the introduction of multiple contact angles.

5.1.2 Relative Permeabilities

The relative permeabilities for a saturation state are calculated by solving the Stokes flow equation for each phase and dividing it by the absolute permeability of the system simulated in a single-phase state. Hence, the phase population of the model is essential and parameters influencing the displacement modeling will affect the individual fluid-phase mobilities as well. A flow can only be calculated when the phase is connected from the inlet to the outlet. A relative permeability value of zero indicates that the phase is no longer or not yet connected throughout the system, however, displacement processes can still be applied which can result in different saturation ranges for the mobile wetting and non-wetting phases. The relative permeabilities are computed for different imbibition curves to analyze the influence of the input parameters, i.e., wetting state, on the fluid distribution and connectivity.

5.1.2.1 Stochastic and Deterministic Relative Permeabilities

The highest influence on the imbibition capillary pressure curves has proven to be the wetting CA, the region size and the volume of non-wetting material introduced. Figure 19 (left) showed that for the stochastic approach. The largest change was given for region sizes starting at 10 μm and increasing to 50 μm. To assess the sensitivity of the resulting relative permeabilities, simulations were conducted for three different combinations of SVP (10%, 20%, and 30%) and RS (10 μm, 25 μm, and 50 μm), while keeping the wetting and non-wetting CA fixed at 40° and 140°, respectively. Figure 26 shows the resulting relative permeabilities plotted against the WP saturation. Even though the stochastic approach is influencing both drainage and imbibition, generally the connectivity at the end of the primary drainage is similar. A general observation is that the effective permeability of the NWP at residual WP saturation is higher for large SVP and RS values. This observation is expected, since large volumes of non-wetting material result in a higher connectivity of the NWP throughout the domain. The top panel shows the influence of the SVP for a fixed region size of 25 μm.
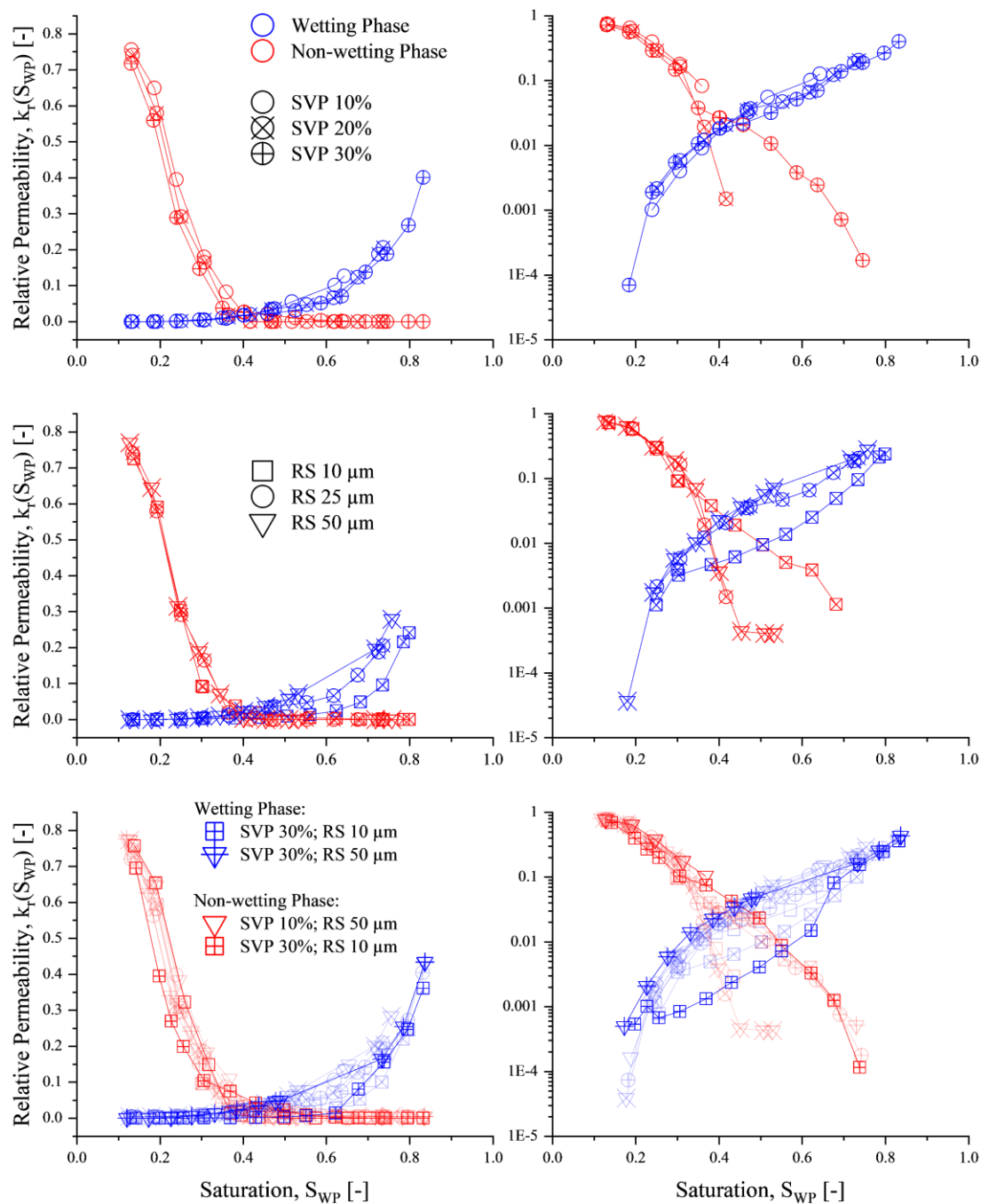
Figure 26 Relative permeability curves plotted against the wetting phase saturation on a linear (left) and logarithmic (right) scale. The top panel shows the influence of the SVP (10%, 20% and 30%) of non-wetting material in combination with a RS of 25 μm. The middle panel shows the influence of the RS (10 μm, 25 μm and 100μm) in combination with a SVP of 20%. The bottom panel shows the cloud of relative permeabilities from all nine combinations.

On the logarithmic scale (right) it can be observed that the SVP majorly influences both the wetting and non-wetting phase relative permeabilities. While the WP trend in all three cases is similar, the starting point of connectivity of the WP and residual endpoints differ majorly

($\Delta S_{NWP,r} = 0.3$ and $\Delta k_{r,WPe} = 0.37$). A large SVP results in an early connectivity of the WP and a large saturation range for the simulation. The latter is mainly a consequence of the ratio between SI and FI, as a large SVP results in an earlier stoppage of the SI modeling, hence a larger FI saturation range and lower residual NWP saturation. This observation is reflected in the NWP relative permeabilities as well, where an early cut-off can be observed for a small SVP while a thorough connectivity is given for a large SVP.

During the SI modeled saturation range the NWP connectivity reduces strongly, which can result in a relatively large "jump" of the relative permeability values. This is observable around 0.3 WP saturation points for the SVP 20% and SVP 30% cases. However, all three cases still exhibit the same trend at the start of the imbibition process. The middle panel of Figure 26 shows the influence of the RS for a fixed SVP of 20%. Similar to the effects the SVP has, the RS also influences the point of connectivity but also influences the trend of the WP relative permeabilities to a larger extend. A small RS value shows less connectivity for the WP compared to a larger RS. The connectivity starts to deviate at the point where the FI modeling starts. This is a consequence of the general modeling approach, where the roles of the WP and NWP are switched. The switch allows for the unresisting invasion of former wetting regions, while the more initial non-wetting material is introduced, the higher the barrier. Additionally, small region sizes avoid the instant filling of larger regions, as they are more thoroughly spread through the system. In the bottom panel, all combinations are shown in a cloud of relative permeabilities. The cases setting the boundaries are marked, while the rest is made transparent.
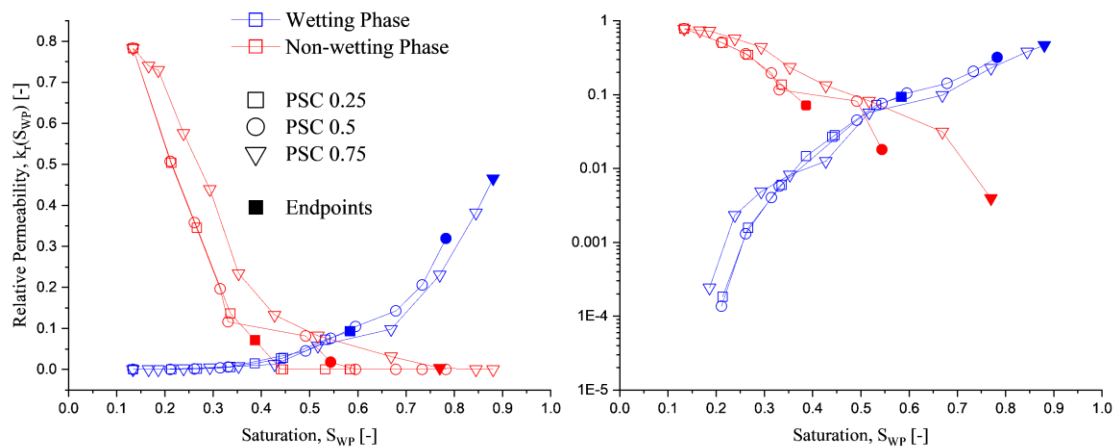
Figure 27 Relative permeability curves plotted against the wetting phase saturation on a linear (left) and logarithmic (right) scale. The curves show the influence of the pore space considered (PSC), which is mainly observable for the simulation endpoints, which indicate either the disconnection of the NWP or the residual wetting saturation.

The right side of Figure 19 has shown that for the deterministic approach the PSC highly influences the wetting conditions of our system, with an increasing value making our system

less wetting. Therefore, an influence on the relative permeabilities is also expected. In Figure 27 the relative permeabilities are plotted on a linear (left) and logarithmic (right) scale, for varying PSC values. The values of 0.25, 0.50 and 0.75 were chosen, so the imbibition consists of a spontaneous and a forced part. The indicated endpoints represent the last point of connectivity for the NWP and the residual WP saturation for the WP. A general trend for the WP relative permeabilities can be observed that mainly differs for the endpoints, which is a consequence of the SI and FI imbibition modeling. A low PSC value indicates a larger SI to FI ratio that results in an earlier cut-off of the NWP connectivity and a reduction of the total imbibition saturation range. This can be observed by the NWP relative permeability endpoints. However, it should also be noted that the nonwetting mobility is higher for a larger PSC value where the imbibition modeling is almost entirely forced.
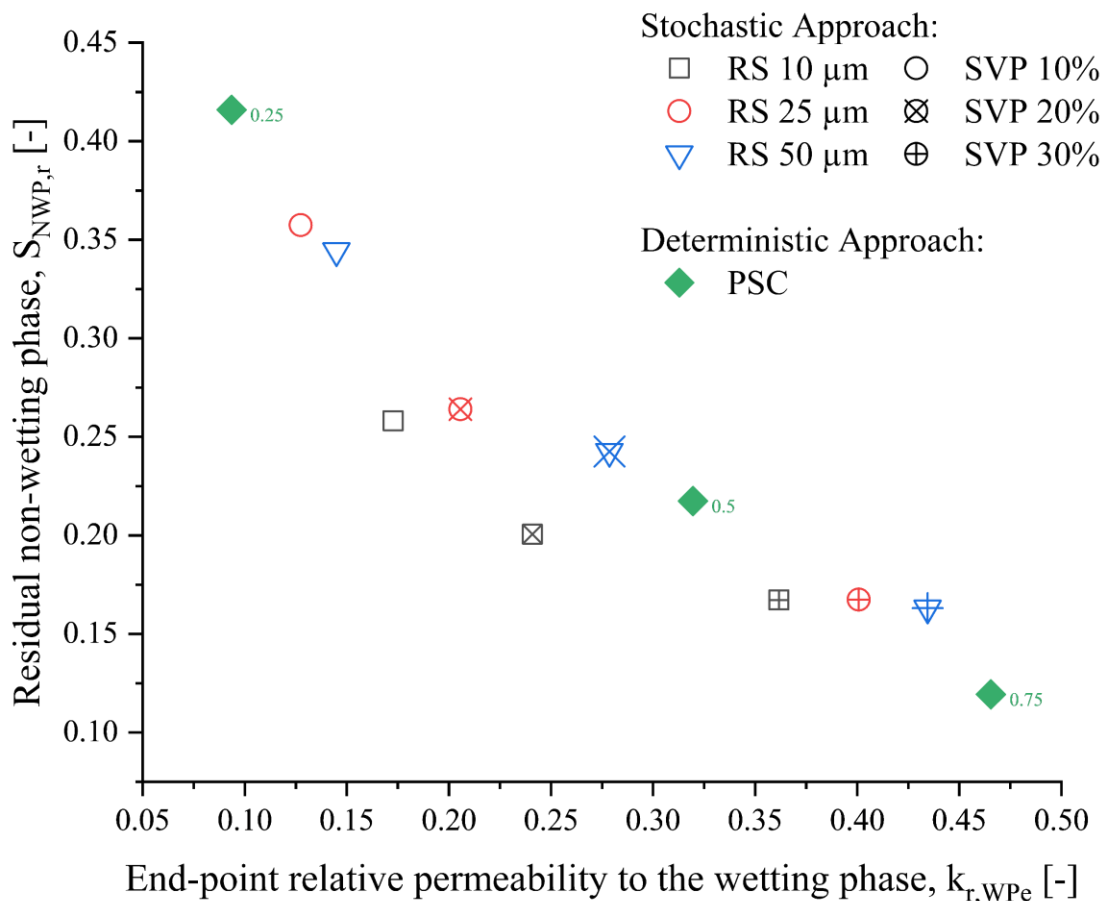
Figure 28 Residual saturation of the non-wetting phase plotted against the end point relative permeability of the wetting phase for varying parameters of the non-wetting material introduced by the stochastic and deterministic approach. The labels indicate the PSC value.

Both modeling approaches are significantly affected by the region size and volume of non-wetting material introduced. Especially the connectivity of the NWP is directly linked to the imbibition modeling, which is highly influenced by both parameters, as shown in chapter 5.1.1.

The results reflect the ratio between SI and FI. The relative permeabilities trends of each phase are similar, even with varying parameters, but exhibit different end-points. Figure 28 shows the end-point relative permeabilities of the wetting phase as a function of the residual saturation. Here it can be observed that in both modeling approaches the WP end points scale almost linearly with the residual NWP saturation. This suggests that significant changes are effectively imposed on the system through the introduction of the non-wetting material. The impact is most pronounced when either large regions (high RS) or a substantial portion of the porous medium (indicated by a high PSC value) are affected.
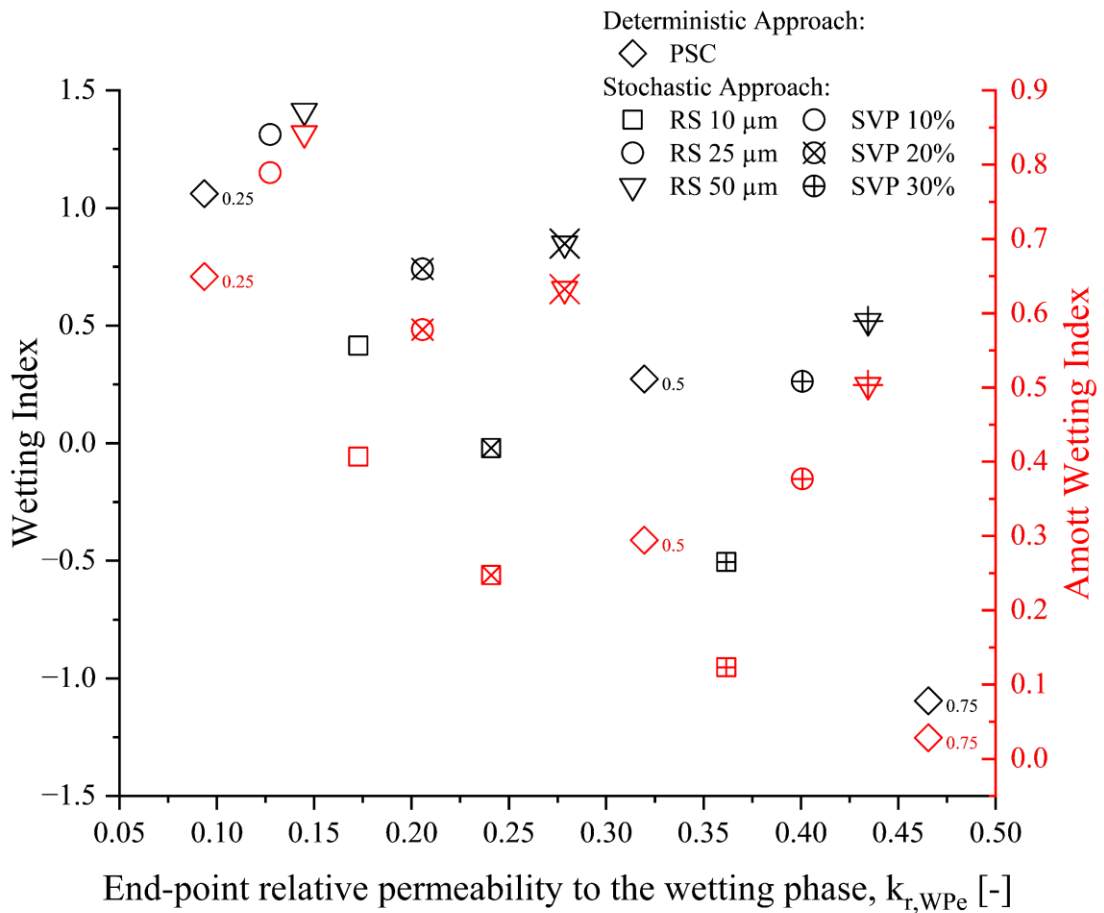
Figure 29 Wetting index and Amott wetting index plotted against the end point relative permeability of the wetting phase for varying parameters of the non-wetting material introduced by the stochastic and deterministic approach. The labels indicate the PSC value.

In Figure 29, the wetting index and Amott wetting index are plotted against the end point relative permeability of the wetting phase. This is done for different parameters of the non-wetting material introduced using both the stochastic and deterministic approaches. In the stochastic approach, both the wetting index and Amott wetting index exhibit nearly identical variations in relation to the end-point relative permeability. This suggests that both indices serve as robust measures of wettability change in the system for this approach.

On the other hand, the deterministic approach reveals that the quantification by the indices is similar when either SI or FI dominates (PSC value of 0.25 or 0.75, respectively), but diverges in cases of mixed wetting conditions. This outcome is expected because the volumetric introduction of non-wetting material scales linearly in the stochastic approach but not in the deterministic approach. The heterogeneity introduced by considering more pores with non-wetting surfaces can have a greater impact on the wetting state than solely relying on changes in the surface fraction. Consequently, the wetting indices scale similarly when the surface fraction (SVP value) changes, but differ when the spatial distribution is also taken into account. This discrepancy is observed for a PSC value of 0.5 and in cases where the SVP value is the same but RS varies.

5.1.2.2 Contact Angle Sensitivities of Relative Permeabilities

The wettability is strongly influenced by the assigned CA values as well as spatial distribution, allowing alternative invasion path ways for the same porous structure. From previous observations on the capillary pressure curves, the highest influence is expected from the wetting CA. For the base case simulations, a PSC value of 0.50 is chosen.
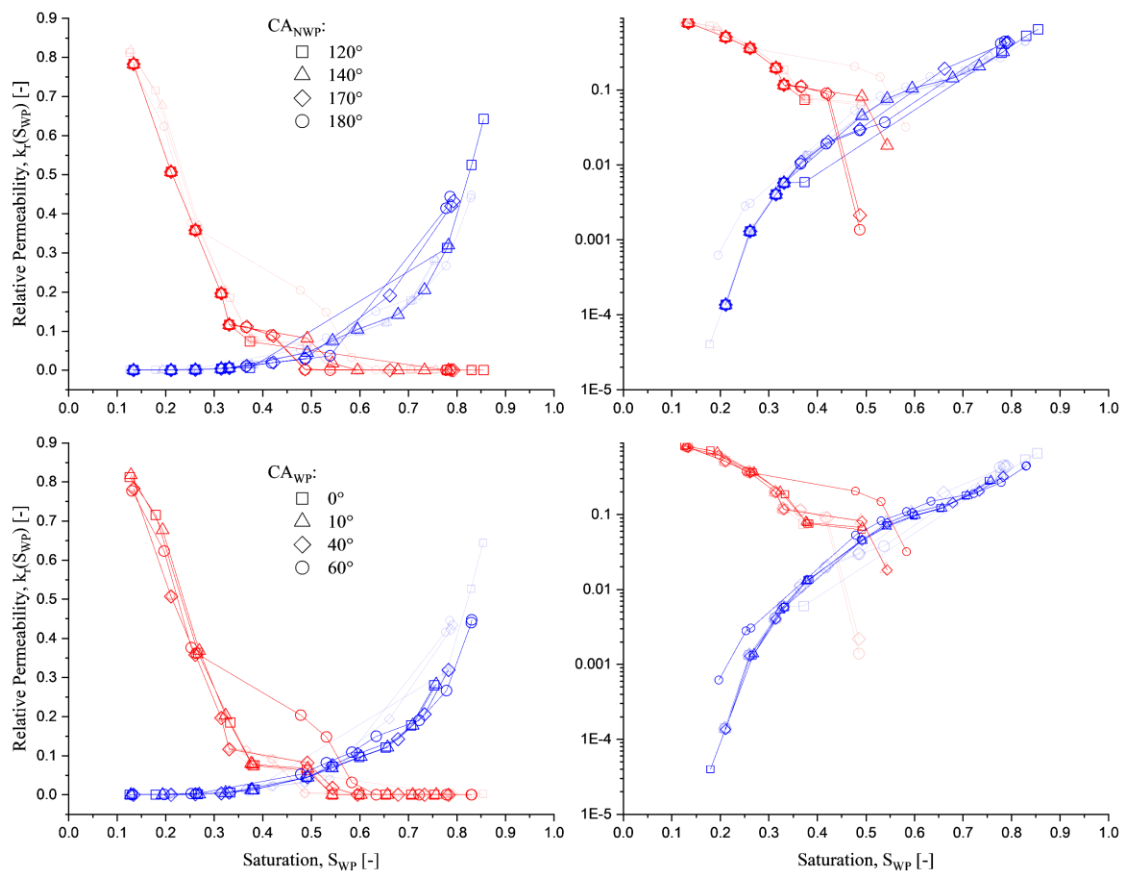
Figure 30 Contact angle dependent relative permeability curves on the linear (left) and logarithmic (right) scale as a function of the wetting phase saturation. The top shows the sensitivity to the non-wetting

contact angle and the bottom the sensitivity to the wetting contact angle. The influence of the respective other wetting material is plotted in all graphs by the transparent symbols.

Figure 30 shows the resulting relative permeability curves as a function of the wetting phase saturation. The top panel shows the influence on the curves with respect to the non-wetting CA. Since the SI part is unaffected by the non-wetting CA, the resulting influence is limited to the FI saturation range, after approximately SWP = 0.3. A higher NWP CA results in a stronger WP connectivity and consequently lower NWP connectivity. The initial NWP RP drop is associated with the spontaneous imbibition modeling. However, it can be observed that both contact angles highly influence the end point relative permeabilities of the wetting phase. For both contact angles it can be observed that weaker wetting conditions i.e., ($\theta = 60°, \theta = 120°$), lead to a higher WP end point relative permeability, implying more neutral wetting conditions.
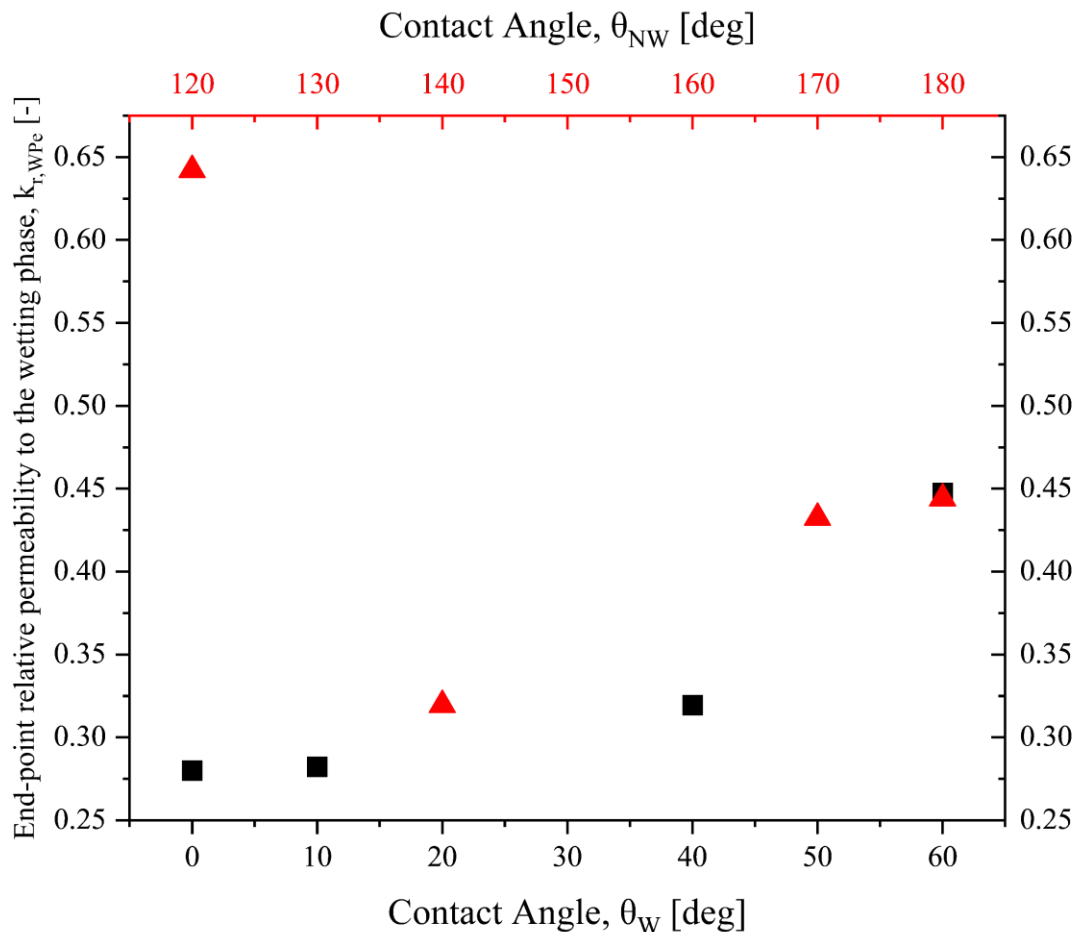
Figure 31 End-point relative permeability of the wetting phase plotted against the assigned contact angle of the wetting and non-wetting material. The wetting contact angles were combined with a non-wetting contact angle of 140° and the non-wetting contact angles with a wetting contact angle of 40°.

The end-point relative permeabilities of the wetting phase are plotted as a function of the wetting and non-wetting contact angles in Figure 31. Excluding the non-wetting CA of 120°, an increase in the end-point relative permeabilities is observed in less wetting conditions (high

θ_W and θ_{NW}), implying a shift in the wetting state of the systems as expected from SCAL experience. When a non-wetting CA of 120° is applied, an overly connected wetting phase is obtained in the simulations, as indicated by $k_{r,WPe} = 0.64$. While the relative permeability curves for that case still follow the same trends as the other contact angles, the end-point strongly deviates. This deviation is most likely a consequence of artifacts created by the scaling of the dilation radius during the displacement modeling.
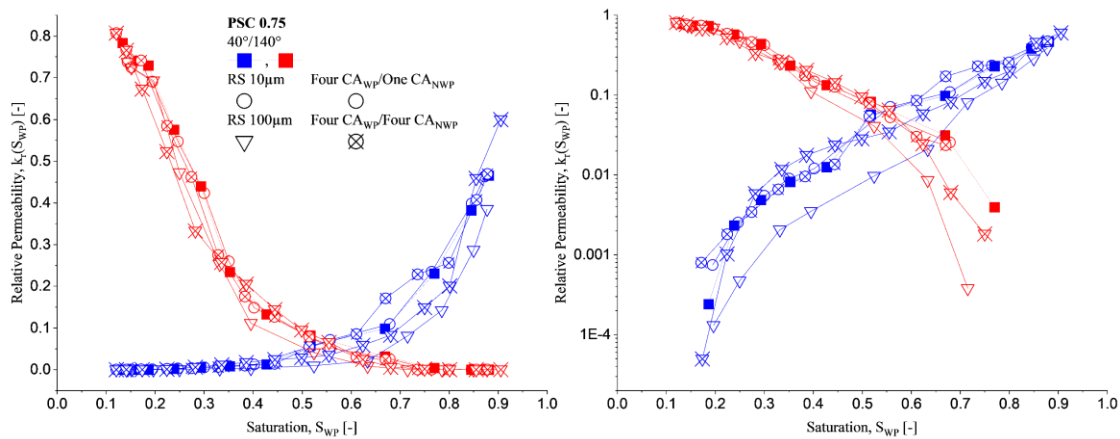
Figure 32 Relative permeabilities for single and multiple contact angles on a linear (left) and logarithmic (right) scale using the deterministic approach with a PSC of 0.75.

The introduction of multiple contact angles has shown, with regard to the capillary pressure curves, that mainly the transition between the SI and FI is smoothed down, as well as the saturation jump at the switch between both processes can be reduced. Figure 32 shows the resulting RP for a single CA for both wetting and non-wetting, four wetting CA and a single non-wetting CA as well as the combination of four contact angles of both wetting conditions. While the differences in the capillary pressure curves are rather minor, especially with regard to the spontaneous imbibition modeling, the relative permeabilities show larger effects. Major differences can be observed for different region sizes (circle and triangle) of the CA material introduced for a forced imbibition-dominated process. Having multiple wetting CA for large regions of each CA, reduces the connectivity during the displacement process, whereas multiple non-wetting CA mainly influence the end point of the WP RP (crossed symbols).

This indicates that the identification and assignment of different contact angles to different materials play a major role for the imbibition displacement, especially the forced.

The complete set of relative permeabilities for all combinations can be found in Appendix C.

5.2   Sensitivity to Different Rock Samples

The structural and petrophysical properties of the used structures introduced in Chapter 4 suggest that each of the systems has different prerequisites. Therefore, different capillary pressure curves are expected for the same wetting conditions, and subsequently different relative permeabilities. In Figure 33 the modeled capillary pressure curves are plotted when using the deterministic approach with a PSC value of 0.50 and a 40°/140° contact angle combination.
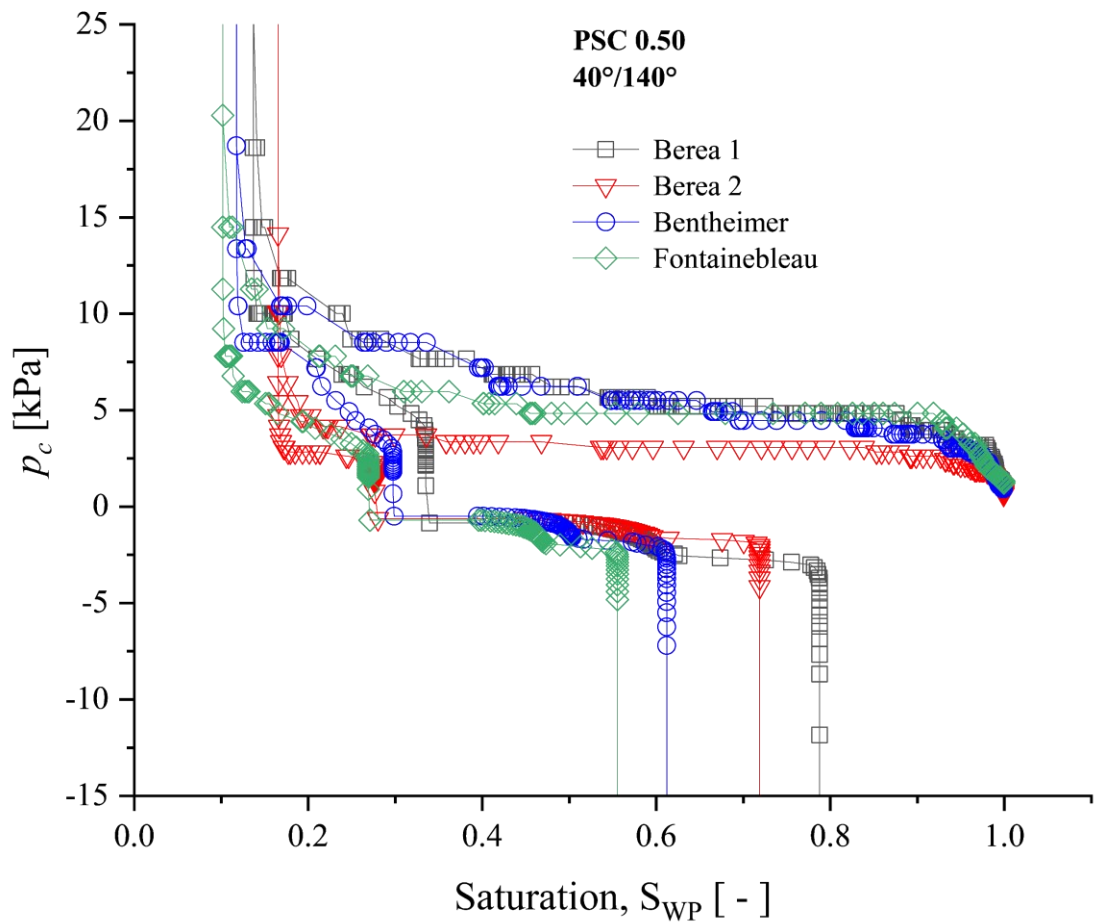
Figure 33 Capillary pressure curves of the four different structures for the deterministic approach with a PSC 0.50 and a contact angle combination of 40°/140°.

This combination showed the highest differences and includes a good ratio between the spontaneous and forced displacement. The residual wetting saturations range from 0.1 to 0.16, whereas the non-wetting residuals range from 0.21 to 0.45. For a high or low PSC value, the saturation range between the structures decreases significantly, suggesting that once a single displacement process is dominant the structure dependent differences mitigate. While the Berea 1, Bentheimer and Fontainebleau have a similar saturation range for the spontaneous

imbibition, the Berea 2 the smallest of all ranges. The Berea 2 does not follow the general tendencies for the residuals, as exhibited by the other three structures.

The relative permeability curves have shown a high sensitivity to the implied wetting conditions, with the volume and spatial distribution of non-wetting material being the most influential. Due to the nature of the WP occupation within the MM, the SI process should be governed by the pore body distribution whereas the FI should follow the pore throat size distribution. Therefore, the investigation focuses on whether the same trends shown in the previous chapter are reflected for different rock structures as well, assuming a constant contact angle combination.
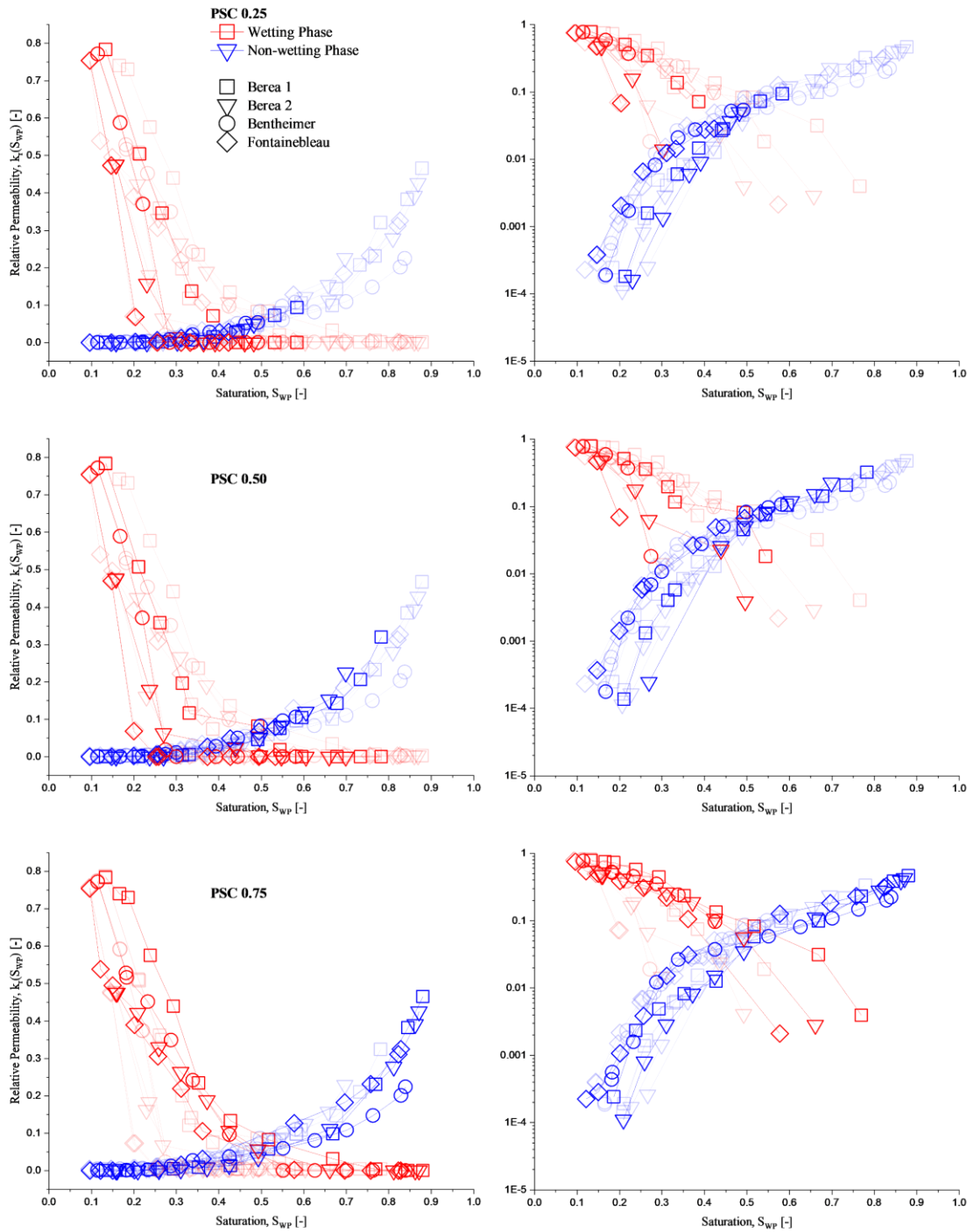
Figure 34 Relative permeability curves for different structures plotted against the wetting phase saturation on a linear (left) and logarithmic (right) scale for varying PSC.

Figure 34 shows the resulting relative permeability curves on a linear (left) and logarithmic scale (right) for varying PSC values of all four structures. Each of the samples has quite different relative permeability values, with especially the endpoints differing from each other. The WP RP converges for larger WP saturations while the NWP RP diverge. The Berea 1, Bentheimer and Fontainebleau showed similar trends for the capillary pressure curves, which continue for the relative permeabilities. It can be observed, that the Fontainebleau is most influenced by the SI modeling, whereas the Berea 1 is least effected. Especially the NWP RP are governed by that which could result from the large portion of small pores as shown in Figure 16. Since the small pores tend to be filled with the WP, a large volume of those could indicate an early disconnection of the NWP, as observed in the top and middle panels of Figure 34. Furthermore, Berea 2 shows the least connectivity of the WP at the end of the primary drainage process, however, shows during the displacement process less of a disconnection in comparison to the Bentheimer and Fontainebleau structures.
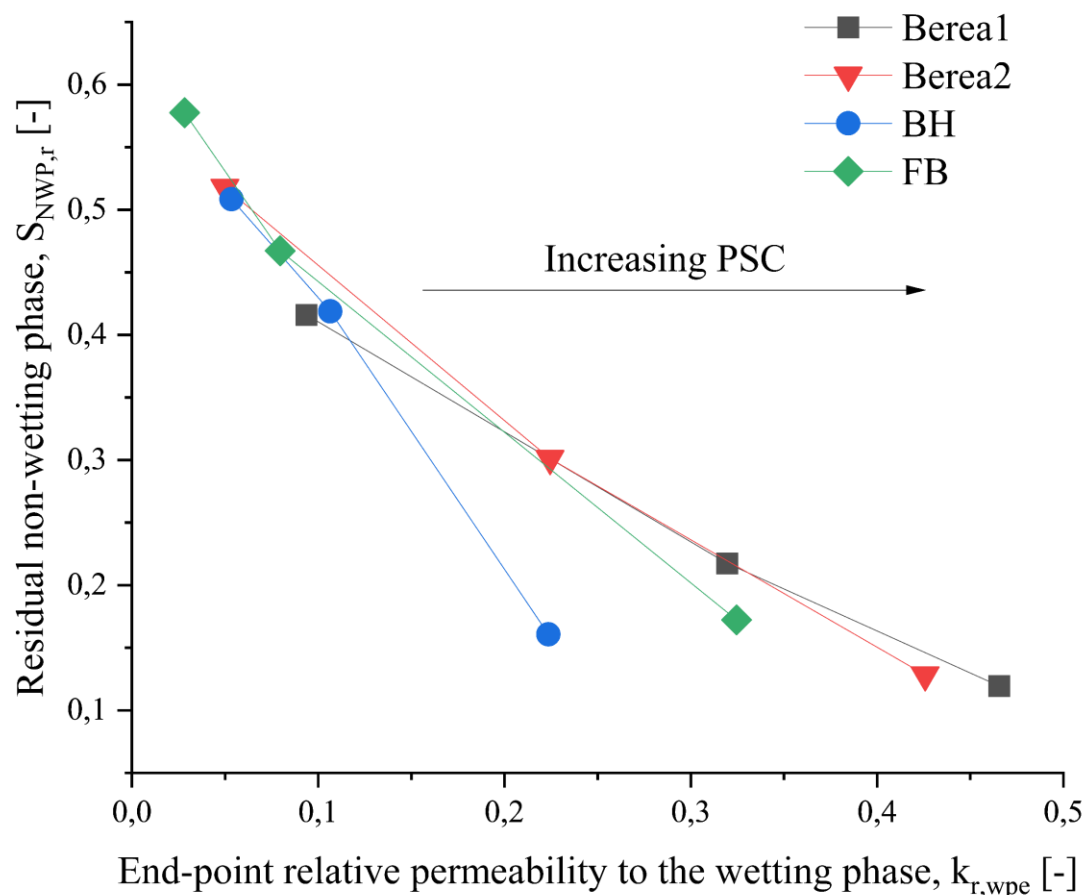
Figure 35 Residual saturation of the non-wetting phase plotted against the end point relative permeability of the wetting phase for different rock structures. The data has been created using the deterministic approach with PSC values of 0.25, 0.50 and 0.75.

All structures show similar trends of increasing WP end-point relative permeability, with decreasing residual NWP saturations for an increase in PSC value, as plotted in Figure 35. However, the gradient of these trends differs among the samples, with Berea 1 and 2 exhibiting similar behavior. This suggests that the changes in relative permeability and saturation end-points are influenced by the structural properties and may be dependent on the rock type.

5.3   Validation with Experimental Relative Permeability Data

In 2016 the research group Berg et al. (Berg et al. 2016b) conducted an imbibition experiment at a synchrotron facility, where they imaged a water/oil system at different steady states. The previous study is therefore perfectly suited as it captured the steady-state fluid configurations during an imbibition process, which can be directly compared to modeled data. However, the study revealed a considerable disparity between the imbibition relative permeability curves simulated based on morphological and experimentally derived fluid distributions. To validate the introduced extension of the imbibition modeling and to further investigate the parameters, as well as determine the uncertainty range, the experimental imbibition process was modeled using the modified approach. The experiment was conducted with a water/decane system, which in our simulations are represented by the WP and NWP respectively. For the modeling predominantly, the deterministic approach is applied to investigate the sensitivity of the relative permeabilities to the different wetting states of the system while tying the implementation of non-wetting material to the structure topology. Both the imbibition process only (starting at experimental fluid configuration) and the entire displacement cycle (drainage and imbibition) are modeled to compare the matching and predictive capabilities of the new approach. The modeling of the drainage followed by the imbibition displacement will be referred to as *full cycle* within this section.

The connate wetting saturation of the experiment is at $S_{wp,c} = 0.21$, which serves with the experimental fluid distribution as starting point for the imbibition simulations, as well as orientation for the full cycle modeling. In the synchrotron experiment a residual non-wetting saturation of $S_{nwp,r} = 0.29$ was reached which is used as a reference point for the parameter matching.
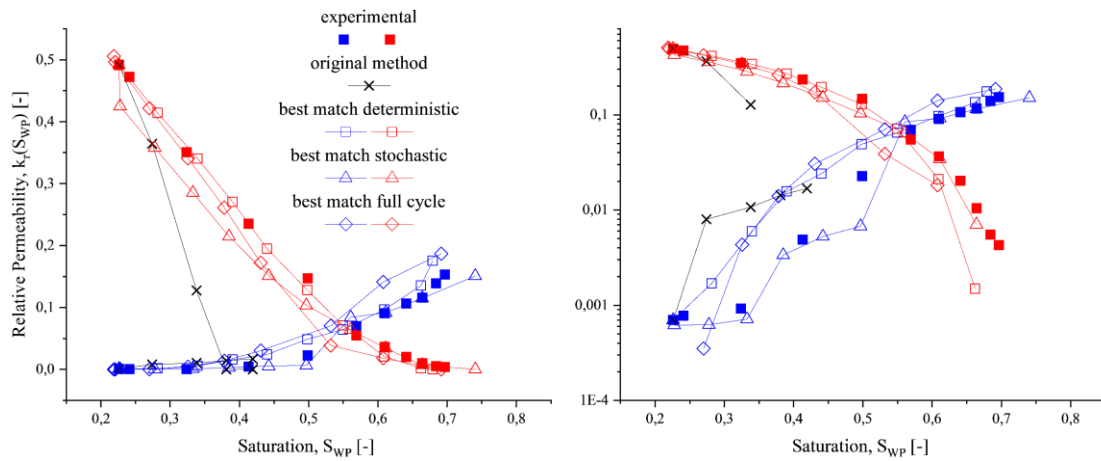
Figure 36 Relative permeabilities on the linear (left) and logarithmic (right) scale. The simulated data on the experimental fluid distributions of the WP (blue) and NWP (red) is represented by the solid squares (■). The other curves represent the best matches for the imbibition modeling only (stochastic and deterministic approach) and full cycle modeling.

The best results were achieved when using a PSC value of 0.75 which resulted in a residual NWP saturation ranging from 0.25 to 0.35 for varying wetting and non-wetting CA. A PSC value of 0.75 corresponds to a volume of roughly 35% of non-wetting material which is introduced. To compare the stochastic approach as well, the structure was populated with 30% and 35% of non-wetting material for a RS of 10 μm, since a forced-dominated modeling delivered the best results. The parameters were chosen based on the previous observations. In Figure 36 the best matches for the relative permeability simulations are plotted. The original method refers to the initial (spontaneous only) modeling approach, which was computed in the initial study by Berg et. al (Berg et al. 2016b) and has been re-simulated for reference. It is obvious that in addition to the extended saturation range also the data matching has greatly improved. There is a slight underestimation, especially for higher saturations, for the NWP, whereas the WP is slightly overestimated. However, overall, the simulated data matches the experimental one quite well. To match the experimental data strong wetting and non-wetting conditions ($\theta = 0°\ or\ \theta = 180°$) need to be avoided. For the deterministic (PSC 0.75) and stochastic approach (RS = 10 μm, SVP = 30%), the best match was found for a 40°/140° combination. Both deliver similar results with respect to the NWP, with the stochastic approach matching the WP as well. The full cycle simulation was performed with the deterministic approach as well but gave the best results for a 60°/140° combination.

When starting from the experimental fluid distribution the best matches were found modeling forced imbibition only. On a first thought, this might seem counterintuitive as the experiment should include both spontaneous and forced, unless the system is strongly non-wetting. During

the experiment a water/decane combination was used, which rather indicates water-wetting conditions implying the presence of a spontaneous imbibition as well. Conversely, in a flow experiment, water may invade at a faster pace than it is spontaneously imbibed, meaning that the imbibition could be forced. When modeling the drainage and imbibition on the digital rock structure, i.e., entirely working with simulated fluid distributions, the best result was found when applying even lesser wetting conditions, which lead to both a great match for the residual saturations as well as relative permeabilities. However, here as well the imbibition was modeled, almost entirely by a forced process, with only two saturation points being the range for the spontaneous part.

The imbibition simulations were initiated using the experimental fluid phase distribution, which had a connate water saturation of $S_{w,c} = 0.21$. The experimental remaining oil saturation ($S_{o,r} = 0.29$) was utilized as a reference endpoint to select the appropriate parameters for the algorithm. The imbibition simulations were performed using 75% of the pore space for conversion, resulting in a residual oil saturation ranging from 0.25 to 0.35 for non-wetting material contact angles of 180° and 140°, respectively. Using the initial implementations, i.e., only spontaneous modeling, a $S_w = 0.41$ was reached at the end of the imbibition process as already shown in the study of Berg et al. (Berg et al. 2016b). In Figure 36, the experimental relative permeability data (solid squares) are compared with the initial morphological modeling approach (crosses). The new algorithm resulted in a reduction of the spontaneous imbibition saturation ranges, ranging from 0.25 to 0.32, depending on the chosen WP contact angle. The range of resulting relative permeability curves is shown in Figure 37, demonstrating a successful extension of the saturation range while reducing the offset to the experimental data. An outlier from the otherwise good matches is given for the deterministic approach using a 40°/120° combination.
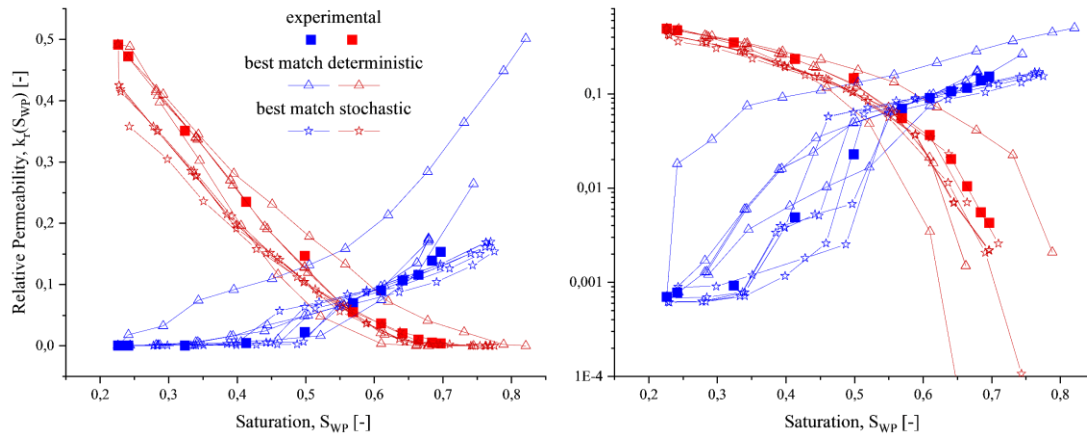
Figure 37 Relative permeabilities on the linear (left) and logarithmic (right) scale. The graphs show a cloud of results for the deterministic (triangle) and stochastic (star) approach for varying contact angles.

The NWP relative permeability is mainly affected by the wetting contact angle, whereas the non-wetting contact angle influences both. The NWP relative permeability decreases as the wetting contact angle decreases, especially during the early stages of imbibition. As the diminished connectivity of the NWP arises from spontaneous imbibition, this effect is more pronounced for strong wetting contact angles around $\theta = 0°$. This results from the trends shown in chapter 5.1.1.2, that the spontaneous and forced saturation range scale with the wetting CA. This is due to the disconnected NWP clusters during the SI process, which cannot be reconnected during any further displacement events.

Although often not commonly discussed, it is indeed possible for water to invade at a higher rate than occurring spontaneously during a flow experiment, resulting in a forced imbibition.

5.4   Summary

The simulation results have shown that the modified modeling approach successfully extended the imbibition saturation range while reducing the premature disconnection of the NWP. Both the capillary pressure curves and subsequently the relative permeability results are sensitive to the wetting state of the system, which is mainly defined by the ratio between the spontaneous and forced part of the imbibition curve. Assuming the same starting point, e.g., residual wetting saturation, the imbibition modeling is mainly governed by the wetting contact angle as well as the volume of non-wetting material introduced. Both highly influence the spontaneous modeling which dictates the overall imbibition process, as it is a rather dominating process that can lead to an early disconnection of the NWP while the WP connectivity is strongly increased. Thereby both parameters govern the overall saturation range, as they control the advancement of the spontaneous front. The forced modeling approach is less dominating with regard to the

disconnection of phases leading, in contrast to the SI modeling, to smaller connectivity changes between two saturation stages. Hence the connectivity of the NWP, i.e., relative permeability, is strongly influenced by the wetting CA and volume of non-wetting material. On the other hand, the WP is less influenced which is observable by the similar trends of the WP relative permeabilities. The non-wetting CA mainly influences the endpoint connectivity of the WP. In the last chapter, it is demonstrated that the new modeling approaches allow for the matching of experimental data that was previously unattainable. The results indicate that the data is most accurately represented by a purely forced imbibition modeling approach. This observation could suggest that during the experiment, the occurrence of spontaneous imbibition was not observed. It is likely that these experiments were conducted in a forced mode with injection rates exceeding the natural imbibition rate. As such, a change in the wetting state in the simulation can be attributed to the shift from advancing to receding contact angles, when the phase is forcefully introduced into the porous media. Alternatively, it is also plausible that the forced imbibition modeling encompasses the effects of spontaneous imbibition when appropriate parameters associated with the wetting state of the system are selected. Since the relative permeabilities are non-unique further investigations of the topology of fluid phases are necessary to gain further insights on the imbibition modeling.

<div align="right">

Chapter 6

</div>

Topological Analysis

In the previous chapter, different modeling approaches were introduced and the sensitivities of parameters were investigated. The capillary pressure curves, hence also the relative permeabilities, do not deliver perfectly unique results and depend on the exact input parameters in terms of wetting properties. Therefore, it is possible that similar results on the continuum scale are coming from different microscopic configurations. In other words, a match of a relative permeability to, e.g., experimental data can be by chance. To achieve certainty, simulations or a combination of simulations and experiments can be compared based on the exact microscopic fluid configuration. Although the exact fluid configuration serves as a benchmark, it is realistically unattainable. Thus, the fluid topology, which encapsulates the essence of the fluid configuration, carries more significance. Given the complexity of fluid distribution in the pore space, the topological properties of the fluid phases are computed. This allows for comparison across different systems, with the fluid topology providing a more comprehensive comparison that extends beyond the exact fluid configuration. In chapter 2.3 the Minkowski functionals (MF) are introduced, which can be applied to quantify topological measures that deliver a fingerprint of our system. The analysis begins with the experimental data, as it provides the experimental fluid distributions that serve as the topological references. Later in the chapter, the influence of contact angles and their spatial distribution is investigated, and comparisons are made between different structures on a topological basis. The topological trends are then compared with the global trends computed in the previous chapter.

6.1   Topology of Experimental and Simulated Data

In Chapter 5.3, it is demonstrated that the morphological forced imbibition modeling leads to reasonable matches with the experimental relative permeability data. Three different approaches with varying parameters were used, which raises the question of whether the match with the experimental data is due to the specific choice of the input parameters, or if the modeling approaches are inherently robust. The experimental data set has been used in many different studies and therefore also some topological properties have already been computed.

So far mainly the Euler characteristic of the non-wetting phase was investigated (Berg et al. 2016a; Alpak et al. 2018). The Euler characteristic is a measure of the connectivity of a phase linking directly to the relative permeability of a phase. It is therefore often computed when relative permeabilities are simulated. The Euler characteristic is computed by summing the number of connected components and subtracting the number of holes from it as stated in Equation [9].
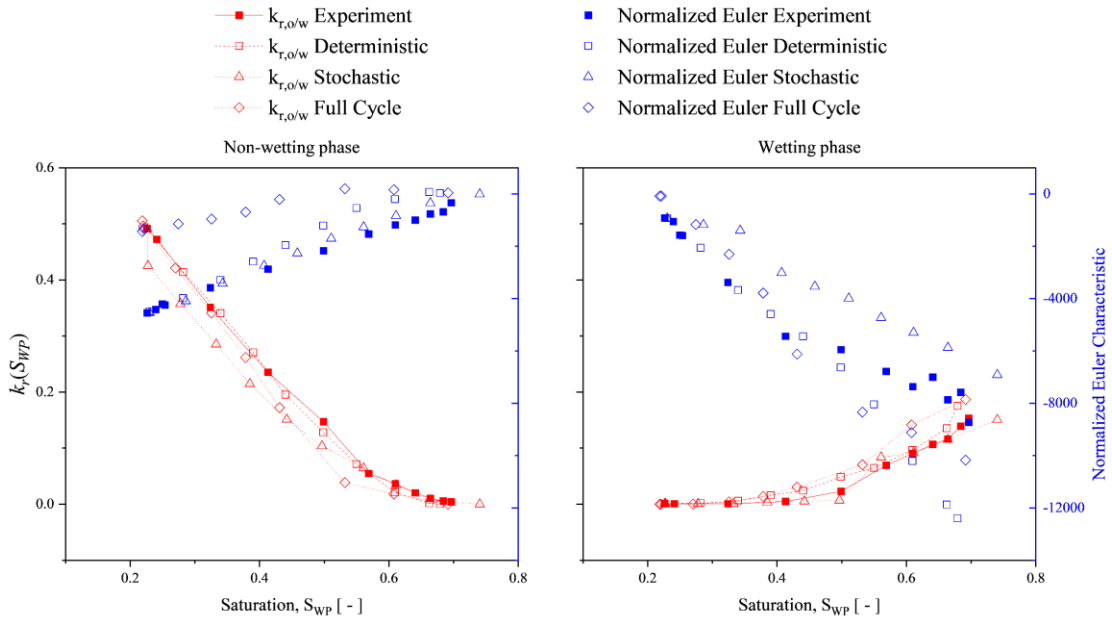
Figure 38 Normalized Euler characteristic of the wetting and non-wetting phase as a function of the wetting phase saturation for the simulated and experimental datasets. In red the respective relative permeability curve match is shown.

Since the Euler characteristic is additive data sets are typically filtered by applying a threshold value size below which clusters are removed from the statistics. This prevents small cluster sizes or single pixels, which can also be related to initial image noise, from adding to the total number. Another approach, as chosen in this thesis, employs a volume-weighted method, as proposed by (Ott et al. 2020):

$$\chi = \frac{\sum_{n_{cl}} \chi_{cl} V_{cl}}{\sum_{n_{cl}} V_{cl}} \qquad\qquad [\,11\,]$$

The normalization avoids arbitrary cut-offs and allows for the inclusion of the entire data set. In Figure 38 the computed values are plotted for the best matches of the experimental dataset as presented in Chapter 5.3. The stochastic and deterministic simulated approaches have the same starting point as they were computed from the experimental fluid distributions, the full cycle on the other hand starts from a simulated drainage distribution using the stochastic approach. In general, the trends are accurate for all scenarios, though there are deviations during various saturation stages. Focusing first on the non-wetting phase (left), the stochastic

approach's normalized Euler characteristic exhibits the best overall alignment with the experimental data, while the deterministic approach diverges at higher saturations. The full-cycle approach begins with an offset and appears to follow a different trend. In terms of relative permeability, the deterministic approach yields the best match at lower saturations, and the stochastic approach is more accurate at higher saturations.

Turning to the wetting phase (right), for both distributions modeled stochastically, it is observed that the trend is captured effectively in the early stage of imbibition, specifically within the saturation range up to 0.5. However, deviations are evident at higher saturations, indicated by an underestimation of the normalized Euler characteristic. This underestimation suggests an overestimation of the connectivity of the wetting phase, resulting in increased relative permeability compared to experimental results. In contrast, the stochastic approach overestimates the normalized Euler characteristic throughout the saturation range but displays a consistent trend with an offset at higher saturations. Notably, the stochastic approach yields the best match regarding the wetting phase's relative permeability, particularly in the low saturation range where the normalized Euler characteristic trend of the stochastic approach and experimental data diverge the most.

In the previous chapter, it was proposed that the governing factor in forced imbibition, depending on the implementation of the non-wetting material, is either the structure itself (deterministic) or the wettability distribution within the system (stochastic). Picking up those statements it would mean that with respect to the connectivity of the phases, hence the Euler characteristic, the early imbibition phase is driven by the structure, while the later stage is rather driven by the wettability of the system. However, the Euler characteristic alone is not enough to uniquely describe a system let alone are the trends as evident to entirely support such a statement. Therefore, the first and second Minkowski functionals (Equation [6] and [7]) were also computed and compared as a function of the wetting saturation, as shown in Figure 39.

Both the surface area and the mean curvature integral are normalized by division with the total volume of the structure. The surface area incorporates both fluid-fluid and fluid-rock interactions. When referring to the total volume of this structure, it encompasses the combined volume of the pores and grains. The specific value of both parameters is useful when computing different structures.
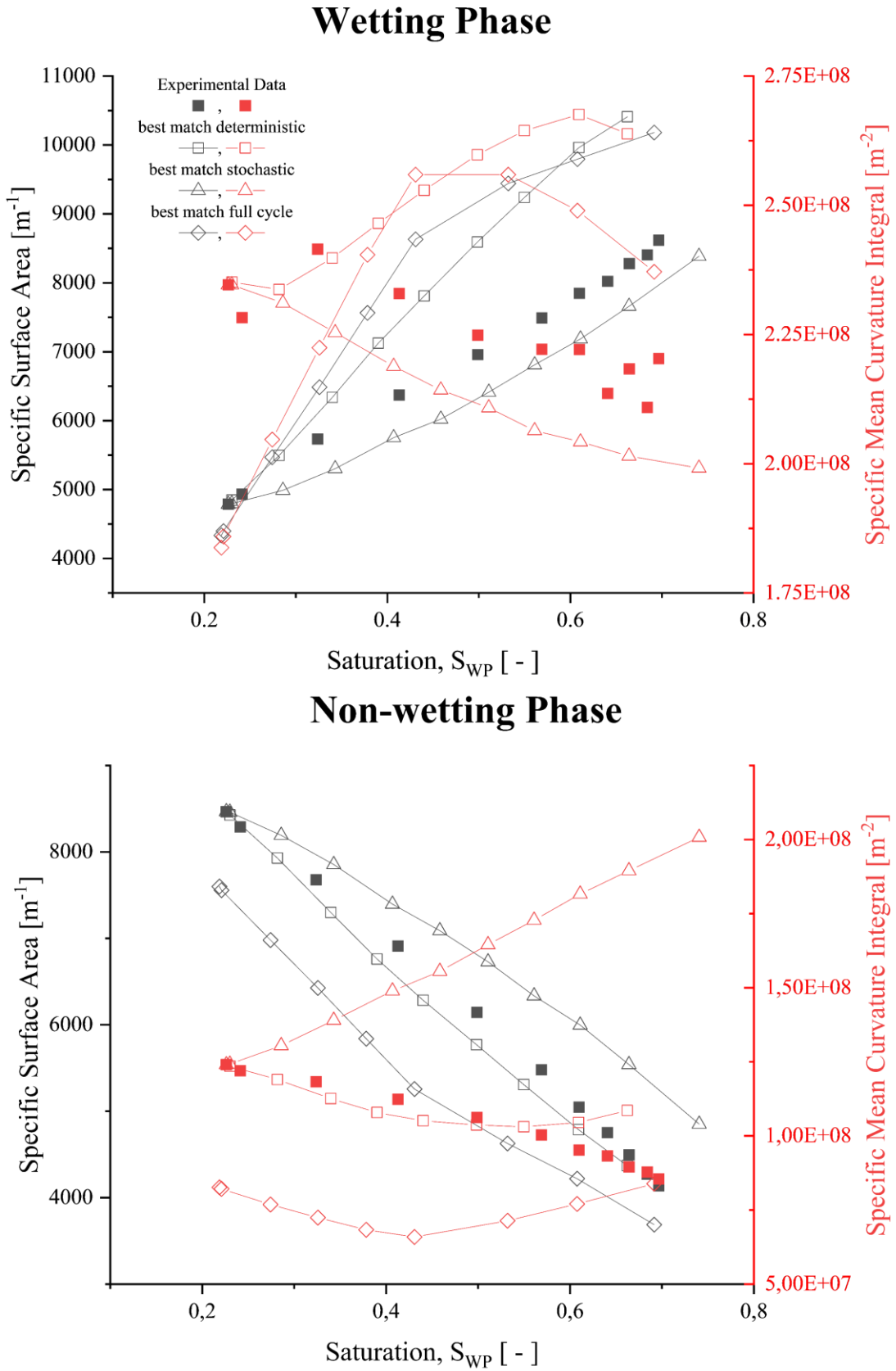
Figure 39 Specific surface area and specific mean curvature integral as a function of the wetting phase saturation of the wetting phase (top) and non-wetting phase (bottom) for simulated and experimental data.

Figure 39 shows that the experimental specific surface area of the WP increases with increasing volume, while the NWP surface area decreases with decreasing volume with both scaling linearly. It suggests that almost no additional interfaces develop during the displacement process and that existing interfaces between the phases are remaining which is also represented by the minor changes in the total specific surface area at the top right in Figure 40.
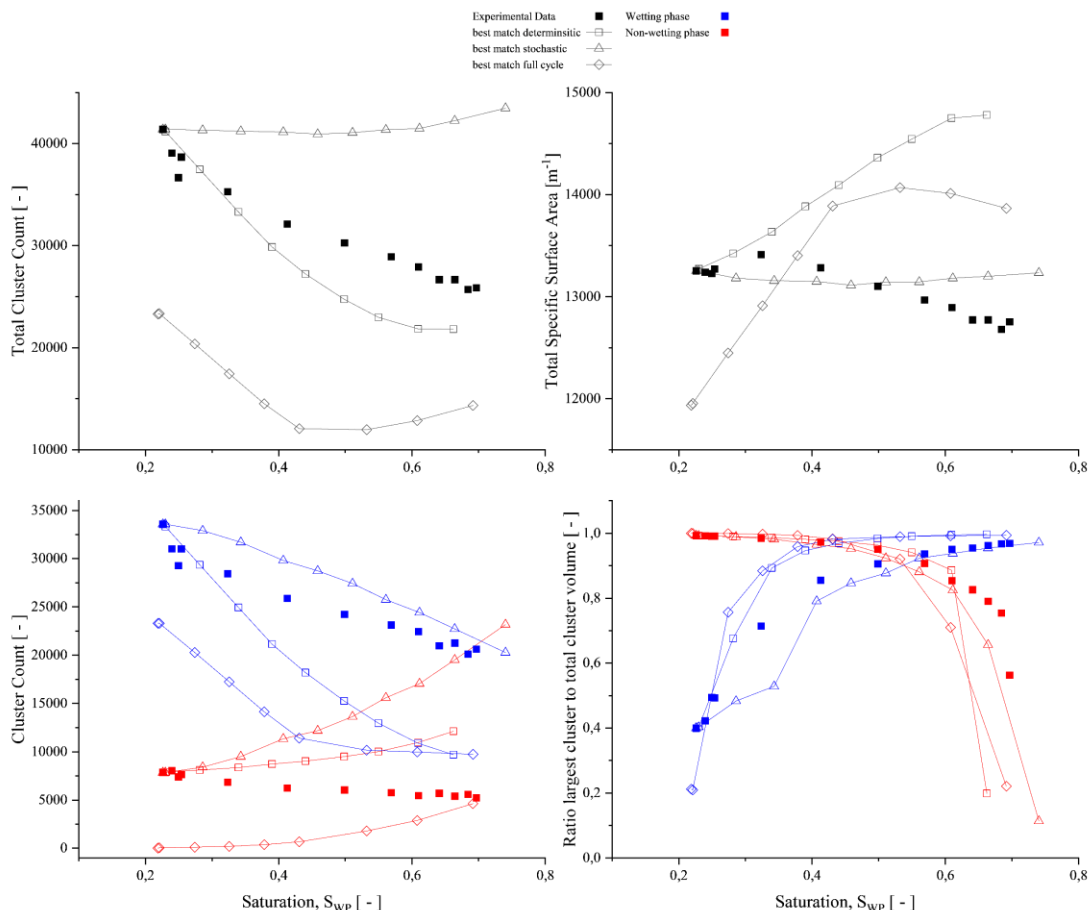
Figure 40 Total Cluster Count (top left), total specific surface area (top right), phase cluster count (bottom right) and phase cluster to total cluster volume (bottom right) as a function of the wetting phase saturation. In each graph, the experimental data is compared to the best match of the different simulated approaches.

The total is obtained by adding up the specific surface areas of the individual phases, similarly, the cluster count is the total of all clusters, but separated by the wetting and non-wetting phase. Yet, in the top left panel, the total number of clusters are plotted which show that with increasing WP saturation the total number of clusters decreases. It suggests that a lot of small clusters whose surface-to-volume ratio is small disappear by e.g., reconnecting to their phase and that snapped-off clusters are pore-filling while being connected to the grain surface. Figure 41 shows a depiction of the different volume fraction and surface area fraction changes when a new cluster is formed. The initial total surface area increase in the experimental data could be

caused by the development of pore-filling clusters, disconnected from the grain surface which would align with the experimental observations of film swelling by Berg et al. (Berg et al. 2016b).
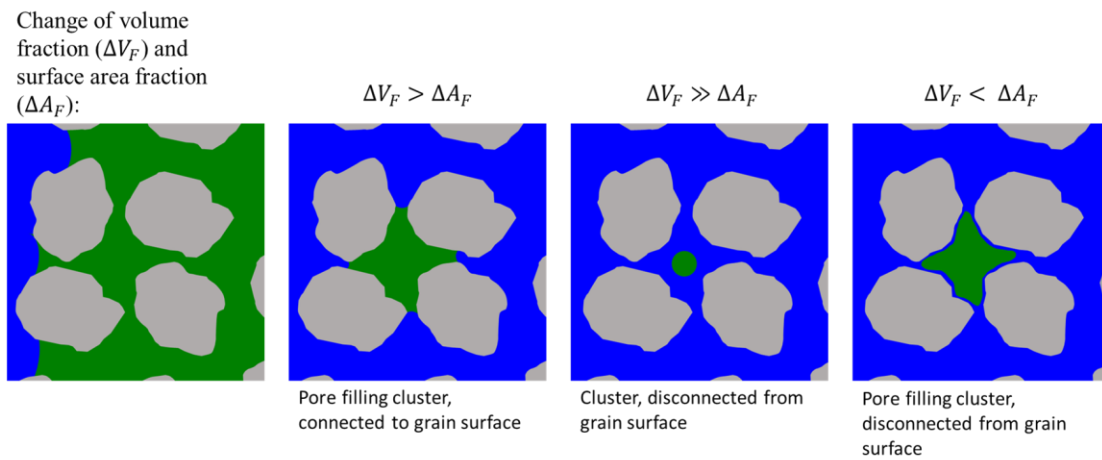
Figure 41 Visualization of how the surface area fraction and volume fraction of the phases can change during a displacement process. The surface area fraction includes the surface area between the phases and the grains.

The specific surface area trends of the NWP are similar for all datasets, with all of them declining. In contrast to that the WP data sets increase, but differ with the deterministic approach simulations showing a much steeper increase with increasing volumes. This shows in the total (top right Figure 40) as well, where the experimental data and stochastic approach change minorly compared to the other two.

In Figure 39 there is also the specific mean curvature integral plotted, where the general trend of the simulated data does not match the experimental data anymore. Here the WP trend is matched by the stochastic, whereas the NWP trend is matched by the deterministic approach for most of the saturation range. The specific mean curvature integral of the NWP scales with the cluster count of the NWP (bottom left of Figure 40). The same can be said for the WP for the experimental data and the stochastic approach, however, the other two show an increase in the specific mean curvature integral, whereas the cluster count decreases. In combination with the surface area, the findings suggest that there are more pore-filling clusters disconnected from the grains while the total number of individual clusters, especially the WP clusters decreases. This is the case when WP clusters re-establish connection to the invading front, while new NWP form and new interfaces develop. Contrarily, the experimental data reveals a reduction in the number of interfaces between WP and NWP as the displacement progresses. In the simulation, it's important to note that the NWP cluster count cannot decrease, since a cluster, once disconnected from the outlet, is rendered immobile and can no longer be displaced. Therefore, unless the specific boundary conditions permit it, the general trend is for the NWP

cluster count to increase. In contrast, in experiments, clusters can still mobilize, either disappearing from the field of view or coalesce with another cluster within the system. The decline in the experimental count of NWP clusters and the specific surface area indicates that smaller clusters are likely being expelled from the system. While these statistics undergo changes, the largest clusters dominate the complementary phase permeability, and as a result, the smaller clusters have a relatively minimal impact.

Computing the additional topological measures has shown that the approaches strongly differ from each other when it comes to the individual phase topology and distribution. However, in the previous chapter, it was demonstrated that the multiphase flow properties of the experimental data are matched by each of the approaches, proving that a solution exclusively based on the relative permeabilities is non-unique. The question is whether individual measures are mitigated by the overall measures of the system.

At the bottom right of Figure 40 the ratio of the largest cluster volume of the WP and NWP, respectively to the total cluster volume is plotted as a function of the WP saturation. A ratio of one means that the entire phase is accumulated in one single cluster. It can be seen that the NWP is dominated by a single cluster for almost the entire saturation range for all cases. During the drainage process, the NWP invades a pore when the capillary threshold (pore throat) is overcome while being connected to the invading front. Due to the nature of the simulation, the cluster count of the NWP at the end of a drainage process is 1, whereas in an experiment additional clusters can form due to nonsteady fluctuations during the displacement process. For example, a pore can be instantly filled by a Haines jump, where the volumetric change during the event can be bigger than the volume supply by the invading front (Berg et al. 2013). The WP on the other hand gets split up during the drainage until it typically consists of a lot of smaller clusters residing in smaller pores. On a sub-resolution scale (experimental μCT resolution), the WP can still be connected by a water film while appearing to be disconnected on the microscale. During imbibition these clusters can get reconnected, therefore reducing the total WP clusters. When it comes to the individual cluster statistics a difference in the data sets can be observed. The cluster count of the WP is underestimated by the deterministic approach, which coincides with the overestimation of the connectivity. Contrary the stochastic approach matches the WP but overestimates the NWP cluster count, however still matches both phase flow properties. It therefore can be assumed that the snapped-off clusters of the NPW are rather small and do not contribute to the overall connectivity of the phase. In general, it is evident that the relative permeabilities are primarily influenced by the largest clusters, which is expected since the effective permeability simulations consider only connected pathways. As a result, the

trends observed for both the size ratio of the largest cluster and the relative permeability exhibit similarities.

Overall, the impact of displacement events during imbibition on the topological characteristics of the system and their relationship with flow properties was examined. It was observed that the morphological forced imbibition modeling led to satisfactory matches with experimental relative permeability data using three distinct approaches. Notably, the flow properties could be effectively matched when the system was dominated by a single cluster governing the entire flow, implying that relative permeabilities are chiefly influenced by the largest clusters. Furthermore, the study revealed that the overall connectivity of this dominant cluster is predominantly dictated by the porous structure, while the statistics of individual clusters are influenced by the system's wettability. The stochastic and deterministic approaches exhibited divergent trends and statistics in topological measures. In the next chapter, a more detailed investigation is conducted to determine whether these changes coincide with the varying parameters of the individual approaches and the overall wetting state of the system.

6.2   Stochastic and Deterministic Parameter Sensitivity

In chapter 5.1.1, the wettability trends are presented, considering variations in the input parameters of both the deterministic and stochastic approaches. The systems proved to be sensible to the volumetric amount and distribution of non-wetting material. In the previous section, it was demonstrated that both approaches exhibited distinct topological measures, indicating that the wettability of the system plays a significant role in determining the displacement pattern.
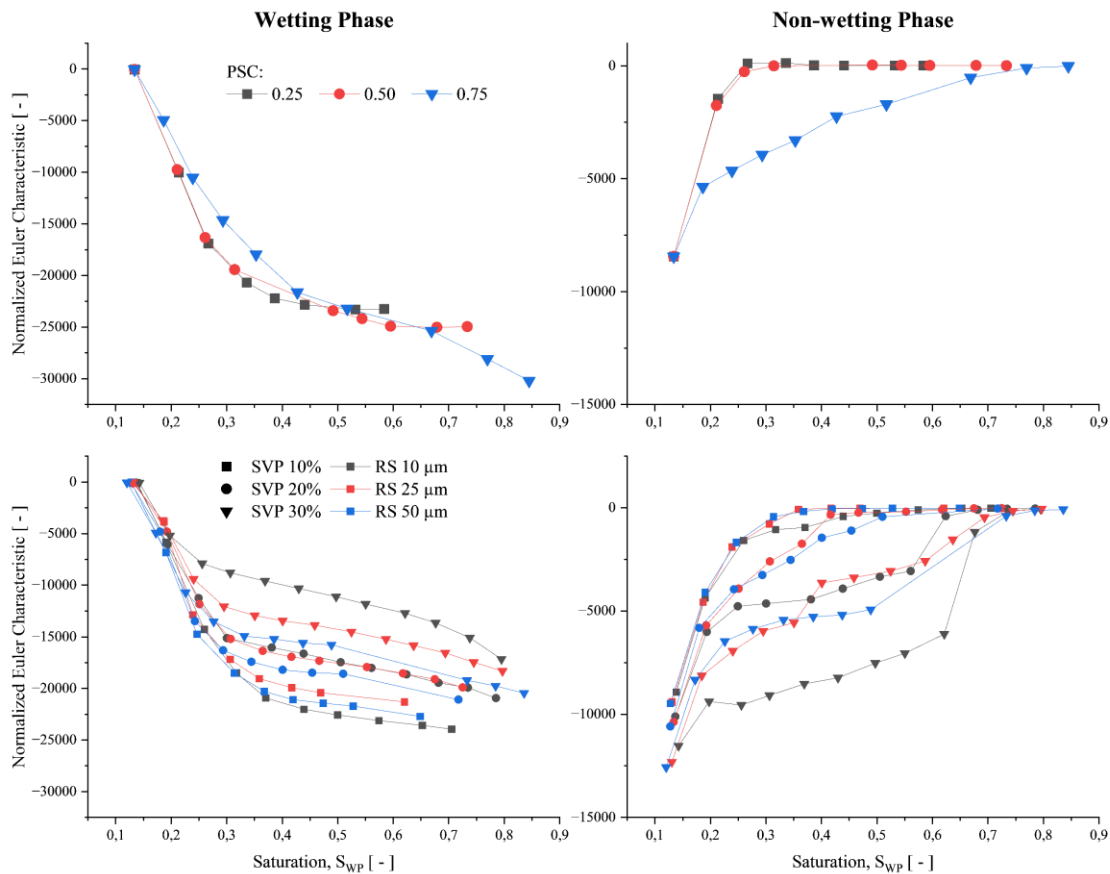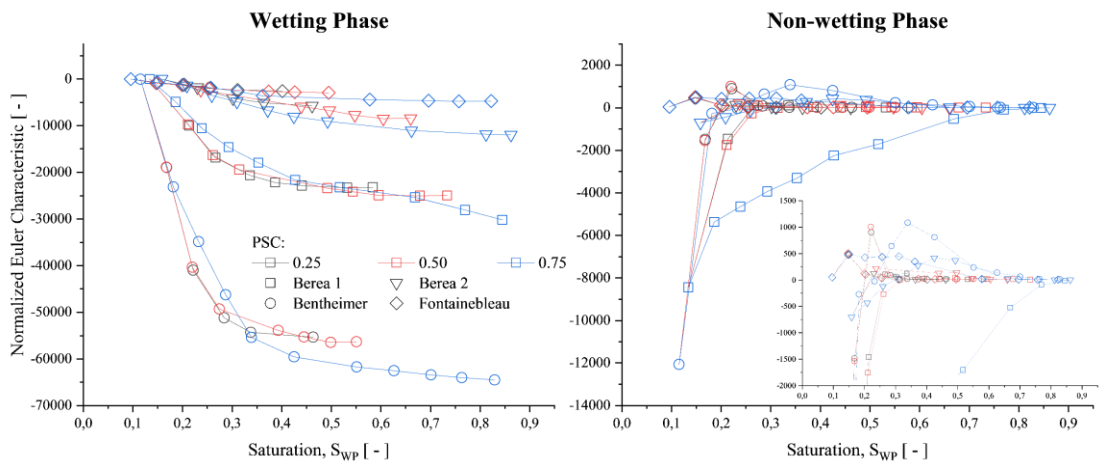
Figure 42 Normalized Euler characteristic as a function of the wetting phase saturation plotted for varying parameters of the deterministic (top) and stochastic (bottom) approach. The left side shows the wetting phase and the right side the non-wetting phase statistics.

The analysis begins by plotting and comparing the normalized Euler characteristic as a function of the WP saturation for both WP and NWP. In Figure 42 the comparison for different parameters associated with the wetting state of the system can be seen. The top of the panel shows the results of the deterministic approach for different PSC values. All curves have the same starting point, as the approach does not influence the drainage process resulting in the same starting point for the different simulations. The WP connectivity is almost unaffected by the PSC value, which mainly extends the saturation range. A value of 0.75 results in a less steep decrease of the normalized Euler characteristic as the imbibition process is mainly forced. This effect is more prominent on the NWP characteristics, as those steeply increase for low saturation for a spontaneous modeled process, e.g., PSC values of 0.25 and 0.5. The disconnection of the big cluster for low saturations, results in the sharp decrease of the flow conductivity and therefore reduced relative permeability saturation range of the NWP.

The stochastic approach is plotted for different SVP and RS values at the bottom panels. The normalized Euler characteristic shows very similar trends for all of the curves, with the values increasing with larger volumes of non-wetting material introduced. A sensitivity to the RS

becomes apparent for larger SVP values, e.g., 30%. The more the non-wetting material is distributed within the system (large SVP, small RS), the less the WP can connect within the system. Hence, scaling with the SI and FI saturation ranges. For the NWP normalized Euler characteristic, a similar behavior can be observed, however, the trends of the curve differ from each other. Especially the combination of a large SVP (30%) and small RS (10 μm) exhibits a different trend compared to the other curves, maintaining a low normalized Euler characteristic for a large saturation range. These differences are much more apparent and therefore more sensitive compared to the relative permeabilities of the WP and NWP for the same parameters as plotted in Figure 26.

Complementary to the normalized Euler characteristic in Figure 43 the specific surface areas and the specific mean curvature integrals are plotted as a function of the WP saturation for varying parameters of the deterministic and stochastic approach. On the left side, the wetting phase measures are plotted that exhibit no major changes compared to each other. In general, the trends are very similar and only vary with the SVP (bottom left panel), fitting the observations of the normalized Euler characteristic. On the other hand, the NWP measures are influenced stronger by the different deterministic and stochastic parameters. When setting a PSC value of 0.75 the specific mean curvature starts to strongly increase at a WP saturation of around 0.3 as here still one dominant oil cluster remains. In the other two cases, the number of oil clusters increases, while the largest cluster size ratio decreases hence becoming less dominant. In those cases, the snapped-off clusters have a significant volume whose interfaces scale with the overall volumetric change of the NWP. For a PSC value of 0.75 after a saturation of around 0.3 a lot of small clusters, e.g., spheres, form that do not account for a lot of surface area and volume, but mean curvature integral of the phase. For the stochastic approach even though less prominent this effect can be observed for a small RS and increasing SVP.
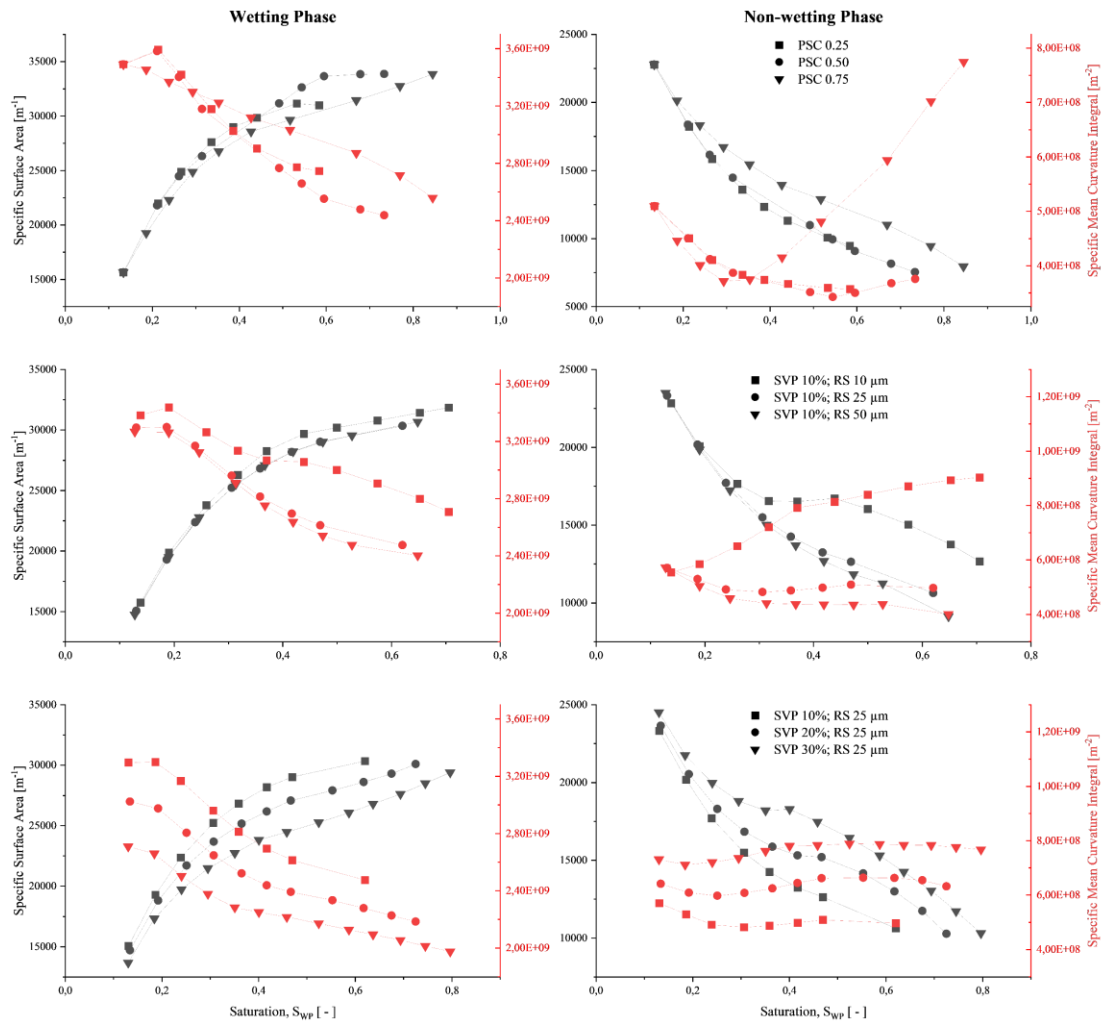
Figure 43 Specific surface area and specific mean curvature integral as a function of the wetting phase saturation plotted for the wetting phase (left) and non-wetting phase (right). The top shows the sensitivity of the topological measures for varying PSC (0.25, 0.5 and 0.75) values for the deterministic approach. The middle and the bottom panel show the sensitivities with respect to the RS (10, 25 and 50 μm) and SVP (10%, 20% and 30%) having the respective other parameter fixed for the stochastic approach.

Different trends were observed for the topological measures in the stochastic and deterministic approaches; however, overall, the systems exhibited similar behavior. This suggests that the results are robust and highly credible, emphasizing that the displacement process in this rock sample is largely dictated by the characteristics of the porous structure. However, it's important to note that deviations occur when there are significant changes in wetting properties, such as a high PSC value or a combination of small RS with high SVP. This denotes that while the porous structure plays a pivotal role, wetting changes are also influential in determining the outcome. In the subsequent chapter, further investigations will be conducted to examine the variations in topological measures in correlation with alterations in wetting and non-wetting contact angles. This aims to provide a more comprehensive understanding of the interactions between these factors.

6.3   Wetting and Non-wetting Contact Angle Sensitivities

In addition to the non-wetting material added to the structure, the wettability can be altered by changing the contact angle of the wetting and non-wetting material. In chapter 5.1.1.2 the sensitivities with respect to the CA changes have been thoroughly discussed. The observed trends indicate that the topology is likely to change when strong wetting conditions, such as contact angles of 0° or 180°, are applied.
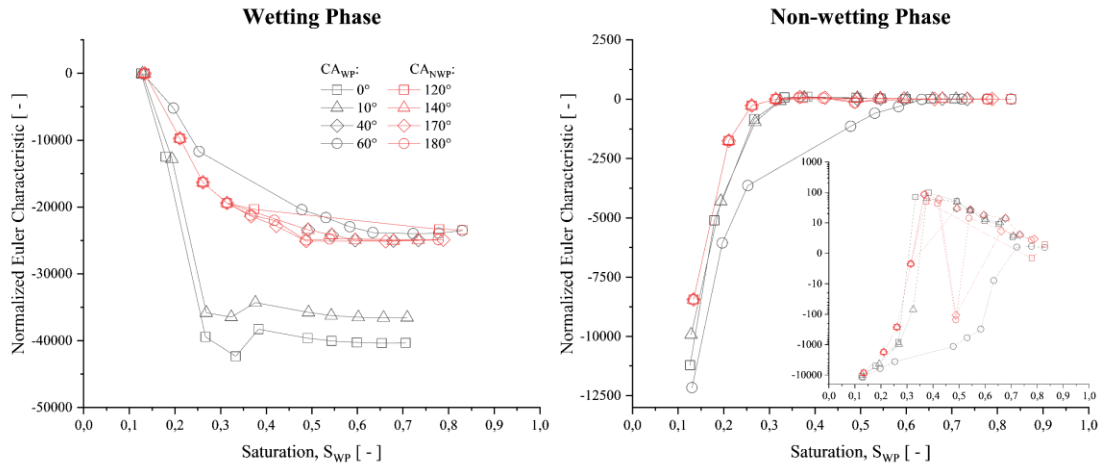
Figure 44 Normalized Euler characteristic as a function of the wetting phase saturation plotted for varying wetting and non-wetting contact angles. The left side shows the measures of the wetting phase and the right side of the non-wetting phase.

In Figure 44 the normalized Euler characteristic is plotted as a function of the WP saturation for varying wetting and non-wetting contact angles. The non-wetting CA was varied for a wetting CA of 40°. It is notable that the wetting contact angle strongly influences the characteristics of the WP (left) during the spontaneous imbibition process which can be observed in the drastic change at the start of the imbibition process. The non-wetting CA only affects the WP during the forced process, as anticipated according to the simulation algorithm. Complementary the NWP exhibits a similar behavior. Both phases are most influenced by the wetting CA with the biggest differences being observable between 0° and 60°. The outlier of the trend for the non-wetting CA of 170° and 180° is connected to the largest oil cluster strongly reducing, more than halving, in size which leads to a decreasing jump in the Euler characteristic of that cluster. This jump is connected to the disconnection of the NWP from the inlet/outlet. At this point, the NWP is not anymore connected throughout the domain anymore, which can be seen in Figure 30 by the cut-off of the NWP relative permeability. Subsequently, the cluster is breaking up into even smaller pieces resulting in a larger total Euler characteristic.
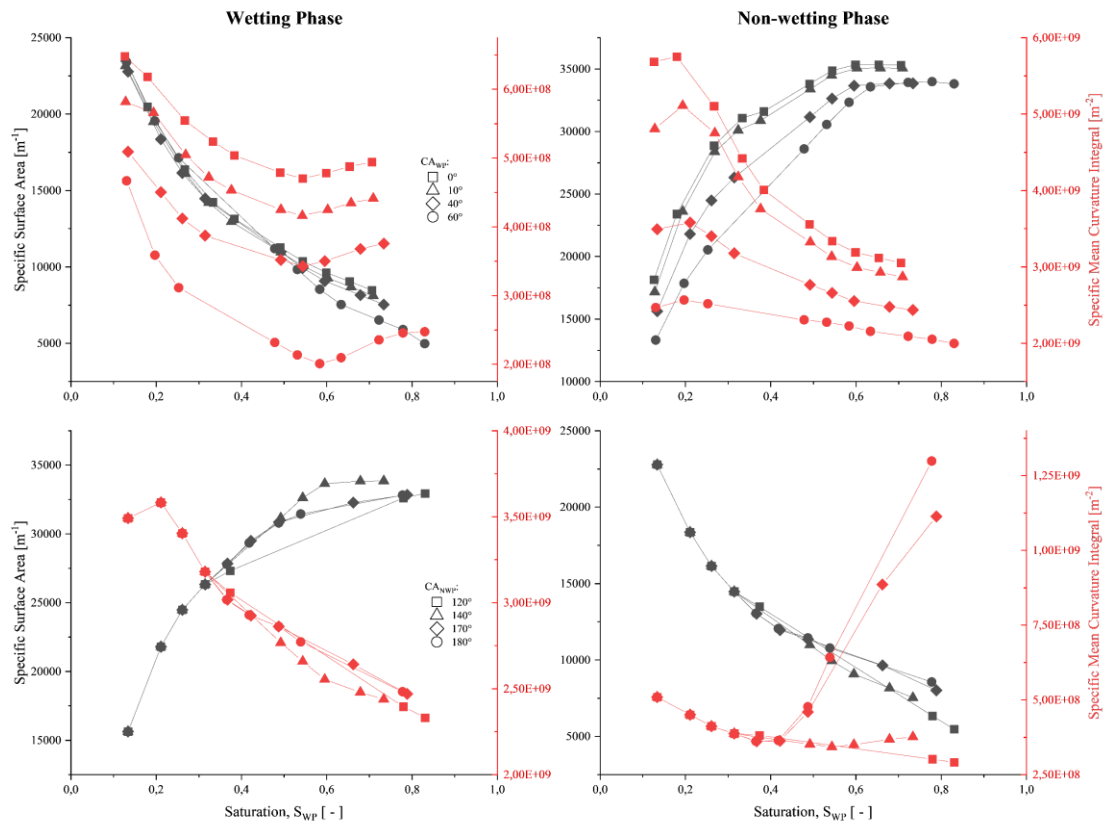
Figure 45 Specific surface area and specific mean curvature integral as a function of the wetting phase saturation plotted for the wetting phase (left) and non-wetting phase (right). The top shows the sensitivities with respect to the wetting contact angles and the bottom for the non-wetting contact angles.

Figure 45 shows the specific surface area and specific mean curvature integral as a function of the WP saturation for varying wetting and non-wetting contact angles. The surface area of the WP and NPW shows minimal sensitivity to the contact angles, although the NWP exhibits some degree of sensitivity to the wetting CA (top right). On the other hand, the specific mean curvature integral is influenced by the contact angle of the wetting phase. This indicates that the curvature between the phases depends on the wetting contact angle. Additionally, the influence of the non-wetting contact angle aligns with the previously observed trends, and the deviation from the trend appears to be correlated with the abrupt disconnection of the NWP phase.

The assigned contact angles do not majorly influence the nature of the displacement process, as the topological measures are comparable with each other. It appears that displacement is mainly governed by the structure unless strong wetting or non-wetting conditions are applied. However, even then the changes in the different statistics are very strong at the start for low saturation ranges. This suggests that a) the spontaneously modeled part of the imbibition

strongly governs the general displacement pattern and b) that the spontaneous imbibition is very robust to the applied contact angles.

6.4   Fluid-topological Trends for Different Rock Types

In the previous chapters, the evaluation of the topology of the wetting and non-wetting phases was conducted using the simulation approach, considering different wetting conditions. The findings reveal that the displacement process, particularly the spontaneous imbibition, plays a significant role in shaping the phase topology. It is noteworthy that substantial changes in the topology were primarily observed when the system exhibited strong wetting conditions. The observed changes in trends with varying wetting conditions indicate the robustness of the simulation approach.

In this chapter, a comparison of the same parameters as before is conducted for four different rock types, employing solely the deterministic approach. The results are presented in Figure 46 and Figure 47. The general trends for the WP and NWP are very similar between the different rock types. An increase in the PSC value leads to an extended saturation range, while the trend is mainly given by the start of the imbibition process, hence in the low saturations. For the NWP it can be observed that a PSC value of 0.75 leads to an increase in the specific mean curvature integral (bottom right Figure 47). This is similar to the deviations observed in the earlier chapters when strong wetting conditions were applied.

Figure 46 Normalized Euler characteristic as a function of the wetting phase saturation plotted for varying PSC values for different rock samples. The colors indicate a change in the PSC value with each rock having another shape. The left side shows the wetting phase and the right side the non-wetting phase.
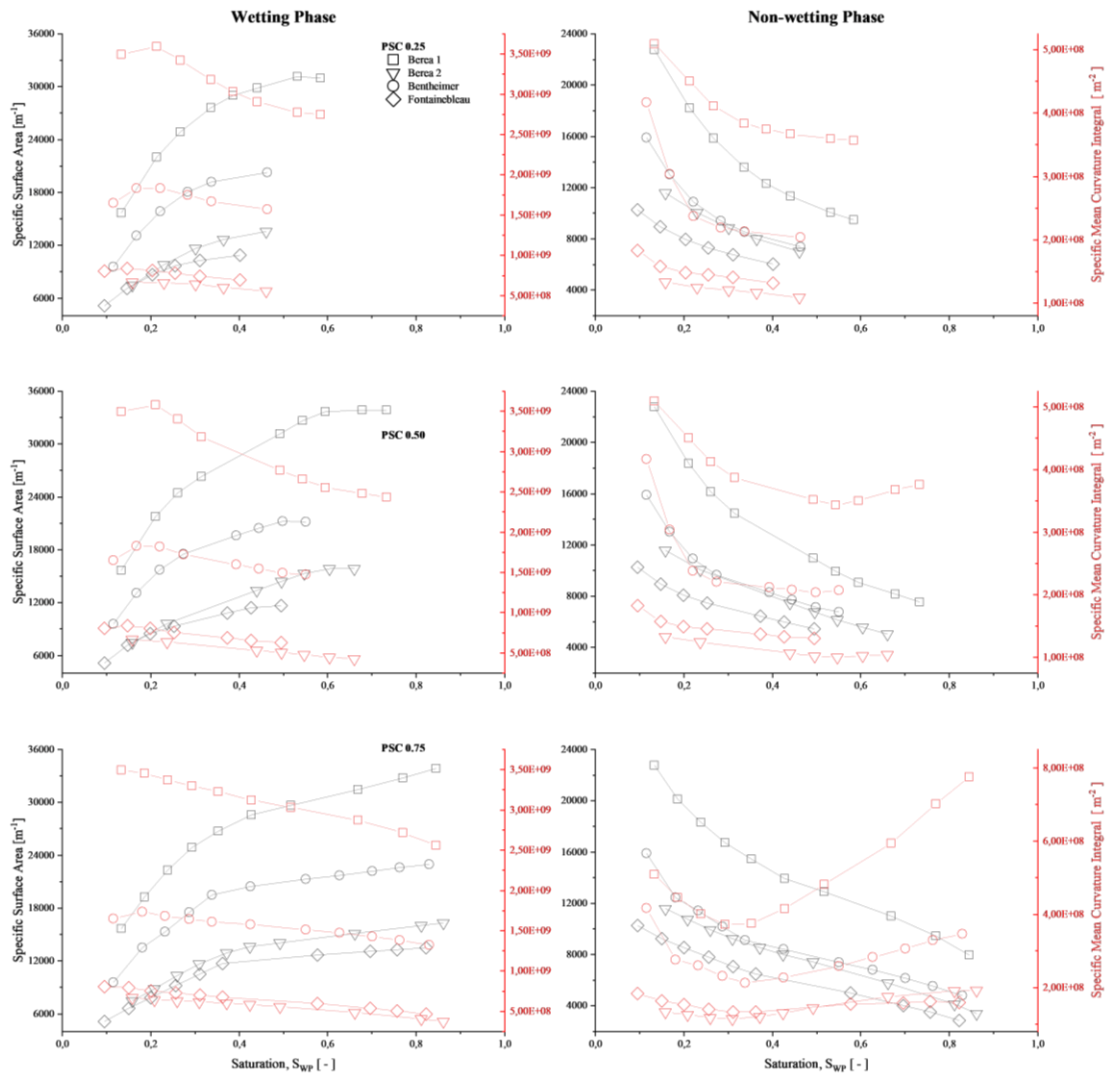
Figure 47 Specific surface area and specific mean curvature integral as a function of the wetting phase saturation plotted for the wetting phase (left) and non-wetting phase (right). In each graph, the four different samples are compared for a PSC value of 0.25, 0.50 and 0.75 top to bottom respectively.

The magnitude of the normalized Euler number correlates with the total number of pores, which is directly reflected in the WP plot. Here the number decreases with increasing volume, i.e., with the wetting-phase saturation. The NWP on the other hand shows a very similar behavior for all rock types, with the number converging towards 1. A normalized Euler number of one indicates that the majority of clusters consist of single entities without any inclusions, resembling dispersed bubbles, for example. Besides for a PSC value of 0.75, the normalized Euler numbers do not differ distinctively from each other. Even though the Bentheimer sample has the lowest of all NWP normalized Euler numbers, it shows the steepest increase at the beginning of the imbibition process after which it converges similarly to the Berea 2 and Fontainebleau sample. This sharp increase is related to the largest cluster decreasing in size whereas the Euler characteristic of it increases. That increase is mainly correlated to the cluster

disconnecting from the inlet, reducing the number of holes, as the WP is invading. The large number of pores and the high connectivity between them (large coordination number) seems to lead to a strong invasion of the WP with the NWP being disconnected quite early. Therefore, the NWP relative permeability is cut off at around 0.5 saturation units, while the residual saturation of the NWP is very low, i.e., the imbibition process extends over a long saturation range.

The number of pores and their connectivity clearly influence the imbibition displacement process. In combination with the pore throat size and pore diameter distribution, samples can be compared to each other even when porosity and permeability are completely different. The Berea 2 and the Fontainebleau show very similar trends while being categorized differently purely based on such petrophysical features. Supposing they are available, they could be used as an alternative way for categorizing different rock types.

6.5   Summary

In this chapter, the topological characteristics of the wetting and non-wetting phases were examined using different modeling approaches and varying wetting conditions. It was found that the capillary pressure curves and relative permeabilities are not uniquely determined and depend on the input parameters related to wetting properties. This implies that similar results on the macroscopic scale can arise from different microscopic configurations, and vice versa. To ensure a higher level of certainty, simulations were compared with experimental data on the exact microscopic fluid configurations. By computing topological properties, such as Minkowski functionals (MF), fingerprints of the system were obtained that provided insights into the fluid distribution in the complex pore space. As it has been found that MFs enable direct comparability of the micro and macro states of fluid saturation, independent of the precise microscopic saturation state, which varies from experiment to experiment. The experimental data were analyzed, and the influence of contact angles and their spatial distribution on different structures was investigated. The topological trends were compared with the global trends computed in previous chapters.

The topological analysis conducted in this chapter revealed that the spontaneous imbibition process is predominantly influenced by the individual pore structure, representing the topology of the porous medium. The impact of wetting conditions, although significant, was relatively small in comparison. It was observed that even when different rock types are considered, the topological *trends* are similar. The preferred population of non-wetting material in the larger pores combined with the nature of the spontaneous and forced algorithm leads to very similar patterns. However, differences in the saturation ranges are apparent which seem to connect to

the number of pores and their connectivity (coordination number). While the assigned contact angles provided information about the curvature between the phases, the trends of the topological measures remained relatively consistent. Exceptions are apparent when strong wetting conditions, e.g., $CA_{WP} = 0°\ or\ CA_{NWP} = 180°$, are applied, the process is mainly driven by the forced imbibition or non-wetting material is randomly distributed within the structure. The addition of non-wetting material forces the populating phase to take alternative routes. The comparison with experimental data has shown that the WP matches best using the stochastic and the NWP using the deterministic approach. Therefore, it can be inferred that a synthesis of both approaches is required to accurately determine the wetting state of a system. Hence, emphasizing how important the wettability distribution within a porous medium is.

Chapter 7

Conclusion

7.1   Summary

The intricate nature of multiphase flow on the pore scale necessitates innovative and simplified modeling approaches to accurately capture saturation functions efficiently. Among various techniques, the morphological method has stood out for its effectiveness in modeling capillary-driven processes, such as drainage, owing to its quasi-static nature. However, its limitations were evident in handling imbibition due to the absence of a time scale, as reported by prior research such as Berg et al. (Berg et al. 2016b).

A significant advancement has been made in this study, effectively addressing the limitations of the traditional morphological method by introducing a notable extension to incorporate forced imbibition. This extension serves as a crucial step in bridging the gap between model predictions and experimental data, bolstering the reliability of the morphological method in simulating multiphase flows. The innovative extension strategically entails the controlled termination of imbibition to prevent the disconnection of the non-wetting phase from the in- and outlet of the system. To achieve this, two strategies for the distribution of non-wetting material within the porous structure have been devised: a stochastic approach and a deterministic approach. These strategies represent a considerable improvement, contributing positively to the accuracy and applicability of multiphase flow modeling in porous media.

In the stochastic approach, non-wetting material is randomly distributed following Gaussian statistics, providing an element of randomness in the simulation. In contrast, the deterministic approach takes a more strategic path by prioritizing the allocation of non-wetting areas within the largest pores, specifically when these areas are in contact with the NWP at the end of the primary drainage process. The analysis delves into how these approaches affect saturation functions such as capillary pressure and relative permeability, and the role of wettability in these processes. The findings indicate that not only the volume but also the sizes of non-wetting materials introduced are crucial, with average pore throat size emerging as a significant factor. Moreover, connectivity is primarily determined by the interplay between spontaneous and

forced modeling, as spontaneous imbibition leads to an early cut-off of the non-wetting phase. The influence of wetting and non-wetting contact angles is also examined, with the wetting contact angles playing a significant role during the spontaneous imbibition process. However, the endpoints and residual saturations are more impacted by the NWP CA as the forced imbibition is governed by them. It was also demonstrated that a gradient of contact angles will lead to changes in the endpoints, suggesting that defining grain-specific contact angles should be considered for accurate modeling. Overall, the saturation functions modeled through this novel approach exhibit a good alignment with trends observed in experimental data upon altering the wettability. This coherence underscores the robustness and reliability of the method while underlining the importance of the wettability of the porous medium in accurately capturing the complexities of multiphase flow dynamics.

The new extension was then validated by comparing it to experimental data from Berg et al. (Berg et al. 2016b), showcasing a good match. By adjusting different parameters, the model can represent a broad range of wetting states. However, the study raises the question of data reliability due to the high degrees of freedom in the simulation. To address this, topological measures were computed, and trends were analyzed based on input parameters with experimental fluid distributions as reference points. The results indicated distinct topologies for the WP and NWP, and the best match compared to experimental data was obtained through the stochastic approach for the WP and the deterministic approach for the NWP. The parameter sensitivities indicate that the topology is strongly governed by the spontaneous imbibition.

In conclusion, this work has successfully extended the imbibition process and analyzed the associated changes in fluid topologies. The significantly enhanced morphological method emerges as a capable pore-scale simulation method that can produce fluid distributions for various wetting conditions. While the wetting state of a solid surface does not necessarily change from drainage to imbibition, the implemented changes in CA in the simulations can be associated with the shift from advancing to receding contact angles. This can correspond to increased injection rates in an experimental context. The displacement processes are found to be intimately interconnected with the porous structure, as well as the wettability preferences of specific regions within it. The method boasts rapid simulation performance and is adept at computing microscopic fluid distributions within the system, making it well-suited for conducting in-depth uncertainty analyses.

7.2   Outlook

The best matches with the experimental data were achieved when entirely modeling the imbibition as forced. Through computing the topologies of the phases, it was validated that the experimental data partially aligned with the models (WP and NWP each with a different approach). However, this raises pertinent questions: Was there an absence of spontaneous imbibition during the experiment, or is this data inherently incorporated when modeling forced imbibition? Although it is highly plausible that the experiment did not experience any wettability changes post-primary drainage, the injection rate might have significantly exceeded the rate of spontaneous imbibition. This suggests that processes of this nature can be effectively modeled through forced imbibition, provided that a reasonable receding non-wetting CA is utilized.

To refine these findings, there is a compelling need for more experimental data with enhanced temporal resolution and varied injection rates. An experiment of interest could involve comparing AMOTT and high-rate core flooding experiments, which represent the extremes of spontaneous and force-dominated displacements, respectively. Additionally, the integration of simplified modeling approaches that incorporate pseudo-viscous or dynamic effects warrants further exploration. The accessibility of microscopic fluid distribution analysis enhances the feasibility of comparing experimental and numerical results. The inclusion of film swelling, as observed by Berg et al. (Berg et al. 2016b), may bridge the connectivity discrepancies among phases. However, this would necessitate the incorporation of sub-resolution modeling, culminating in multiscale modeling. Moreover, it is vital to understand how saturation functions of porous regions (including sub-resolution regions) can be integrated into resolved pore-space modeling, given their critical role in phase connectivity.

Another promising avenue for investigation is the strategic allocation of wettability through contact angles for distinct grain types. Traditional grayscale imaging often results in binary segmentation (pore and grain) due to constraints such as resolution, contrast, and available information. However, advancements in image quality and the advent of modern machine-learning algorithms have made multiphase segmentation increasingly viable, enabling the assignment of different wetting states to various minerals or grains.

In this study, the contact angle during displacement was modeled based on Schulz et al., which is ineffective near 90° (Schulz et al. 2015). As such, the model allows for mixed wetting but not neutral wetting conditions. In GeoDict 2023, a novel "True Contact Angle" approach has been introduced, resolving this limitation (Math2Market GmbH et al. 2023).

In summary, both the modeling methodologies and our comprehension of multiphase displacement processes require further advancement. Nonetheless, it is evident that actual

processes adhere to certain patterns that can be modeled without the necessity for exhaustive knowledge. This suggests that strategic approximations and informed assumptions can pave the way for the development of effective and practical modeling techniques.

References

Aghaei, A., & Piri, M. (2015). Direct pore-to-core up-scaling of displacement processes: Dynamic pore network modeling and experimentation. *Journal of Hydrology*, *522*, 488–509. https://doi.org/10.1016/j.jhydrol.2015.01.004

Ahrenholz, B., Tölke, J., Lehmann, P., Peters, A., Kaestner, A., Krafczyk, M., & Durner, W. (2008). Prediction of capillary hysteresis in a porous material using lattice-Boltzmann methods and comparison to experimental data and a morphological pore network model. *Advances in Water Resources*, *31*(9), 1151–1173. https://doi.org/10.1016/j.advwatres.2008.03.009

Al-Gharbi, M. S., & Blunt, M. J. (2005). Dynamic network modeling of two-phase drainage in porous media. *Physical Review. E, Statistical, Nonlinear, and Soft Matter Physics*, *71*(1 Pt 2), 16308. https://doi.org/10.1103/PhysRevE.71.016308

Alhammadi, A. M., AlRatrout, A., Singh, K., Bijeljic, B., & Blunt, M. J. (2017). In situ characterization of mixed-wettability in a reservoir rock at subsurface conditions. *Scientific Reports*, *7*(1), 10753. https://doi.org/10.1038/s41598-017-10992-w

Al-Kharusi, A. S., & Blunt, M. J. (2007). Network extraction from sandstone and carbonate pore space images. *Journal of Petroleum Science and Engineering*, *56*(4), 219–231. https://doi.org/10.1016/j.petrol.2006.09.003

Alpak, F. O., Berg, S [S.], & Zacharoudiou, I [I.] (2018). Prediction of fluid topology and relative permeability in imbibition in sandstone rock by direct numerical simulation. *Advances in Water Resources*, *122*, 49–59. https://doi.org/10.1016/j.advwatres.2018.09.001

AlRatrout, A., Blunt, M. J., & Bijeljic, B. (2018). Spatial Correlation of Contact Angle and Curvature in Pore-Space Images. *Water Resources Research*, *54*(9), 6133–6152. https://doi.org/10.1029/2017WR022124

AlRatrout, A., Raeini, A. Q., Bijeljic, B., & Blunt, M. J. (2017). Automatic measurement of contact angle in pore-space images. *Advances in Water Resources*, *109*, 158–169. https://doi.org/10.1016/j.advwatres.2017.07.018

Amott, E. (1959). Observations Relating to the Wettability of Porous Rock. *Transactions of the AIME*, *216*(01), 156–162. https://doi.org/10.2118/1167-G

Anderson, W. (1986). Wettability Literature Survey- Part 2: Wettability Measurement. *Journal of Petroleum Technology*, *38*(11), 1246–1262. https://doi.org/10.2118/13933-PA

Andrä, H., Combaret, N., Dvorkin, J., Glatt, E., Han, J., Kabel, M., Keehm, Y., Krzikalla, F., Lee, M., Madonna, C., Marsh, M., Mukerji, T., Saenger, E. H., Sain, R., Saxena, N., Ricker, S., Wiegmann, A [Andreas], & Zhan, X. (2013a). Digital rock physics benchmarks—Part I: Imaging and segmentation. *Computers & Geosciences*, *50*, 25–32. https://doi.org/10.1016/j.cageo.2012.09.005

Andrä, H., Combaret, N., Dvorkin, J., Glatt, E., Han, J., Kabel, M., Keehm, Y., Krzikalla, F., Lee, M., Madonna, C., Marsh, M., Mukerji, T., Saenger, E. H., Sain, R., Saxena, N., Ricker, S., Wiegmann, A [Andreas], & Zhan, X. (2013b). Digital rock physics benchmarks—part II: Computing effective properties. *Computers & Geosciences*, *50*, 33–43. https://doi.org/10.1016/j.cageo.2012.09.008

Andrew, M., Bijeljic, B., & Blunt, M. J. (2014). Pore-scale contact angle measurements at reservoir conditions using X-ray microtomography. *Advances in Water Resources*, *68*, 24–31. https://doi.org/10.1016/j.advwatres.2014.02.014

Armstrong, R. T., Georgiadis, A [Apostolos], Ott, H [Holger], Klemin, D., & Berg, S [Steffen] (2014). Critical capillary number: Desaturation studied with fast X-ray computed microtomography. *Geophysical Research Letters*, *41*(1), 55–60. https://doi.org/10.1002/2013GL058075

Armstrong, R. T., McClure, J. E., Berrill, M. A., Rücker, M [Maja], Schlüter, S [Steffen], & Berg, S [Steffen] (2016). Beyond Darcy's law: The role of phase topology and ganglion dynamics for two-fluid flow. *Physical Review. E*, *94*(4-1), 43113. https://doi.org/10.1103/PhysRevE.94.043113

Armstrong, R. T., McClure, J. E., Robins, V., Liu, Z., Arns, C. H., Schlüter, S [Steffen], & Berg, S [Steffen] (2019). Porous Media Characterization Using Minkowski Functionals: Theories, Applications and Future Directions. *Transport in Porous Media*, *130*(1), 305–335. https://doi.org/10.1007/s11242-018-1201-4

Armstrong, R. T., Sun, C., Mostaghimi, P., Berg, S [Steffen], Rücker, M [Maja], Luckham, P., Georgiadis, A [Apostolos], & McClure, J. E. (2021). Multiscale Characterization of Wettability in Porous Media. *Transport in Porous Media*, *140*(1), 215–240. https://doi.org/10.1007/s11242-021-01615-0

Arnold, P., Dragovits, M., Linden, S., Hinz, C., & Ott, H [Holger] (2023). Forced imbibition and uncertainty modeling using the morphological method. *Advances in Water Resources*, *172*, 104381. https://doi.org/10.1016/j.advwatres.2023.104381

Becker, J [Jürgen], Schulz, V., & Wiegmann, A [Andreas] (2008). Numerical Determination of Two-Phase Material Parameters of a Gas Diffusion Layer Using Tomography Images. *Journal of Fuel Cell Science and Technology*, *5*(2), Article 021006. https://doi.org/10.1115/1.2821600

Berg, S [S.], Rücker, M [M.], Ott, H [H.], Georgiadis, A [A.], van der Linde, H [H.], Enzmann, F [F.], Kersten, M [M.], Armstrong, R. T [R. T.], With, S. de, Becker, J [J.], & Wiegmann, A [A.] (2016). Modeling of Imbibition Relative Permeability by Direct Quasi-Static Approach. *The 2016 International Symposium of the Society of Core Analysts (SCA 2016)*.

Berg, S [Steffen], Ott, H [Holger], Klapp, S. A., Schwing, A [Alex], Neiteler, R [Rob], Brussee, N [Niels], Makurat, A [Axel], Leu, L [Leon], Enzmann, F [Frieder], Schwarz, J.-O., Kersten, M [Michael], Irvine, S., & Stampanoni, M. (2013). Real-time 3D imaging of Haines jumps in porous media flow. *Proceedings of the National Academy of Sciences of the United States of America*, *110*(10), 3755–3759. https://doi.org/10.1073/pnas.1221373110

Berg, S [Steffen], Rücker, M [Maja], Ott, H [Holger], Georgiadis, A [Apostolos], van der Linde, H [Hilbert], Enzmann, F [Frieder], Kersten, M [Michael], Armstrong, R. T., With, S. de, Becker, J [Jürgen], & Wiegmann, A [Andreas] (2016). Connected pathway relative permeability from pore-scale imaging of imbibition. *Advances in Water Resources*, *90*, 24–35. https://doi.org/10.1016/j.advwatres.2016.01.010

Berg, S [Stuart], Kutra, D., Kroeger, T., Straehle, C. N., Kausler, B. X., Haubold, C., Schiegg, M., Ales, J., Beier, T., Rudy, M., Eren, K., Cervantes, J. I., Xu, B., Beuttenmueller, F., Wolny, A., Zhang, C., Koethe, U., Hamprecht, F. A., & Kreshuk, A. (2019). Ilastik: Interactive machine learning for (bio)image analysis. *Nature Methods*, *16*(12), 1226–1232. https://doi.org/10.1038/s41592-019-0582-9

Blunt, M. J. (2017). *Multiphase Flow in Permeable Media*. Cambridge University Press. https://doi.org/10.1017/9781316145098

Blunt, M. J., Lin, Q., Akai, T., & Bijeljic, B. (2019). A thermodynamically consistent characterization of wettability in porous media using high-resolution imaging. *Journal of Colloid and Interface Science*, *552*, 59–65. https://doi.org/10.1016/j.jcis.2019.05.026

Boek, E. S., & Venturoli, M. (2010). Lattice-Boltzmann studies of fluid flow in porous media with realistic rock geometries. *Computers & Mathematics with Applications*, *59*(7), 2305–2314. https://doi.org/10.1016/j.camwa.2009.08.063

Bultreys, T [Tom], Lin, Q., Gao, Y., Raeini, A. Q., AlRatrout, A., Bijeljic, B., & Blunt, M. J. (2018). Validation of model predictions of pore-scale fluid distributions during two-phase flow. *Physical Review. E*, *97*(5-1), 53104. https://doi.org/10.1103/PhysRevE.97.053104

Bultreys, T [Tom], Singh, K., Raeini, A. Q., Ruspini, L. C [Leonardo C.], Øren, P.-E., Berg, S [Steffen], Rücker, M [Maja], Bijeljic, B., & Blunt, M. J. (2020). Verifying Pore Network Models of Imbibition in Rocks Using Time-Resolved Synchrotron Imaging. *Water Resources Research*, *56*(6). https://doi.org/10.1029/2019WR026587

Churcher, P. L., French, P. R., Shaw, J. C., & Schramm, L. L. (1991). Rock Properties of Berea Sandstone, Baker Dolomite, and Indiana Limestone. In *SPE International Symposium on Oilfield Chemistry*. Society of Petroleum Engineers. https://doi.org/10.2118/21044-MS

Donaldson, E. C., & Alam, W. (2008a). Wettability. In *Wettability* (pp. 1–55). Elsevier. https://doi.org/10.1016/B978-1-933762-29-6.50007-7

Donaldson, E. C., & Alam, W. (2008b). Wettability and Production. In *Wettability* (pp. 121–172). Elsevier. https://doi.org/10.1016/B978-1-933762-29-6.50009-0

Donaldson, E. C., Thomas, R. D., & Lorenz, P. B. (1969). Wettability Determination and Its Effect on Recovery Efficiency. *Society of Petroleum Engineers Journal*, *9*(01), 13–20. https://doi.org/10.2118/2338-PA

Dong, H., & Blunt, M. J. (2009). Pore-network extraction from micro-computerized-tomography images. *Physical Review. E, Statistical, Nonlinear, and Soft Matter Physics*, *80*(3 Pt 2), 36307. https://doi.org/10.1103/physreve.80.036307

Dullien, F. A. L. (2015). *Porous Media: Fluid Transport and Pore Structure* (Second edition). Acedemic Press.

Foroughi, S., Bijeljic, B., Lin, Q., Raeini, A. Q., & Blunt, M. J. (2020). Pore-by-pore modeling, analysis, and prediction of two-phase flow in mixed-wet rocks. *Physical Review. E*, *102*(2-1), 23302. https://doi.org/10.1103/PhysRevE.102.023302

Garfi, G [Gaetano], John, C. M., Rücker, M [Maja], Lin, Q., Spurin, C., Berg, S [Steffen], & Krevor, S [Samuel] (2022). Determination of the spatial distribution of wetting in the pore networks of rocks. *Journal of Colloid and Interface Science*, *613*, 786–795. https://doi.org/10.1016/j.jcis.2021.12.183

Garing, C., Voltolini, M., Ajo-Franklin, J. B., & Benson, S. M. (2017). Pore-scale Evolution of Trapped CO2 at Early Stages Following Imbibition Using Micro-CT Imaging. *Energy Procedia*, *114*, 4872–4878. https://doi.org/10.1016/j.egypro.2017.03.1628

Gharbi, O., & Blunt, M. J. (2012). The impact of wettability and connectivity on relative permeability in carbonates: A pore network modeling analysis. *Water Resources Research*, *48*(12). https://doi.org/10.1029/2012WR011877

Hadwiger, H. (1975). *Vorlesungen über Inhalt, Oberflache und Isoperimetrie*. *Grundlehren der mathematischen Wissenschaften, A Series of Comprehensive Studies in Mathematics: Vol. 93*. Springer. https://doi.org/10.1007/978-3-642-94702-5

Hassanizadeh, S [S.Majid], & Gray, W. G. (1990). Mechanics and thermodynamics of multiphase flow in porous media including interphase boundaries. *Advances in Water Resources*, *13*(4), 169–186. https://doi.org/10.1016/0309-1708(90)90040-B

Hazlett, R. D. (1995). Simulation of capillary-dominated displacements in microtomographic images of reservoir rocks. *Transport in Porous Media*, *20*(1-2), 21–35. https://doi.org/10.1007/BF00616924

Heijmans, H. J. A. M. (1995). Mathematical Morphology: A Modern Approach in Image Processing Based on Algebra and Geometry. *SIAM Review*, *37*(1), 1–36. https://doi.org/10.1137/1037001

Herring, A. L., Harper, E. J., Andersson, L., Sheppard, A., Bay, B. K., & Wildenschild, D [Dorthe] (2013). Effect of fluid topology on residual nonwetting phase trapping: Implications for geologic CO2 sequestration. *Advances in Water Resources*, *62*, 47–58. https://doi.org/10.1016/j.advwatres.2013.09.015

Higgs, S., Da Wang, Y., Sun, C., Ennis-King, J., Jackson, S. J., Armstrong, R. T., & Mostaghimi, P. (2022). In-situ hydrogen wettability characterisation for underground hydrogen storage. *International Journal of Hydrogen Energy*, *47*(26), 13062–13075. https://doi.org/10.1016/j.ijhydene.2022.02.022

Hilfer, R. (1998). Macroscopic equations of motion for two-phase flow in porous media. *Physical Review E*, *58*(2), 2090–2096. https://doi.org/10.1103/PhysRevE.58.2090

Hilfer, R. (2001). *Review on Scale Dependent Characterization of the Microstructure of Porous Media*. https://arxiv.org/pdf/cond-mat/0105458

Hilpert, M., & Miller, C. T. (2001). Pore-morphology-based simulation of drainage in totally wetting porous media. *Advances in Water Resources*, *24*(3-4), 243–255. https://doi.org/10.1016/S0309-1708(00)00056-7

Hirasaki, G. J., Rohan, J. A., Dubey, S. T., & Niko, H. (1990). Wettability Evaluation During Restored-State Core Analysis. In *All Days*. SPE. https://doi.org/10.2118/20506-MS

Høiland, L. K., Spildo, K., & Skauge, A. (2007). Fluid flow properties for different classes of intermediate wettability as studied by network modeling. *Transport in Porous Media*, *70*(1), 127–146. https://doi.org/10.1007/s11242-006-9088-x

Joekar Niasar, V., Hassanizadeh, S. M [S. M.], Pyrak-Nolte, L. J., & Berentsen, C. (2009). Simulating drainage and imbibition experiments in a high-porosity micromodel using an unstructured pore network model. *Water Resources Research*, *45*(2). https://doi.org/10.1029/2007WR006641

Joekar-Niasar, V., Doster, F., Armstrong, R. T [R. T.], Wildenschild, D [D.], & Celia, M. A. (2013). Trapping and hysteresis in two-phase flow in porous media: A pore-network study. *Water Resources Research*, *49*(7), 4244–4256. https://doi.org/10.1002/wrcr.20313

Joekar-Niasar, V., & Hassanizadeh, S. M [S. M.] (2012). Analysis of Fundamentals of Two-Phase Flow in Porous Media Using Dynamic Pore-Network Models: A Review. *Critical Reviews in Environmental Science and Technology*, *42*(18), 1895–1976. https://doi.org/10.1080/10643389.2011.574101

Joekar-Niasar, V., Hassanizadeh, S. M [S. M.], & DAHLE, H. K. (2010). Non-equilibrium effects in capillarity and interfacial area in two-phase flow: Dynamic pore-network modeling. *Journal of Fluid Mechanics*, *655*, 38–71. https://doi.org/10.1017/s0022112010000704

Khanamiri, H. H., Berg, C. F., Slotte, P. A., Schlüter, S [Steffen], & Torsæter, O. (2018). Description of Free Energy for Immiscible Two-Fluid Flow in Porous Media by Integral Geometry and Thermodynamics. *Water Resources Research*, *54*(11), 9045–9059. https://doi.org/10.1029/2018WR023619

Legland, D., Arganda-Carreras, I., & Andrey, P. (2016). Morpholibj: Integrated library and plugins for mathematical morphology with ImageJ. *Bioinformatics (Oxford, England)*, *32*(22), 3532–3534. https://doi.org/10.1093/bioinformatics/btw413

Lenormand, R., Touboul, E., & Zarcone, C. (1988). Numerical models and experiments on immiscible displacements in porous media. *Journal of Fluid Mechanics*, *189*, 165–187. https://doi.org/10.1017/S0022112088000953

Leverett, M. C. (1941). Capillary Behavior in Porous Solids. *Transactions of the AIME*, *142*(01), 152–169. https://doi.org/10.2118/941152-G

Linden, S., Wiegmann, A [Andreas], & Hagen, H. (2015). The LIR space partitioning system applied to the Stokes equations. *Graphical Models*, *82*, 58–66. https://doi.org/10.1016/j.gmod.2015.06.003

Lindquist, W. B., Lee, S.-M., Coker, D. A., Jones, K. W., & Spanne, P. (1996). Medial axis analysis of void structure in three-dimensional tomographic images of porous media. *Journal of Geophysical Research: Solid Earth*, *101*(B4), 8297–8310. https://doi.org/10.1029/95JB03039

Liu, H., Kang, Q., Leonardi, C. R., Schmieschek, S., Narváez, A., Jones, B. D., Williams, J. R., Valocchi, A. J., & Harting, J. (2016). Multiphase lattice Boltzmann simulations for porous media applications. *Computational Geosciences*, *20*(4), 777–805. https://doi.org/10.1007/s10596-015-9542-3

Liu, M., Meakin, P., & Huang, H. (2007). Dissipative particle dynamics simulation of pore-scale multiphase fluid flow. *Water Resources Research*, *43*(4). https://doi.org/10.1029/2006WR004856

Liu, Z., Herring, A., Arns, C., Berg, S [Steffen], & Armstrong, R. T. (2017). Pore-Scale Characterization of Two-Phase Flow Using Integral Geometry. *Transport in Porous Media*, *118*(1), 99–117. https://doi.org/10.1007/s11242-017-0849-5

Ma, S., & Morrow, N. R. (1994). Effect of Firing on Petrophysical Properties of Berea Sandstone. *SPE Formation Evaluation*, *9*(03), 213–218. https://doi.org/10.2118/21045-PA

Math2Market. (2022). *MatDict User Guide*. https://doi.org/10.30423/userguide.geodict2022-matdict

Math2Market GmbH, Becker, J [Jürgen], Biebl, F., Cheng, L., Glatt, E., Grießer, A., Groß, M., Linden, S., Mosbach, D., Wagner, C., Weber, A., Westerteiger, R., & Wiegmann, A [Andreas]. (2023). *Geodict Releases 2023*. Math2Market GmbH. https://doi.org/10.30423/release.geodict2023

McClure, J. E., Armstrong, R. T., Berrill, M. A., Schlüter, S [Steffen], Berg, S [Steffen], Gray, W. G., & Miller, C. T. (2018). Geometric state function for two-fluid flow in porous media. *Physical Review Fluids*, *3*(8). https://doi.org/10.1103/PhysRevFluids.3.084306

McClure, J. E., Li, Z., Berrill, M., & Ramstad, T. (2021). The LBPM software package for simulating multiphase flow on digital images of porous rocks. *Computational Geosciences*, *25*(3), 871–895. https://doi.org/10.1007/s10596-020-10028-9

McClure, J. E., Ramstad, T., Li, Z., Armstrong, R. T., & Berg, S [Steffen] (2020). Modeling Geometric State for Fluids in Porous Media: Evolution of the Euler Characteristic. *Transport in Porous Media*, *133*(2), 229–250. https://doi.org/10.1007/s11242-020-01420-1

Mecke, K. R., & Stoyan, D. (2000). *Statistical physics and spatial statistics: The art of analyzing and modeling spatial structures and pattern formation*. *Lecture notes in physics: Vol. 554*. Springer Verlag.

Murison, J., Semin, B., Baret, J.-C., Herminghaus, S., Schröter, M., & Brinkmann, M. (2014). Wetting Heterogeneities in Porous Media Control Flow Dissipation. *Physical Review Applied*, *2*(3). https://doi.org/10.1103/PhysRevApplied.2.034002

Niessner, J., Berg, S [Steffen], & Hassanizadeh, S. M [S. Majid] (2011). Comparison of Two-Phase Darcy's Law with a Thermodynamically Consistent Approach. *Transport in Porous Media*, *88*(1), 133–148. https://doi.org/10.1007/s11242-011-9730-0

Ott, H [Holger], Kharrat, A., Borji, M., & Arnold, P. (2020). Fluid-phase topology of complex displacements in porous media. *Physical Review Research*, *2*(2). https://doi.org/10.1103/PhysRevResearch.2.023240

Peksa, A. E., Wolf, K.-H. A., & Zitha, P. L. (2015). Bentheimer sandstone revisited for experimental purposes. *Marine and Petroleum Geology*, *67*, 701–719. https://doi.org/10.1016/j.marpetgeo.2015.06.001

Pepper, J. F., Witt, W. de, & Demarest, D. F. (1954). Geology of the Bedford Shale and Berea Sandstone in the Appalachian Basin. *Science (New York, N.Y.)*, *119*(3094), 512–513. https://doi.org/10.1126/science.119.3094.512-a

Raeesi, B., & Piri, M. (2009). The effects of wettability and trapping on relationships between interfacial area, capillary pressure and saturation in porous media: A pore-scale network modeling approach. *Journal of Hydrology*, *376*(3-4), 337–352. https://doi.org/10.1016/j.jhydrol.2009.07.060

Ramstad, T., Kristoffersen, A., & Ebeltoft, E. (2020). Uncertainty span for relative permeability and capillary pressure by varying wettability and spatial flow directions utilizing pore scale modeling. *E3S Web of Conferences*, *146*, 1002. https://doi.org/10.1051/e3sconf/202014601002

Regaieg, M., & Moncorgé, A. (2017). Adaptive dynamic/quasi-static pore network model for efficient multiphase flow simulation. *Computational Geosciences*, *21*(4), 795–806. https://doi.org/10.1007/s10596-017-9661-0

Rücker, M [M.], Bartels, W.-B., Garfi, G [G.], Shams, M., Bultreys, T [T.], Boone, M., Pieterse, S., Maitland, G. C., Krevor, S [S.], Cnudde, V., Mahani, H., Berg, S [S.], Georgiadis, A [A.], & Luckham, P. F. (2020). Relationship between wetting and capillary

pressure in a crude oil/brine/rock system: From nano-scale to core-scale. *Journal of Colloid and Interface Science*, *562*, 159–169. https://doi.org/10.1016/j.jcis.2019.11.086

Rücker, M [M.], Berg, S [S.], Armstrong, R. T [R. T.], Georgiadis, A [A.], Ott, H [H.], Schwing, A [A.], Neiteler, R [R.], Brussee, N [N.], Makurat, A [A.], Leu, L [L.], Wolf, M., Khan, F., Enzmann, F [F.], & Kersten, M [M.] (2015). From connected pathway flow to ganglion dynamics. *Geophysical Research Letters*, *42*(10), 3888–3894. https://doi.org/10.1002/2015GL064007

Ruecker, M., Berg, S [Steffen], Armstrong, R., Ott, H [Holger], simon, L., Enzmann, F [Frieder], Kersten, M [Michael], & With, S. (2015). *The Fate of Oil Clusters during Fractional Flow: Trajectories in the Saturation-Capillary Number Space.*

Ruspini, L. C [L. C.], Øren, P. E., Berg, S [S.], Masalmeh, S., Bultreys, T [T.], Taberner, C., Sorop, T., Marcelis, F., Appel, M., Freeman, J., & Wilson, O. B. (2021). Multiscale Digital Rock Analysis for Complex Rocks. *Transport in Porous Media*, *139*(2), 301–325. https://doi.org/10.1007/s11242-021-01667-2

Saadi, F. A., Wolf, K.-H., & van Kruijsdijk, C. (2017). Characterization of Fontainebleau Sandstone: Quartz Overgrowth and its Impact on Pore-Throat Framework. *Journal of Petroleum & Environmental Biotechnology*, *08*(03). https://doi.org/10.4172/2157-7463.1000328

Sahimi, M. (2011). *Flow and Transport in Porous Media and Fractured Rock: From Classical Methods to Modern Approaches* (2., wesentlich überarb. u. erw. Auflage). Wiley-VCH.

Scanziani, A., Lin, Q., Alhosani, A., Blunt, M. J., & Bijeljic, B. (2020). Dynamics of fluid displacement in mixed-wet porous media. *Proceedings. Mathematical, Physical, and Engineering Sciences*, *476*(2240), 20200040. https://doi.org/10.1098/rspa.2020.0040

Scanziani, A., Singh, K., Blunt, M. J., & Guadagnini, A. (2017). Automatic method for estimation of in situ effective contact angle from X-ray micro tomography images of two-phase flow in porous media. *Journal of Colloid and Interface Science*, *496*, 51–59. https://doi.org/10.1016/j.jcis.2017.02.005

Schlüter, S [S.], Berg, S [S.], Rücker, M [M.], Armstrong, R. T [R. T.], Vogel, H.-J., Hilfer, R., & Wildenschild, D [D.] (2016). Pore-scale displacement mechanisms as a source of hysteresis for two-phase flow in porous media. *Water Resources Research*, *52*(3), 2194–2205. https://doi.org/10.1002/2015WR018254

Schulz, V. P., Wargo, E. A., & Kumbur, E. C. (2015). Pore-Morphology-Based Simulation of Drainage in Porous Media Featuring a Locally Variable Contact Angle. *Transport in Porous Media*, *107*(1), 13–25. https://doi.org/10.1007/s11242-014-0422-4

Serra, J. (1982). *Image Analysis and Mathematical Morphology*. *Image Analysis and Mathematical Morphology*. Academic Press. https://books.google.at/books?id=6pZTAAAAYAAJ

Silin, D., & Patzek, T. (2006). Pore space morphology analysis using maximal inscribed spheres. *Physica a: Statistical Mechanics and Its Applications*, *371*(2), 336–360. https://doi.org/10.1016/j.physa.2006.04.048

Singh, K., Jung, M., Brinkmann, M., & Seemann, R. (2019). Capillary-Dominated Fluid Displacement in Porous Media. *Annual Review of Fluid Mechanics*, *51*(1), 429–449. https://doi.org/10.1146/annurev-fluid-010518-040342

Singh, K., Menke, H., Andrew, M., Lin, Q., Rau, C., Blunt, M. J., & Bijeljic, B. (2017). Dynamics of snap-off and pore-filling events during two-phase fluid flow in permeable media. *Scientific Reports*, *7*(1), 5192. https://doi.org/10.1038/s41598-017-05204-4

Singh, K., Scholl, H., Brinkmann, M., Di Michiel, M., Scheel, M., Herminghaus, S., & Seemann, R. (2017). The Role of Local Instabilities in Fluid Invasion into Permeable Media. *Scientific Reports*, *7*(1), 444. https://doi.org/10.1038/s41598-017-00191-y

Steffen Berg, Ryan Armstrong, & Andreas Weigmann. (2018). *Gildehauser Sandstone*. https://doi.org/10.17612/P7WW95

Tiab, D., & Donaldson, E. C. (2015). *Petrophysics: Theory and Practice of Measuring Reservoir Rock and Fluid Transport Properties*. Elsevier Science.

Valvatne, P. H., & Blunt, M. J. (2004). Predictive pore-scale modeling of two-phase flow in mixed wet media. *Water Resources Research*, *40*(7). https://doi.org/10.1029/2003WR002627

Vogel, H. J. (2000). A numerical experiment on pore size, pore connectivity, water retention, permeability, and solute transport using network models. *European Journal of Soil Science*, *51*(1), 99–105. https://doi.org/10.1046/j.1365-2389.2000.00275.x

Vogel, H.-J., Tölke, J., Schulz, V. P [V. P.], Krafczyk, M., & Roth, K. (2005). Comparison of a Lattice-Boltzmann Model, a Full-Morphology Model, and a Pore Network Model for Determining Capillary Pressure-Saturation Relationships. *Vadose Zone Journal*, *4*(2), 380–388. https://doi.org/10.2136/vzj2004.0114

Wael Abdallah, Jill S. Buckley, Andrew Carnegie, John Edwars, Bernd Herold, Edmund Fordham, Arne Graue, Tarek Habashy, Nikita Seleznev, Claude Sighner, Hassan Hussain, Bernhard Montaron, & Murtaza Ziauddin (2007). Fundamentals of Wettability, 44–61.

Zacharoudiou, I [Ioannis], Boek, E. S., & Crawshaw, J. (2018). The impact of drainage displacement patterns and Haines jumps on CO2 storage efficiency. *Scientific Reports*, *8*(1), 15561. https://doi.org/10.1038/s41598-018-33502-y

List of publications and conference proceedings

Arnold, Pit; Dragovits, Mario; Linden, Sven; Hinz, Christian; Ott, Holger (2023): Forced imbibition and uncertainty modeling using the morphological method. In: *Advances in Water Resources* 172, S. 104381. DOI: 10.1016/j.advwatres.2023.104381.

Arnold, P., Dragovits, M., Linden, S., Zekiri, F., & Ott, H [Holger] (2022). Forced Imbibition and Uncertainty Modelling using the Morphological Method. SCA Symposium 2022. https://jgmaas.com/SCA/2022/SCA2022-15.pdf

Burmester, G.; Jones, A.; Jurcic, H.; Amrollahinasab, O.; Arnold, P.; Ott, H. (2023): Predictions of Relative Permeability and Fractional Flow on Log Scale – Pilot Projects Results. In: 84th EAGE Annual Conference & Exhibition. 84th EAGE Annual Conference & Exhibition. Vienna, Austria, June 5-8, 2023: European Association of Geoscientists & Engineers, S. 1–5.

Burmester, G.; Zekiri, F.; Jurcic, H.; Arnold, P.; Ott, H. (2022): Integration and Upscaling of Multi-Phase Fluid Flow Properties in Clastic Reservoirs. In: 83rd EAGE Annual Conference & Exhibition. 83rd EAGE Annual Conference & Exhibition. Madrid, Spain / Online, Spain, June 6-9, 2022: European Association of Geoscientists & Engineers, S. 1–5.

Hassannayebi, Neda; Jammernegg, Boris; Schritter, Johanna; Arnold, Pit; Enzmann, Frieder; Kersten, Michael et al. (2021): Relationship Between Microbial Growth and Hydraulic Properties at the Sub-Pore Scale. In: *Transp Porous Med* 139 (3), S. 579–593. DOI: 10.1007/s11242-021-01680-5.

Kharrat, Ahmad; Brandstätter, Bianca; Borji, Mostafa; Ritter, Rene; Arnold, Pit; Fritz-Popovski, Gerhard et al. (2022): Development of foam-like emulsion phases in porous media flow. In: *Journal of colloid and interface science* 608 (Pt 1), S. 1064–1073. DOI: 10.1016/j.jcis.2021.10.022.

Ott, Holger; Kharrat, Ahmad; Borji, Mostafa; Arnold, Pit (2020): Fluid-phase topology of complex displacements in porous media. In: *Phys. Rev. Research* 2 (2). DOI: 10.1103/PhysRevResearch.2.023240.

Reinhardt, Marcel; Jacob, Arne; Sadeghnejad, Saeid; Cappuccio, Francesco; Arnold, Pit; Frank, Sascha et al. (2022): Benchmarking conventional and machine learning segmentation techniques for digital rock physics analysis of fractured rocks. In: *Environ Earth Sci* 81 (3). DOI: 10.1007/s12665-021-10133-7.

Sadeghnejad, Saeid; Reinhardt, Marcel; Enzmann, Frieder; Arnold, Pit; Brandstätter, Bianca; Wilde, Fabian et al. (2023): Minkowski functional evaluation of representative elementary volume of rock microtomography images at multiple resolutions. In: *Advances in Water Resources*, S. 104501. DOI: 10.1016/j.advwatres.2023.104501.

Zekiri, F.; Steckhan, J.; Linden, S.; Arnold, P.; Ott, H. (2020): Novel Digital Rock Simulation Approach in Characterizing Gas Trapping by Modified Morphological Workflow. In: First EAGE Digitalization Conference and Exhibition. First EAGE Digitalization Conference and Exhibition. Vienna, Austria, November 30 - December 3, 2020: European Association of Geoscientists & Engineers, S. 1–5.

Appendix

Appendix A

Capillary Pressure Curves

Figure 48 displays the capillary pressure curves derived from Berea 1 to assess the sensitivity to varying wetting conditions.
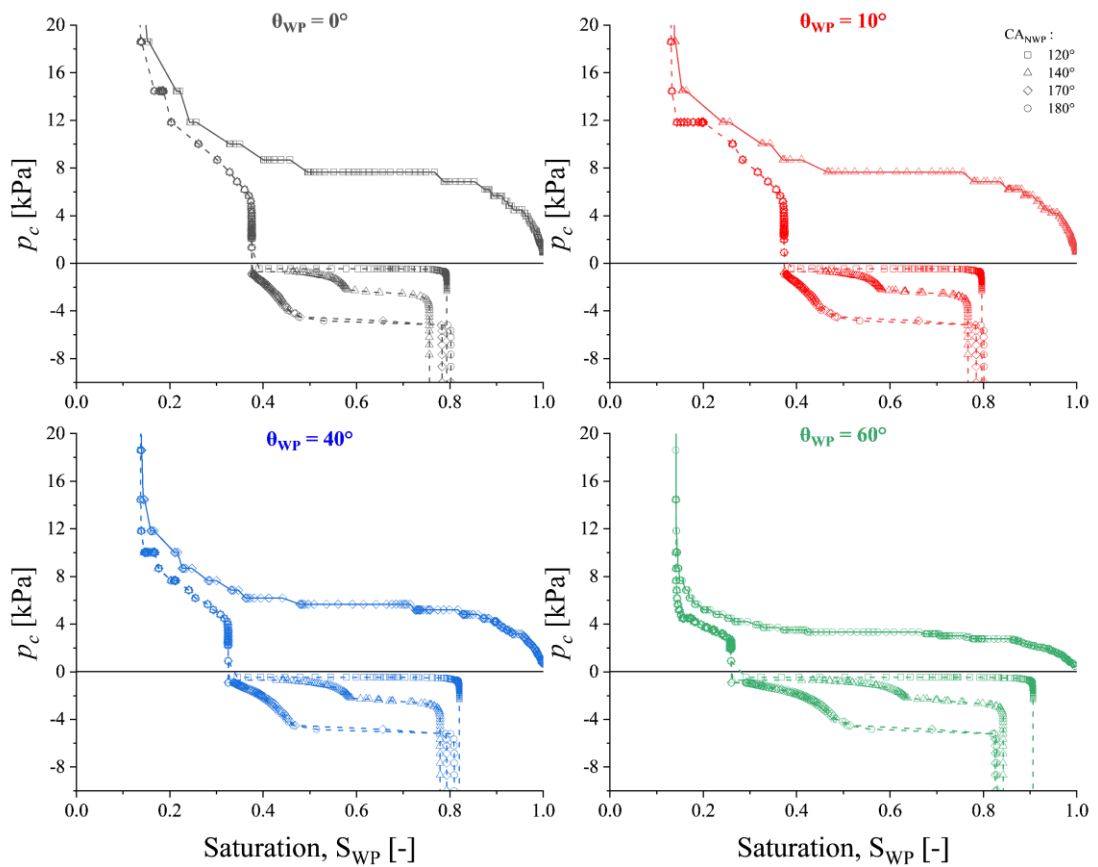
Figure 48 Capillary pressure curves illustrating different combinations of wetting (0°, 10°, 40° and 60°) and non-wetting contact angle (120°, 140°, 170° and 180°) for the Berea 1 sample, using the deterministic approach with a PSC value of 0.50.

In the figure, various colors represent distinct wetting contact angles, while different symbols indicate the non-wetting contact angles. A deterministic approach with a PSC value of 0.50 was used for the simulations. The trends of the curves are very similar across different contact angles, primarily altering the point where $p_c = 0$, as well as affecting the residual non-wetting saturations.
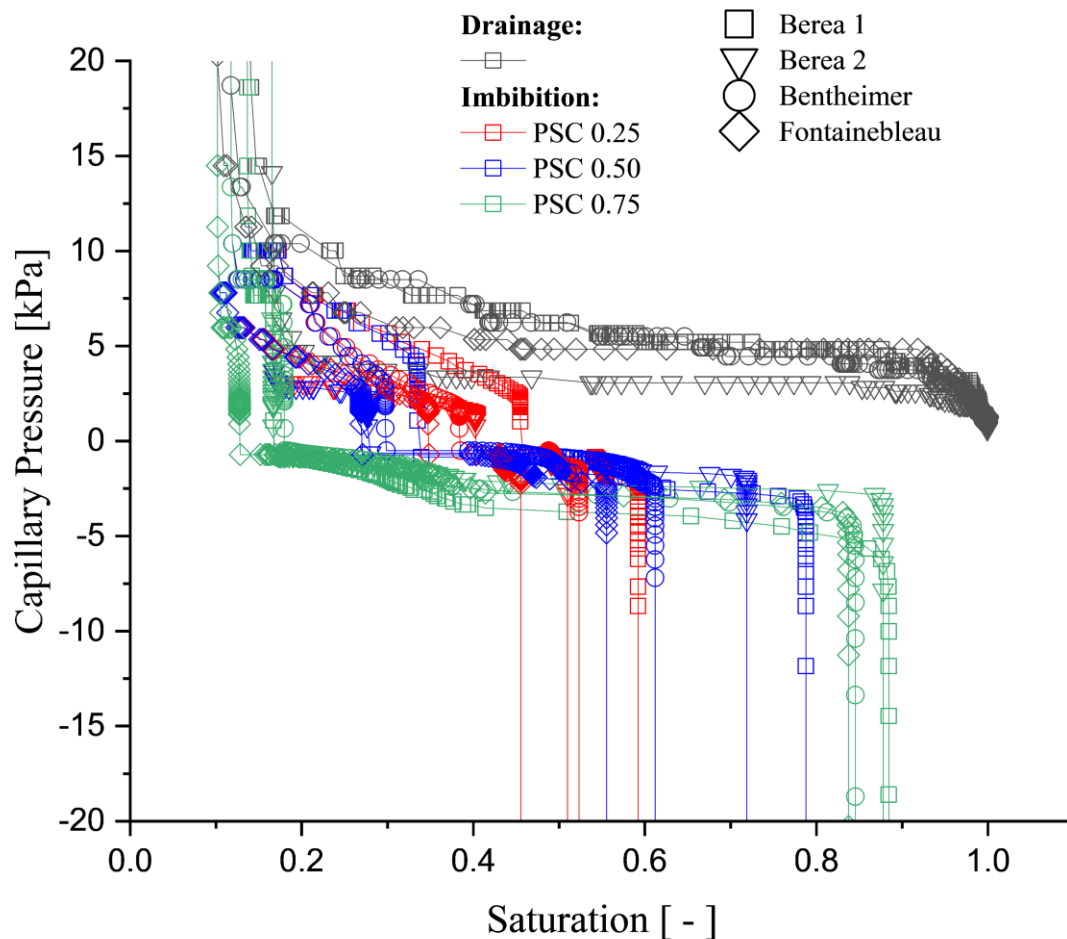
Figure 49 Capillary Pressure curves illustrating variations across distinct rock types, plotted for PSC values of 0.25 (in red), 0.50 (in blue), and 0.75 (in green), at a contact angle combination of 40°/140°. Various symbols represent the different rock types, while all drainage curves are marked in black.

Figure 49 presents the capillary pressure curves for various rock types, employing a deterministic approach with a contact angle setting of 40°/140° and varying PSC values.

Appendix B

Wetting Indices Multiple Contact Angles

The wetting (black) and Amott wetting (red) indices for four different wetting contact angles (0°, 10°, 40° and 60°) paired with one (140°) and four (120°, 140°, 170° and 180°) non-wetting contact angles.
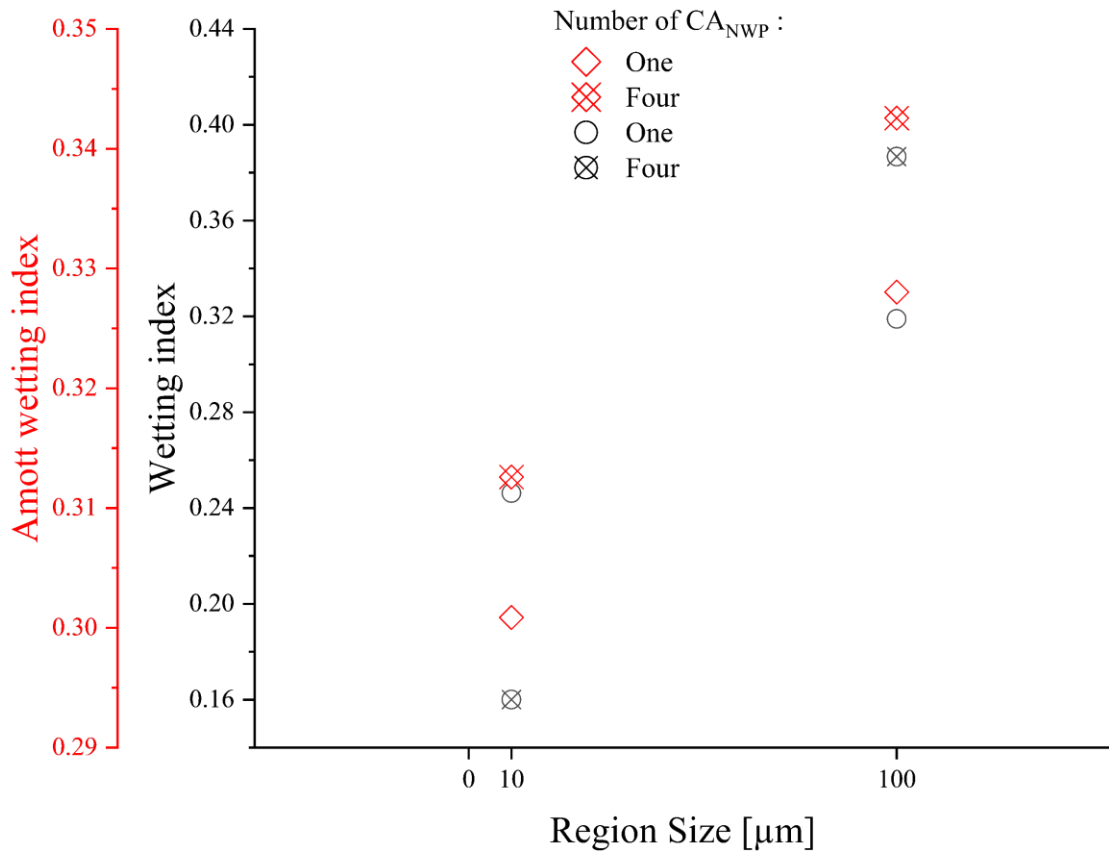
Figure 50 Wetting and Amott Wetting Indices for four wetting contact angles paired with a single non-wetting contact angle (One), and four wetting contact angles paired with four different non-wetting contact angles (Four), for two distinct region sizes (10μm and 100μm).

Appendix C

Relative Permeabilities for Multiple Contact Angles

Figure 51 and Figure 52 depict the relative permeability curves for four wetting contact angles paired with either one (140°) or four (120°, 140°, 170°, and 180°) non-wetting contact angles. The relative permeabilities are graphed against the saturation of the wetting phase using both linear (left) and logarithmic (right) scales. In these graphs, non-wetting regions were designated with PSC values of 0.25, 0.50, and 0.75, and region sizes of 10 µm and 100 µm for the wetting contact angles, all of which have the same area fraction of 1/4.
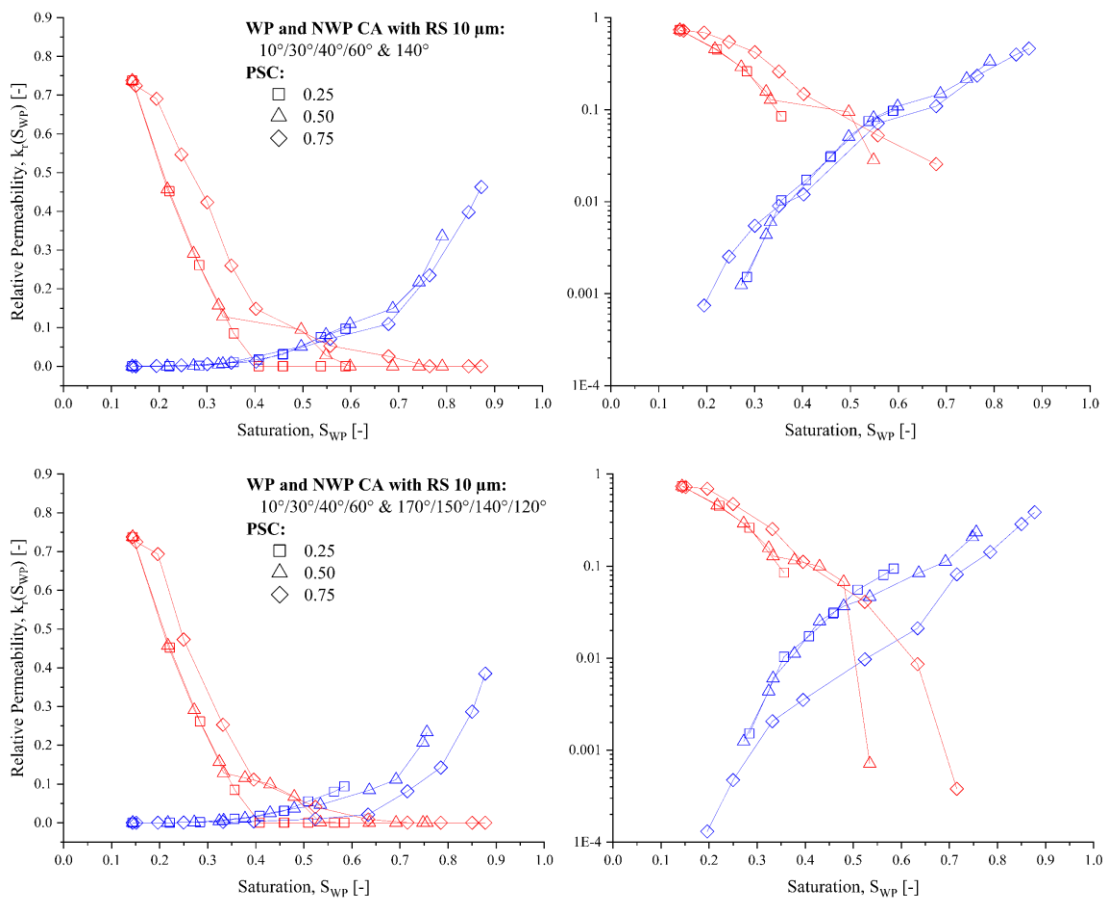
Figure 51 Relative permeabilities of the wetting (blue) and non-wetting (red) phase for four wetting contact angles paired with one (top) and four (bottom) non-wetting contact angles. The relative permeabilities are plotted against the saturation of the wetting phase on both linear (left) and logarithmic (right) scales. Non-wetting regions were assigned with PSC values of 0.25, 0.50, and 0.75, and a region size of 10 µm for the wetting contact angles, which all share an equal area fraction of 1/4.
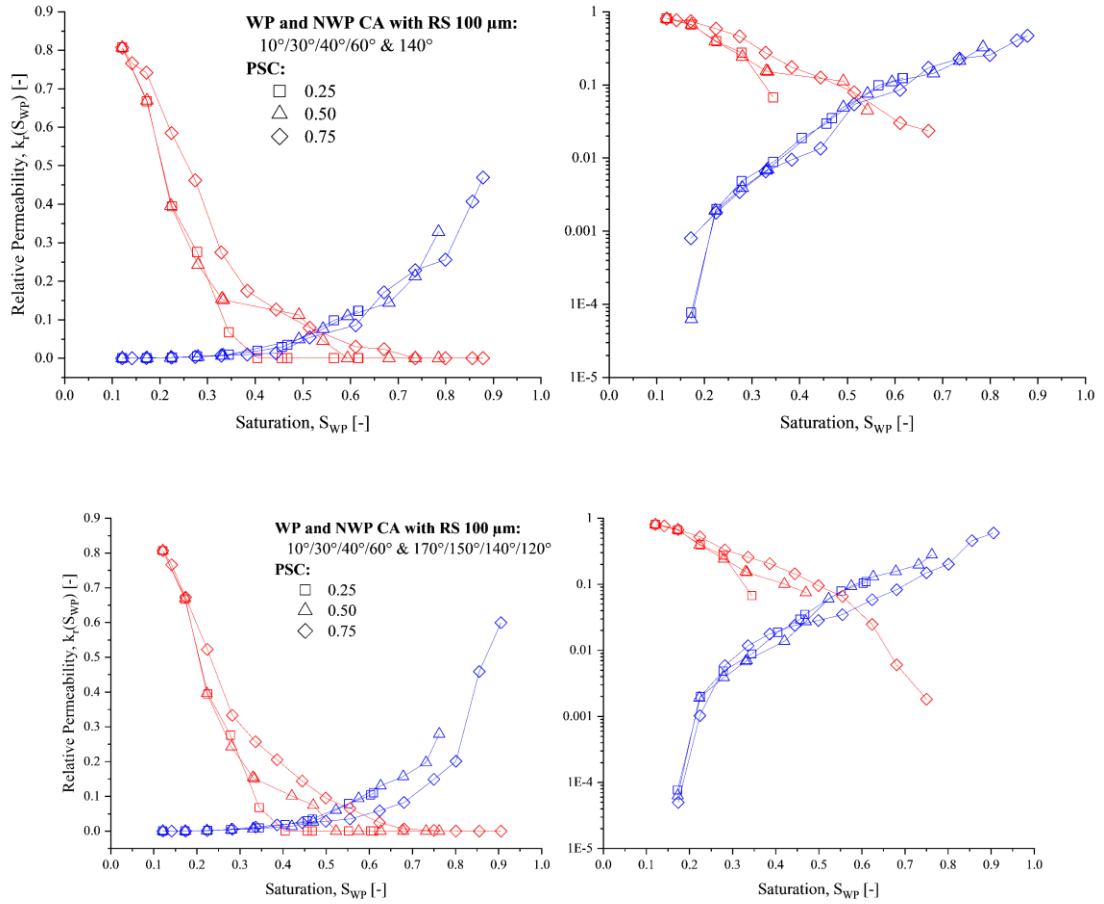
Figure 52 Relative permeabilities of the wetting (blue) and non-wetting (red) phase for four wetting contact angles paired with one (top) and four (bottom) non-wetting contact angles. The relative permeabilities are plotted against the saturation of the wetting phase on both linear (left) and logarithmic (right) scales. Non-wetting regions were assigned with PSC values of 0.25, 0.50, and 0.75, and a region size of 100 μm for the wetting contact angles, which all share an equal area fraction of 1/4.

Appendix D

Simulation Input in GeoDict

The flow chart shown in Figure 53 illustrates the necessary developments for successfully implementing forced imbibition when modelling multiphase displacement in GeoDict. During the course of this thesis several versions of GeoDict, including beta versions, were used for simulations, primarily utilizing GeoDict2021 and GeoDict2022. For the simulation of imbibition and the variation of settings, I developed custom scripts in addition to using the pre-existing ones. The software underwent continuous improvements throughout this project.

The functionalities discussed in this work are now largely accessible via the GeoApp (Two-Phase Flow) in the module titled "Hysteresis for Oil-Water Setups", as indicated by the red box in the flow chart (Figure 53). To replicate the simulations performed for this study, the "Wettability during imbibition" setting should be adjusted to mixed-wet. The "Aging method" tab provides an option to select between "Stochastic" and "Deterministic" modes, which correspond to the approaches employed in this thesis (see Figure 54).

To calculate the relative permeabilities, a distinct script was used. This script included a feature for cropping, as the structures had been mirrored prior to computing the primary drainage and imbibition. All individual scripts can be made available upon request.

Figure 53 Flowchart of the displacement modeling deployment and the developments added in the frame of this thesis. The red marked box indicates the features now available in the GeoApp "Hysteresis for Oil-Water"

Figure 54 Exemplary settings of the GeoApp "Hysteresis for Oil-Water" setups to replicate simulations performed within this thesis.

List of Figures

List of Tables

Nomenclature

A	Area	[m²]
k_r	Relative permeability	[-]
p_c	Capillary Pressure	[Pa]
S	Saturation	[-]
V	Volume	[m³]
θ	Contact angle	[°]
χ	Euler characteristic	[-]

Abbreviations

CA   Contact Angle

BH   Bentheimer

FB   Fontainebleau

FI   Forced Imbibition

LBM   Lattice Boltzmann Method

mCT   Micro computed tomography

MM   Morphological Method

NWP   Non-wetting Phase

PNM   Pore Network Modeling

PSC   Pore Space Considered

RS   Region Size

SCAL   Special Core Analysis

SI   Spontaneous Imbibition

SVP   Solid Volume Percentage

WI   Wetting index

WP   Wetting Phase